

THEORETICAL AND EXPERIMENTAL INVESTIGATION OF
WATER-GAS SHIFT REACTION OVER SUPPORTED COPPER/IRON
OXIDE CATALYSTS

ÖZGEN YALÇIN

SEPTEMBER 2017

THEORETICAL AND EXPERIMENTAL INVESTIGATION OF
WATER-GAS SHIFT REACTION OVER SUPPORTED COPPER/IRON
OXIDE CATALYSTS

A THESIS SUBMITTED TO
THE GRADUATE SCHOOL OF NATURAL AND APPLIED SCIENCES
OF
MIDDLE EAST TECHNICAL UNIVERSITY

BY

ÖZGEN YALÇIN

IN PARTIAL FULFILLMENT OF THE REQUIREMENTS
FOR
THE DEGREE OF DOCTOR OF PHILOSOPHY
IN
CHEMICAL ENGINEERING

SEPTEMBER 2017

Approval of the thesis:

**THEORETICAL AND EXPERIMENTAL INVESTIGATION OF
WATER-GAS SHIFT REACTION OVER SUPPORTED COPPER/IRON
OXIDE CATALYSTS**

submitted by **ÖZGEN YALÇIN** in partial fulfillment of the requirements for
the degree of **Doctor of Philosophy in Chemical Engineering Department,**
Middle East Technical University by,

Prof. Dr. Gülbin Dural Ünver

Dean, Graduate School of **Natural and Applied Sciences** _____

Prof. Dr. Halil Kalıpçılar

Head of Department, **Chemical Engineering** _____

Prof. Dr. Işık Önal

Supervisor, **Chemical Engineering Dept., METU** _____

Examining Committee Members:

Assoc. Prof. Dr. Görkem Külah

Chemical Engineering Dept., METU _____

Prof. Dr. Işık Önal

Chemical Engineering Dept., METU _____

Assoc. Prof. Dr. Emrah Özensoy

Chemistry Dept., Bilkent University _____

Assoc. Prof. Dr. Dilek Varışlı

Chemical Engineering Dept., Gazi University _____

Assist. Prof. Dr. Bahar İpek

Chemical Engineering Dept., METU _____

Date: September 6, 2017

I hereby declare that all information in this document has been obtained and presented in accordance with academic rules and ethical conduct. I also declare that, as required by these rules and conduct, I have fully cited and referenced all material and results that are not original to this work.

Name, Last name: Özgen YALÇIN

Signature :

ABSTRACT

THEORETICAL AND EXPERIMENTAL INVESTIGATION OF WATER-GAS SHIFT REACTION OVER SUPPORTED COPPER/IRON OXIDE CATALYSTS

Yalçın, Özgen

Ph.D., Department of Chemical Engineering

Supervisor: Prof. Dr. Işık Önal

September 2017, 157 pages

Density functional theory calculations were carried out to investigate the role of the chromium and copper, which were demonstrated to act as textural and catalytic promoters, respectively, for the $\text{Fe}_3\text{O}_4\text{-Cr}_2\text{O}_3\text{-CuO}$ catalyst system by *in situ* experimental studies at the atomic scale. There is a minor effect of Cr on the dissociative adsorption of H_2O , but no effect on CO adsorption on the $\text{Fe}_{\text{oct}2}$ termination of Fe_3O_4 (111) surface indicating that Cr does not act as a chemical promoter. Copper promotion of the $\text{Fe}_{\text{oct}2}$ terminated structure with a supported Cu_4 cluster facilitates CO adsorption at the new active sites present at the copper-iron oxide interface.

Zirconia-, niobia-, ceria-, and alumina-promoted supported copper/iron oxide catalysts were synthesized and investigated as the Cr-free iron oxide-based

catalysts. The characterization studies (*ex situ* XRD, *in situ* Raman spectroscopy, High-Sensitivity Low Energy Ion Scattering (LEIS), CO-TPR and flow BET surface area) revealed the interplay between the different components of this dynamic catalyst system. The promoted catalysts were found to have significantly greater thermostability than the unpromoted iron oxide catalyst. The promoted catalysts without copper did not perform better than the unpromoted iron oxide catalyst for the WGS reaction. Al promoter provides better thermostability and higher activity. Desired Cr-free catalyst is the combination of BET stability of Al promoter with redox activity of Ce promoter.

This research study combines theoretical and experimental investigations under the partnership between the Department of Chemical Engineering of Middle East Technical University and Department of Chemical & Biomolecular Engineering of Lehigh University (USA).

Keywords: Water-gas shift reaction, copper/iron oxide, Cr-free, DFT, *in situ* characterization

ÖZ

SU-GAZ DEĞİŞİM TEPKİMESİNİN DESTEKLİ BAKIR/DEMİR OKSİT KATALİZÖRLERİ ÜZERİNDE TEORİK VE DENEYSEL İNCELENMESİ

Yalçın, Özgen

Doktora, Kimya Mühendisliği Bölümü

Tez Yöneticisi: Prof. Dr. Işık Önal

Eylül 2017, 157 sayfa

Fe_3O_4 - Cr_2O_3 - CuO katalizör sistemi için yerinde deneysel çalışmalarla, sırasıyla, dokusal ve katalitik destekçi oldukları kanıtlanan krom ve bakırın rollerini atomik ölçekte araştırmak için yoğun fonksiyon teori (DFT) hesaplamaları uygulanmıştır. Kromun, suyun Fe_3O_4 (111) yüzeyi Fe_{oct2} bitişinde ayrışmalı yüzeye tutunması üzerinde az bir etkisi varken karbon monoksitin aynı yüzey üzerinde yüzeye tutunmasında etkisinin olmaması kromun katalitik destekçi olarak davranmadığının göstergesidir. Cu_4 küme destekli Fe_{oct2} bitişindeki bakır destekçi, bakır-demir oksit ara bağındaki yeni aktif konumlarda karbon monoksit yüzey tutunmasını kolaylaştırmaktadır.

Kromsuz demir oksit bazlı katalizörler olarak zirkonya-, nioby-, serya- ve alumina-iyileştirilmiş destekli bakır/demir oksit katalizörleri sentezlenmiş ve

incelenmiştir. Nitelendirme çalışmaları (yeri dışında XRD, yerinde Raman spektroskopisi, Yüksek-Hassasiyetli Düşük Enerji İyon Saçılması (HT-LEIS), CO-TPR ve BET yüzey alanı) bu dinamik katalizör sisteminin farklı bileşenleri arasındaki etkileşimleri ortaya çıkarmıştır. İyileştirilmiş katalizörlerin ısıl dayanıklılığının iyileştirilmemiş demir oksit katalizöründen önemli ölçüde büyük olduğu bulunmuştur. Bakırsız iyileştirilmiş katalizörler su-gaz değişim tepkimesi için iyileştirilmemiş demir oksit katalizöründen daha iyi performans göstermemiştir. Al destekçisi daha iyi ısıl dayanıklılık ve daha yüksek aktiflik sağlamıştır. Al destekçisinin BET yüzey alanı kararlılığının ve Ce destekçisinin redoks aktivitesinin birleştirilmesi potansiyel tasarlanmış kromsuz katalizördür.

Bu çalışma, Lehigh Üniversitesi'nin (ABD) Kimya ve Biyomoleküler Mühendisliği Bölümü ile Orta Doğu Teknik Üniversitesi'nin Kimya Mühendisliği Bölümü arasındaki ortaklık bünyesindeki teorik ve deneysel araştırmaları birleştirmektedir.

Anahtar sözcükler: Su-gaz değişim tepkimesi, bakır/demir oksit, kromsuz, DFT, yerinde nitelendirme

To my beloved family

ACKNOWLEDGEMENTS

I would like to express my sincere gratitude to my supervisors, Prof. Dr. Işık Önal and Prof. Dr. Israel E. Wachs, Lehigh University, for their guidance and for providing a rare opportunity to be part of the dual degree Ph.D. program. Being a member of their research group has enabled me to grow significantly as a researcher. I would also like to thank my defense committee members and especially the progress committee members: Assoc. Prof. Dr. Emrah Özensoy and Assoc. Prof. Dr. Görkem Külâh.

I am indebted to people with whom I shared the laboratories at Lehigh University and METU: Dr. Michael Ford, Prof. Dr. Jihmirn Jehng, Benjamin Moskowitz, Anisha Chakrabarti, and in particular, Dr. Minghui Zhu and İlker Tezsevin. I have learnt much about the experimental details from Dr. Minghui Zhu and the computational details from İlker Tezsevin. I would like to thank Dr. Henry Luftman for long discussions about the results and Dr. Kemal Tuzla for his endless support and advices.

I am grateful to Dr. Arzu Kanca for her endless friendship, suggestions, advices and sharing tough days of my life.

I want to give my cordial thanks to my friends who do not leave me alone on this rough path and help me enjoy the life. I cannot imagine how tough the life would be without the friendship of Dr. Fulya Akpınar Singh in the U.S.

I would like to give my warmest thanks to Dr. Manos Roumpelakis who is always positive, supportive, and thoughtful. He made me question the priorities of my life and welcome life as it is without overthinking the past or future.

Last but not the least, I would like to express my deepest thanks and respect to my parents: Fahriye and Mustafa Yalçın. Without their belief in me and moral and emotional support, I could not have come to the end of this thesis.

I am also grateful to my brother Özkan, my sister Özgün and her husband Deniz İyidinç, and my lovable nieces: Derin and Deren İyidinç for everlasting love.

The calculations reported in this study were performed at TUBITAK (Scientific and Research Council of Turkey) ULAKBIM, High Performance and Grid Computing Center (TR-Grid e-Infrastructure). Moreover, TUBITAK is kindly acknowledged for financial support by National Scholarship Programme for PhD Students and 2214/B International Joint PhD Fellowship Programme. I acknowledge financial support from National Science Foundation Grant CBET – 1511689.

TABLE OF CONTENTS

ABSTRACT	v
ÖZ.....	vii
ACKNOWLEDGEMENTS	x
TABLE OF CONTENTS	xii
LIST OF TABLES	xvii
LIST OF FIGURES	xix
CHAPTERS	
1. INTRODUCTION	1
1.1 Background	1
1.2 Previous Studies	6
1.2.1 Powdered CuO-Cr ₂ O ₃ -Fe ₂ O ₃ Catalysts	6
1.2.2 Powdered Cr-Free Iron Oxide Catalysts.....	11
1.2.3 Well-Defined Model Catalysts	17
1.2.4 Theoretical Studies of Iron Oxide Catalysts.....	18
1.3 Motivation and Research Objectives	23
1.4 Thesis Outline	25
2. EXPERIMENTAL METHOD	27
2.1 Characterization Developments: <i>Operando</i> and <i>in situ</i> approach	27
2.2 Experimental Procedure	30
2.2.1 Catalyst Preparation.....	30
2.2.2 Catalyst Characterization.....	31
2.2.2.1 X-Ray Diffraction (XRD).....	32
2.2.2.2 <i>In situ</i> Raman Spectroscopy	32
2.2.2.3 High Sensitivity Low Energy Ion Scattering (HS-LEIS)	33
2.2.2.4 Flow BET Surface Area.....	34
2.2.3 CO-TPR	34
2.2.4 Steady-State Activity Measurement	34
3. COMPUTATIONAL METHOD.....	37
3.1 Computational Chemistry	37

3.1.1	Density Functional Theory	37
3.1.2	Approximations	42
3.1.2.1	Local Density Approximation (LDA) & Local Spin- Density Approximation	42
3.1.2.2	The Generalized Gradient Approximation	43
3.1.2.3	LDA/GGA+U	44
3.1.3	The VASP Software	45
3.2.	Computational Procedure.....	46
3.2.1	Clean Magnetite Bulk Calculations.....	46
3.2.2	Computational Details	47
3.2.2.1	Energy Analysis.....	48
4.	Cr ₂ O ₃ -Fe ₂ O ₃ CATALYSTS OXYGEN TERMINATED Fe ₃ O ₄ (111) SURFACE	51
4.1	Abstract	51
4.2	Results and Discussion	51
4.2.1	Bulk Optimization	51
4.2.2	Surface Optimization	53
4.2.3	O _{oct1} Termination of Fe ₃ O ₄ (111)	54
4.2.3.1	Chromium Atomic Substitution on O _{oct1} Termination of Fe ₃ O ₄ (111).....	54
4.2.3.2	Regenerative Mechanism on the Surfaces.....	58
4.2.3.2.1	Regenerative Mechanism on O _{oct1} Terminated Surface	58
4.2.3.2.2	Regenerative Mechanism on O _{oct2} Cr Termination	60
4.2.3.2.3	Bader Charge Analysis of Regenerative Mechanism on O _{oct1} and O _{oct2} Cr	64
4.2.3.2.4	Vibrational Frequency Calculations	68
4.3	Conclusions	70
5.	CuO-Cr ₂ O ₃ -Fe ₂ O ₃ CATALYSTS IRON TERMINATED Fe ₃ O ₄ (111) SURFACE	73
5.1	Abstract	73
5.2	Results and Discussion	73
5.2.1	Bulk Optimization	73
5.2.2	Surface Optimization	74

5.2.3 Chromium Substitution on the Fe _{oct2} Surface	76
5.2.4 Reduction of the Fe ₃ O ₄ (111) Surface	79
5.2.5 Single H ₂ O and CO Adsorption on Fe _{oct2} and Feoct2_Cr_ooa Surfaces	84
5.2.5.1 H ₂ O Adsorption on Fe _{oct2} and Feoct2_Cr_ooa Surfaces	84
5.2.5.2 CO Adsorption on Fe _{oct2} and Feoct2_Cr_ooa Surfaces	85
5.2.6 H ₂ O Adsorption on Fe _{oct2} Termination	86
5.2.6.1 CO Adsorption on Fe _{oct2} Termination with Hydroxyl Groups	87
5.2.7 Redox Reaction on Fe _{oct2} Termination	88
5.2.8 Cu ₄ Cluster on Fe _{oct2} Termination	92
5.2.8.1 CO Adsorption on Fe _{oct2} Termination with Cu ₄ Cluster	93
5.3 Conclusions	95
6. HIGH TEMPERATURE WATER-GAS SHIFT REACTION OVER Cr- FREE IRON OXIDE-BASED CATALYSTS	97
6.1 Abstract	97
6.2 Results	98
6.2.1 Fe ₂ O ₃	98
6.2.2 Zr-promoted Iron Oxide Catalysts	100
6.2.2.1 XRD	101
6.2.2.2 <i>In situ</i> Raman Spectroscopy	102
6.2.2.3 High Sensitivity Low-Energy Ion Scattering (HS- LEIS) Spectroscopy	103
6.2.2.4 Flow BET Surface Area	105
6.2.2.5 CO-TPR	106
6.2.2.6 Catalytic Activity during Steady-State HT-WGS Reaction	107
6.2.2.7 Schematic Model	108
6.2.3 Nb-promoted Iron Oxide Catalysts	109
6.2.3.1 XRD	109
6.2.3.2 <i>In situ</i> Raman Spectroscopy	110
6.2.3.3 High Sensitivity Low-Energy Ion Scattering (HS- LEIS) Spectroscopy	111

6.2.3.4	Flow BET Surface Area	113
6.2.3.5	CO-TPR.....	114
6.2.3.6	Catalytic Activity during Steady-State HT-WGS Reaction	114
6.2.3.7	Schematic Model.....	115
6.2.4	Ce-promoted Iron Oxide Catalysts	116
6.2.4.1	XRD.....	116
6.2.4.2	<i>In situ</i> Raman Spectroscopy	117
6.2.4.3	High Sensitivity Low-Energy Ion Scattering (HS- LEIS) Spectroscopy	118
6.2.4.4	Flow BET Surface Area	120
6.2.4.5	CO-TPR.....	121
6.2.4.6	Catalytic Activity during Steady-State HT-WGS Reaction	122
6.2.4.7	Schematic Model.....	122
6.2.5	Al-promoted Iron Oxide Catalysts	123
6.2.5.1	XRD.....	123
6.2.5.2	<i>In situ</i> Raman Spectroscopy	124
6.2.5.3	High Sensitivity Low-Energy Ion Scattering (HS- LEIS) Spectroscopy	125
6.2.5.4	Flow BET Surface Area	126
6.2.5.5	CO-TPR.....	127
6.2.5.6	Catalytic Activity during Steady-State HT-WGS Reaction	128
6.2.5.7	Schematic Model.....	129
6.3	Discussion	129
6.3.1	Bulk Structure.....	129
6.3.2	Surface Structure	131
6.3.3	Catalyst Thermostability.....	132
6.3.4	Catalytic Activity-Structure Relationship	132
6.4	Conclusions	133
7.	CONCLUSIONS and RECOMMENDATIONS.....	135
7.1	Conclusions	135
7.2	Recommendations	136

REFERENCES	139
APPENDICES	
A. SUPPORTING INFO FOR SECTION 6.2.1	153
CURRICULUM VITAE	155

LIST OF TABLES

Table 2.1. Abbreviations of the catalyst	32
Table 3.1. Observed and calculated bond distances and u parameter	47
Table 4.1 Optimized bulk lattice parameter for different methods	52
Table 4.2. Energy change values due to Cr atom substitution on O_{oct1} surface	55
Table 4.3 Regenerative mechanism steps of water gas shift reaction on O_{oct1} surface	59
Table 4.4. Regenerative mechanism steps of water gas shift reaction on $O_{oct2}Cr$ surface.....	61
Table 4.5. Bader charge of selected atoms for CO adsorption on the surfaces	66
Table 4.6 Bader charge of selected atoms for H_2O adsorption on the surfaces	68
Table 4.7 Calculated and experimental vibrational frequency values of CO and CO_2 in unit of cm^{-1}	68
Table 4.8. Vibrational frequency values (cm^{-1}) of CO adsorption on O_{oct1} and $O_{oct2}Cr$	69
Table 5.1. Energy change and magnetic moment of Cr doped Fe_{oct2} surface	77
Table 5.2. Oxygen vacancy formation energies on Fe_{oct2} and Fe_{tet1} surfaces	80
Table 5.3. Oxygen vacancy formation energies on Fe_{oct2} and $Fe_{oct2}Cr_{ooa}$ surfaces	83
Table 5.4. Bader charges of selected atoms on Fe_{oct2} and $Fe_{oct2}Cr_{ooa}$ surfaces before and after oxygen vacancy	84
Table 5.5. Bader charges of selected atoms on Fe_{oct2} surfaces through CO_2 formation	91

Table 6.1. (a) BET surface area (dehydration: 10% O ₂ /Ar at 400 °C for 1 hr, WGS reaction: 10% CO/Ar (10 mL/min), He (30 mL/min), and water vapor (H ₂ O/CO ~ 1)) and (b) steady-state catalytic activity via CO conversion (10% CO/Ar (10 mL/min), He (30 mL/min), and water vapor (H ₂ O/CO ~ 1)) of unpromoted iron oxide catalyst	100
Table 6.2. BET surface areas of Fe, 8ZrFe and supported 3Cu/8ZrFe catalysts after dehydration: 10% O ₂ /Ar at 400 °C for 1 hr and WGS reaction: 10% CO/Ar (10 mL/min), He (30 mL/min), and water vapor (H ₂ O/CO ~ 1)	105
Table 6.3. Steady-state HT-WGS (10% CO/Ar (10 mL/min), He (30 mL/min), and water vapor (H ₂ O/CO ~ 1)) catalytic activities after 1 hr of reaction for Fe, 8ZrFe and supported 3Cu/8ZrFe catalysts based on CO conversion (x10 ⁻⁶ mol/s.g)	108
Table 6.4. BET surface areas of Fe, 8NbFe and supported 3Cu/8NbFe catalysts (m ² /g) after dehydration: 10% O ₂ /Ar at 400 °C for 1 hr and WGS reaction: 10% CO/Ar (10mL/min), He (30 mL/min), and water vapor (H ₂ O/CO ~ 1)	113
Table 6.5. Steady-state HT-WGS (10% CO/Ar (10 mL/min), He (30 mL/min), and water vapor (H ₂ O/CO ~ 1)) catalytic activities after 1 hr of reaction for Fe, 8NbFe and 3Cu/8NbFe catalysts based on CO conversion (x10 ⁻⁶ mol/s.g) ...	115
Table 6.6. BET surface areas of Fe, 8CeFe and supported 3Cu/8CeFe catalysts (m ² /g) after dehydration: 10% O ₂ /Ar at 400 °C for 1 hr and WGS reaction: 10% CO/Ar (10 mL/min), He (30 mL/min), and water vapor (H ₂ O/CO ~ 1)	121
Table 6.7. Steady-state HT-WGS (10% CO/Ar (10 mL/min), He (30 mL/min), and water vapor (H ₂ O/CO ~ 1)) catalytic activities after 1 hr of reaction for Fe, 8CeFe and supported 3Cu/8CeFe catalysts based on CO conversion (x10 ⁻⁶ mol/s.g)	122
Table 6.8. BET surface areas of Fe and supported 3Cu8AlFe catalysts (m ² /g) after dehydration: 10% O ₂ /Ar at 400 °C for 1 hr and WGS reaction: 10% CO/Ar (10 mL/min), He (30 mL/min), and water vapor (H ₂ O/CO ~ 1)	127
Table 6.9. Steady-state HT-WGS (10% CO/Ar (10 mL/min), He (30 mL/min), and water vapor (H ₂ O/CO ~ 1)) catalytic activities after 1 hr of reaction for Fe and supported 3Cu8AlFe catalysts based on CO conversion (x10 ⁻⁶ mol/s.g). 128	

LIST OF FIGURES

Figure 1.1. Typical variations of carbon monoxide levels in high temperature and low temperature shift catalyst beds	3
Figure 2.1. Geometry of an ion-scattering experiment. An incident ion with mass M_{ion} and energy E_i collides with a sample atom of mass M and loses energy. Its final kinetic energy E_f , after scattering over an angle θ is a measure for the mass of the target atom	30
Figure 4.1. Bulk structure of Fe_3O_4 with LDA+U (Fe: purple, O: red)	53
Figure 4.2. Six terminations of Fe_3O_4 (111) surface (Fe: purple, O: red)	55
Figure 4.3. Possible chromium substitution with iron atoms on O_{oct1} termination of Fe_3O_4 (111) surface (Fe: purple, O: red, Cr: gray)	57
Figure 4.4. (a) Initial (b) Optimized structures of possible location of 2 chromium atoms on O_{oct1} termination of Fe_3O_4 (111) surface (Fe: purple, O: red, Cr: gray)	57
Figure 4.5. Energy profiles & optimized configurations of reaction steps on O_{oct1} surface (Fe: purple, O: red, C: yellow, H: blue)	60
Figure 4.6. Energy profiles & optimized configurations of reaction steps on O_{oct2Cr} surface (Fe: purple, O: red, Cr: gray, C: yellow, H: blue)	62
Figure 4.7. Direct hydrogen-hydrogen interaction for O_{oct2Cr} termination (a) initial geometry (b) final geometry (Fe: purple, O: red, Cr: gray, C: yellow, H: blue)	62
Figure 4.8. Hydrogen atom desorption for O_{oct2Cr} termination (a) desorption of first hydrogen atom (b) desorption of second hydrogen atom (c) final geometry (Fe: purple, O: red, Cr: gray, C: yellow, H: blue)	63
Figure 4.9. Selected atoms of CO adsorption on O_{oct1} surface (Fe: purple, O: red, C: yellow)	65
Figure 4.10. Selected atoms of CO adsorption on O_{oct2Cr} surface (Fe: purple, O: red, C: yellow, Cr: gray)	65
Figure 4.11. Selected atoms of H_2O adsorption on O_{oct1} surface (Fe: purple, O: red, H: blue)	67

Figure 4.12. Selected atoms of H ₂ O adsorption on Ooct2Cr surface (Fe: purple, O: red, H: light blue, Cr: gray)	67
Figure 5.1. Bulk structure of Fe ₃ O ₄ with spin polarized GGA+U (Fe _{tet} : light blue, Fe _{oct} : blue, O: red)	74
Figure 5.2. Optimized structures of (a) Fe _{tet1} and (b) Fe _{oct2} terminations (Fe _{tet} : light blue, Fe _{oct} : blue, O: red)	76
Figure 5.3. Initial structures of differently located Cr atoms in Fe _{oct2} structure (Fe _{tet} : light blue, Fe _{oct} : blue, O: red, Cr: gray)	78
Figure 5.4. Optimized structure of Feoct2_Cr_ooa surface (Fe _{tet} : light blue, Fe _{oct} : blue, O: red, Cr: gray)	79
Figure 5.5. Possible oxygen sites on (a) Fe _{tet1} surface and (b) Fe _{oct2} surface (Fe _{tet} : light blue, Fe _{oct} : blue, O: red)	81
Figure 5.6. Top view of the schematic representation of the (111) surface after relaxation: (raw a) Fe _{oct2} and (raw b) Feoct2_Cr_ooa surface (Fe _{tet} : light blue, Fe _{oct} : blue, O: red, Cr: gray)	82
Figure 5.7. Selected atoms on Feoct2_Cr_ooa for Bader charge comparison (Fe _{tet} : light blue, Fe _{oct} : blue, O: red, Cr: gray)	83
Figure 5.8. H ₂ O adsorption on the (a) Fe _{oct2} terminated and the (b) Feoct2_Cr_ooa terminated Fe ₃ O ₄ (111) surface. The bond length unit is angstrom. (Fe _{tet} : light blue, Fe _{oct} : blue, O: red, Cr: gray, H: white)	85
Figure 5.9. CO adsorption on the (a) Fe _{oct2} terminated and the (b) Feoct2_Cr_ooa terminated Fe ₃ O ₄ (111) surface. The bond length unit is angstrom. (Fe _{tet} : light blue, Fe _{oct} : blue, O: red, Cr: gray, C: yellow)	86
Figure 5.10. Structure optimized for (a) one and (b) two H ₂ O molecules adsorbed at the Fe _{oct2} terminated Fe ₃ O ₄ (111) surface. The bond length unit is angstrom. (Fe _{tet} : light blue, Fe _{oct} : blue, O: red, H: white)	87
Figure 5.11. Optimized structure of CO adsorbed on the Fe _{oct2} terminated Fe ₃ O ₄ (111) surface (a) without a hydroxyl group, (b) with two hydroxyl groups, (c) with four hydroxyl groups (d) top of Fe _{tet} site, and (e) some Fe _{oct} site with OH group. The bond length unit is angstrom. (Fe _{tet} : light blue, Fe _{oct} : blue, O: red, H: white, C: yellow)	88
Figure 5.12. Optimized structures of CO ₂ formation on the Fe _{oct2} terminated Fe ₃ O ₄ (111) surface (a) CO adsorption on Fe _{oct} site (b) CO interaction with O _{lat} (c) CO ₂ in the gas phase (Fe _{tet} : light blue, Fe _{oct} : blue, O: red, C: yellow)	90

Figure 5.13. Possible pathways for H ₂ formation on the Fe _{oct2} terminated Fe ₃ O ₄ (111) surface (Fe _{tet} : light blue, Fe _{oct} : blue, O: red, H: white)	92
Figure 5.14. (a) Cu ₄ cluster in the gas phase and (b) adsorbed Cu ₄ cluster on the Fe _{oct2} terminated Fe ₃ O ₄ (111) surface (Fe _{tet} : light blue, Fe _{oct} : blue, O: red, Cu: brown)	93
Figure 5.15. Optimized structure of CO adsorbed on the Fe _{oct2} terminated Fe ₃ O ₄ (111) surface with Cu ₄ cluster at (a) Fe _{oct} site, (b) the bridge between Fe _{oct} -Cu, (c) Cu site bonded to Fe _{tet} , and (d) Cu site (Fe _{tet} : light blue, Fe _{oct} : blue, O: red, C: yellow, Cu: brown)	95
Figure 6.1. XRD diffractogram of unpromoted (α -Fe ₂ O ₃) catalyst calcined at 400 °C and taken under ambient conditions as a function of 2 Θ (a) full scan and (b) Fe ₂ O ₃ (110) peak	98
Figure 6.2. <i>In situ</i> Raman (442nm) spectra of calcined Fe ₂ O ₃ catalyst at 400 °C: (a) dehydrated in 10% O ₂ /Ar, (b) RWGS reaction conditions (30 mL/min 5%CO ₂ /Ar and 15 mL/min 10%H ₂ /Ar).....	99
Figure 6.3. XRD diffractograms of Fe ₂ O ₃ , 8ZrFe and supported 3Cu/8ZrFe catalysts calcined at 400 °C and taken under ambient conditions as a function of 2 Θ (a) full scan and (b) Fe ₂ O ₃ (110) peak	101
Figure 6.4. The <i>in situ</i> Raman spectra of (a) 8ZrFe and (b) supported 3Cu/8ZrFe catalysts under dehydration in 10% O ₂ /Ar and RWGS reaction conditions (30 mL/min 5%CO ₂ /Ar and 15 mL/min 10%H ₂ /Ar) at 400 °C	103
Figure 6.5. The BET surface area normalized HS-LEIS Fe, Zr, and Cu atomic density of both (a) dehydrated, calcined and (b) activated supported 3Cu/8ZrFe catalyst with the 5keV Ne ⁺ dose as a function of sputtering depth. The vertical dashed lines indicate doses of n(1x10 ¹⁵ ions/cm ²), with n=1,2,3, etc., that correspond to removal of a monolayer-equivalents from the catalyst	105
Figure 6.6. CO-TPR spectra of activated Fe, 8CrFe, 3Cu/8CrFe, and 3Cu/8ZrFe catalysts activated by WGS reaction conditions at 350 °C.....	107
Figure 6.7. Schematic of the supported 3Cu/8ZrFe catalyst (a) calcined and (b) during HT-WGS	108
Figure 6.8. XRD diffractogram of calcined Fe ₂ O ₃ , 8NbFe and supported 3Cu/8NbFe catalysts calcined at 400 °C and taken under ambient conditions as a function of 2 Θ (a) full scan and (b) Fe ₂ O ₃ (110) peak	110
Figure 6.9. The <i>in situ</i> Raman spectra of (a) 8NbFe and (b) 3Cu/8NbFe catalysts under dehydration in 10% O ₂ /Ar and RWGS reaction conditions (30 mL/min	

5%CO₂/Ar and 15 mL/min 10%H₂/Ar) at 400 °C. RWGS_1 and RWGS_2 signify spectral collection from different points..... 111

Figure 6.10. The BET surface area normalized HS-LEIS Fe, Nb, and Cu Atomic density of both (a) dehydrated, calcined and (b) activated supported 3Cu/8NbFe catalyst with the 5keV Ne⁺ dose as a function of sputtering depth. The vertical dashed lines indicate doses of $n(1 \times 10^{15} \text{ ions/cm}^2)$, with $n=1,2,3$, etc., that correspond to removal of a monolayer-equivalents from the catalyst 112

Figure 6.11. CO-TPR spectra of activated Fe, 8CrFe, 3Cu/8CrFe, and 3Cu/8NbFe catalysts activated by WGS reaction conditions at 350 °C..... 114

Figure 6.12. Schematic of the supported 3Cu/8NbFe catalyst (a) calcined and (b) during HT-WGS 116

Figure 6.13. XRD diffractograms of Fe₂O₃, 8CeFe and supported 3Cu/8CeFe catalysts calcined at 400 °C and taken under ambient conditions as a function of 2 Θ (a) full scan and (b) Fe₂O₃ (110) peak 117

Figure 6.14. The *in situ* Raman spectra of (a) 8CeFe and (b) 3Cu/8CeFe catalysts under dehydration in 10% O₂/Ar and RWGS reaction conditions (30 mL/min 5%CO₂/Ar and 15 mL/min 10%H₂/Ar) at 400 °C. RWGS_1 and RWGS_2 signify spectral collection from different points 118

Figure 6.15. The BET surface area normalized HS-LEIS Fe, Ce, and Cu Atomic density of both (a) dehydrated, calcined and (b) activated supported 3Cu/8CeFe catalyst with the 5keV Ne⁺ dose. The vertical dashed lines indicate doses of $n(1 \times 10^{15} \text{ ions/cm}^2)$, with $n=1,2,3$, etc., that correspond to removal of a monolayer-equivalents from the catalyst..... 120

Figure 6.16. CO-TPR spectra of activated Fe, 8CrFe, 3Cu/8CrFe, and 3Cu/8CeFe catalysts activated by WGS reaction conditions at 350 °C 121

Figure 6.17. Schematic of the 3Cu/8CeFe catalyst (a) calcined and (b) during HT-WGSR 123

Figure 6.18. XRD diffractograms of Fe₂O₃ and supported 3Cu8AlFe catalysts calcined at 400 °C and taken under ambient conditions as a function of 2 Θ (a) full scan and (b) Fe₂O₃ (110) peak 124

Figure 6.19. The *in situ* Raman spectra of 3Cu8AlFe catalysts under dehydration in 10% O₂/Ar and RWGS reaction conditions (30 mL/min 5%CO₂/Ar and 15 mL/min 10%H₂/Ar) at 400 °C 125

Figure 6.20. The BET surface area normalized HS-LEIS Fe, Al, and Cu Atomic density of both (a) dehydrated, calcined and (b) activated supported 3Cu8AlFe catalyst with the 3keV He⁺ and 5keV Ne⁺ dose. The vertical dashed lines indicate doses of $n(1 \times 10^{15} \text{ ions/cm}^2)$, with $n=1,2,3$, etc., that correspond to removal of a monolayer-equivalents from the catalyst126

Figure 6.21. CO-TPR spectra of activated Fe, 8CrFe, 3Cu/8CrFe, and 3Cu8AlFe catalysts activated by WGS reaction conditions at 350 °C128

Figure 6.22. Schematic of the 3Cu8AlFe catalyst (a) calcined and (b) during HT-WGSR.....129

Figure A.1. *In situ* Raman (442nm) spectra of calcined unpromoted iron oxide catalyst at 400 °C: (a) reoxidized in 10% O₂/Ar and (b) RWGS reaction conditions (2nd time, (30 mL/min 5%CO₂/Ar and 15 mL/min 10%H₂/Ar))153

CHAPTER 1

INTRODUCTION

1.1. Background

Industrial hydrogen production from various resources is driven by the world's advancement towards a Hydrogen economy. The water-gas shift (WGS) reaction is the intermediate step for carbon-based hydrogen production and is used for hydrogen enrichment and carbon monoxide reduction of the synthesis gas (H_2/CO)¹⁻³. For fuel cells, it is critical to reduce the CO concentration to ppm levels since CO is a poison that deactivates the catalysts⁴.

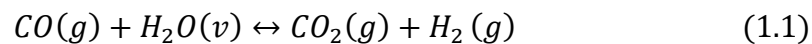
The industrial applications of hydrogen from the WGS reaction are hydrogenation reactions (ammonia, methanol, hydrocarbon refinery fuels, specialty chemicals, pharmaceuticals, food, etc.), synthetic fuels (Fischer-Tropsch process), metals (by reduction of metal oxide ores) and feedstock for fuel cells. The water-gas feed is manufactured by steam reforming, partial oxidation and dry reforming (CO_2 reforming) of carbonaceous materials (coal, coke, natural gas, naphtha, etc.). The highest molar ratio of H_2/CO of 3 is obtainable from CH_4 steam reforming makes methane the most popular feedstock. The lowest H_2/CO molar ratio is produced by dry reforming because CO_2 is hydrogen free⁵.

The WGS reaction was first observed by Felice Fontana in 1780 when steam was passed through a bed of incandescent coke and produced a combustible gas (water-gas). Ludwig Mond and his assistant Carl Langer were the first chemists to study a working fuel cell using coal-derived Mond gas (the product of the reaction of air and steam passed through coal/coke- CO_2 , CO, H_2 , N_2 , etc.). The pure hydrogen feed was produced by passing the Mond gas mixture and steam over finely divided nickel at 400 °C, reacting the carbon monoxide and steam to give carbon dioxide and more hydrogen, and removing

CO₂ by an alkaline wash⁶. Only in 1888 was the modern WGS reaction discovered and reported in the literature (as indicated in reaction 1.1 below)^{6,7}. In 1913, the WGS reaction found industrial application in the Haber-Bosch process of ammonia manufacture by preventing deactivation of Fe-based catalyst by carbon oxides present in synthesis gas. For the past century, the WGS reaction has been utilized to produce hydrogen for ammonia synthesis, methanol synthesis and controlling the optimum molar ratio of H₂/CO ratio for the Fischer-Tropsch process⁶⁻⁹. Currently, there is much environmental interest in employing hydrogen for fuel cells because of the higher efficiency of fuel cells than internal combustion engines and the production of only steam as the exhaust product^{6,10}.

In 1914, Bosch and Wild discovered that an iron-chromium mixed oxide catalyst could convert a mixture of steam and CO into CO₂ and H₂ at 400-500 °C that can provide additional hydrogen for the Haber ammonia synthesis process. Since then, the water-gas mixture is passed over the iron-chromium mixed oxide catalyst to shift the CO to CO₂ and generate additional hydrogen and industrially still used for high temperature WGS reaction.

The WGS reaction involves oxidation of carbon monoxide by steam to yield hydrogen and carbon dioxide as shown by the equilibrium reaction 1.1^{1,4-8}.



The water-gas shift reaction is moderately exothermic and reversible with a ΔH° of -41.1 kJ/mol of carbon monoxide. The equilibrium constant (K_p) of the WGS reaction as a function of temperature is given by^{6,8}:

$$K_p = \frac{y_{CO_2,eq} * y_{H_2,eq}}{y_{CO,eq} * y_{H_2O,eq}} = \exp\left(\frac{4577.8}{T} - 4.33\right), \text{ where } T \text{ is in } K \quad (1.2)$$

The CO equilibrium conversion is favored at lower temperatures because it is an exothermic reaction. The reaction is industrially accomplished in two packed-bed reactor stages: a high-temperature shift (HTS) stage and a low-temperature shift (LTS) stage^{1,4-8,11,12} in order to increase the conversion of this exothermic equilibrium reaction (higher equilibrium conversions are achieved at lower temperatures). With the aid of inter-bed cooling, ca 1% CO exit levels can be achieved by using two separate catalyst beds (Figure 1.1)⁷. HTS stage at 320-450 °C has fast kinetics, but CO conversion is limited by equilibrium. An equilibrium CO conversion is determined from the equilibrium constant and inlet gas composition. On the other hand, LTS stage at 180-250 °C has less thermodynamic limitations, but the reaction is controlled by the slow kinetics at these temperatures⁸. The lower limit of the operating temperature in the LTS reactor is the dew point of water at the operating pressure⁵. The effect of pressure is minimal because the WGS reaction is equimolar. Therefore, pressure does not affect the reaction equilibrium. However, pressure enhances the rate of reaction and pressures up to 3 MPa can be used¹³.

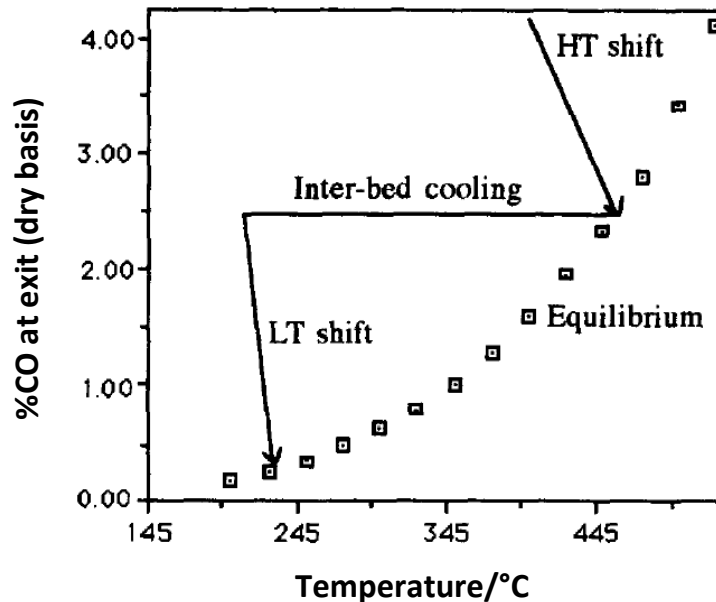
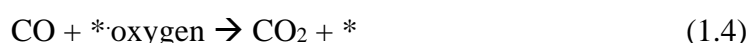


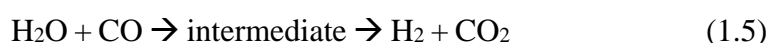
Figure 1.1. Typical variations of carbon monoxide levels in high temperature and low temperature shift catalyst beds⁷

The mechanisms of WGS reaction over the metal oxide catalyst are defined as “Regenerative Mechanism” and “Associative Mechanism”. The regenerative mechanism was first proposed by Armstrong and Hilditch (1920)¹⁴. This mechanism is mostly commonly applied for the high temperature water-gas shift reaction and is based on the oxidation-reduction cycle (redox mechanism), given as follows:



The oxidation state of the catalyst material is changed. The catalyst is oxidized by H₂O and to produce H₂. The catalyst is then reduced by CO and to yield CO₂. After these series reactions, the catalyst returns to its original, pre-reaction state.

The associative mechanism was also first proposed by Armstrong and Hilditch in 1920¹⁴ to explain the low temperature shift reaction¹. This mechanism is a Langmuir-Hinshelwood model where CO and H₂O adsorb and interact to form an adsorbed intermediate that decomposes to form CO₂ and H₂. This reaction is given as following:



Two most plausible surface reaction intermediates that have received the most attention are formate and carboxyl groups. Infrared spectroscopy is used to understand the intermediate species. Formate type intermediates are considered by many studies but there are uncertainties of the presence of formate species resulted from the reaction between the products of the WGS reaction, CO₂ and H₂. On the other hand, some experimental and theoretical (DFT) studies mostly over Cu catalyst show that the formate mechanism has low probability and the

carboxyl mechanism is feasible than the formate mechanism. Thus there is no undisputed conclusive mechanism for the WGS reaction¹.

Conventional Fe₂O₃-Cr₂O₃ catalysts contain about 80-90% (wt) of Fe₂O₃, 8-10% Cr₂O₃ and the balance being promoters and stabilizers like copper oxide, Al₂O₃, alkali, MgO, ZnO, etc.⁵. The conventional method to prepare the HT-WGS catalyst is by co-precipitation of the mixed iron and chromium nitrates with ammonium hydroxides⁵. With this method, the bulk hematite (α -Fe₂O₃ or γ -Fe₂O₃) phases are obtained upon calcination. This is followed by partial reduction by hydrogen or carbon monoxide whereby Fe₂O₃ is transformed to Fe₃O₄ (magnetite), which is the bulk catalytic active phase⁷.

The chromium in the Fe-Cr oxide HT-WGS catalyst has been used as a textural promoter to prevent the thermal sintering of Fe₃O₄ and concomitant catalyst loss of surface area. The Fe-Cr mixed oxide catalyst is used because of its high activity, durability, and reasonable manufacturing cost⁸. The commercial high temperature water-gas shift catalysts, however, possess 8-14 wt.% Cr₂O₃ with several wt.% Cr⁶⁺ compound¹⁵. Hexavalent chromium (Cr⁶⁺) is a toxic carcinogen, threatening human health, and the environment. US Occupational Health and Safety Administration enforces strict regulations regarding worker exposure to Cr⁶⁺ in several industries.⁸ European Restriction of Hazardous Substances also bans the use of Cr⁶⁺.⁸ Although trivalent chromium (Cr³⁺) has very low toxicity, during calcination at elevated temperatures some of the Cr³⁺ can be oxidized into toxic Cr⁶⁺.⁸

Because of the environmental and health concerns, alternative elements are investigated in many studies for replacing chromium with an equivalent element. Mostly aluminum is studied as a textural promoter (structural stabilizer)^{9,16}. Other examples of the replacement elements for Cr in Fe-based high temperature water gas shift catalysts have been Ce, Mo, Zr, and Nb¹⁷⁻²⁰.

1.2. Previous Studies

1.2.1. Powdered CuO-Cr₂O₃-Fe₂O₃ Catalysts

The co-precipitation method is conventionally used to obtain high temperature WGS catalyst, which is prepared as Fe₂O₃ and is transformed to Fe₃O₄ in the presence of large amounts of steam in order to prevent the metallic iron formation. This method involves the conventional co-precipitation of the mixed iron and chromium nitrates with ammonium hydroxides.⁵

Impregnation method was suggested by Pereira et al. (2008)²¹ for the preparation of active phase directly. They compared the chromium-doped magnetite catalysts which were prepared using precipitation and impregnation methods. The delay of the metallic iron production was provided by chromium independently of the preparation method. Lin et al.^{22,23} studied the co-precipitation of copper and iron oxide and concluded that the catalyst prepared by co-precipitation method possesses weak basic site, highly dispersed CuO crystals, and the best catalytic activity and stability for the WGS reaction.

Chromium in the Fe/Cr high temperature WGS catalyst has been used as textural promoter to prevent the thermal sintering of Fe₃O₄ and loss of surface area of the catalyst⁸. Chromium concentration percentage is important and should be optimized for both the textural properties and intrinsic activity since Cr³⁺ replaces the bulk Fe³⁺/Fe²⁺ octahedral sites²⁴. Edwards et al. (2002)²⁵ found that the chromia forms a solid solution within the Fe₃O₄ lattice and there are no discrete chromia phases. According to the X-ray photoelectron spectroscopy (XPS) and high spatial resolution energy dispersive X-ray analysis (STEM-EDX), an activated catalyst that is exposed to air is surface enriched in chromia and is thermodynamically more stable than the iron-rich core. This situation was thought to reduce iron diffusion and sintering effects.²⁵ Similar conclusions were reached by Pereira et al. (2008)²¹. X-ray diffraction (XRD) characterization showed that there is only one ordered phase which is magnetite. The iron and

chromium contents were determined by energy dispersive X-ray spectroscopy (EDS). Results of XRD and EDS showed that the amount of chromium on the surface is higher than in the bulk. Chromium is believed to act both in the bulk and on the surface preventing sintering.²¹ Although it has been proposed that the reduced catalyst forms an inverse spinel type structure with Cr³⁺ ions in solid solution within the Fe₃O₄ lattice, the role of Cr³⁺ is still unclear.²⁶

Another important topic is the mechanistic understanding of the nature of the WGS reaction pathways. The high temperature WGS reaction is generally described by the regenerative mechanism. Temperature-programmed desorption (TPD) study of Diagne et al. (1990)²⁷ after reaction and formic acid adsorption on Fe-Cr catalyst and chemical trapping of formate species showed that the concentration of formates decreased when the reaction temperature and the catalytic activity increased in the temperature range of 250-400 °C. After HCOOH adsorption at higher temperatures, they couldn't observe CO₂ desorption, which suggested that surface formate species were not the predominant intermediate species for the reactions at 300 °C and high.²⁷ At high temperatures, desorption and/or decomposition of surface intermediates such as formate and carbonate species will be very fast and will not be long-lived⁵. Borek et al. (1970)¹¹ directly measured the oxidation and reduction of an iron oxide-based catalyst with CO and H₂O and they established that the rates of reduction and oxidation of an iron oxide-based WGS catalyst by the CO and H₂O were in a good agreement with the rate conversion of CO in the WGS. Tinkle and Dumesic (1987)²⁸ performed isotopic exchange measurements to investigate the adsorption/desorption and the inter-conversion of CO and CO₂ over iron oxide-chromium oxide catalysts. They concluded that CO/CO₂ inter-conversion is fast compared with adsorption/desorption of CO and CO₂ and a common adsorbed species results from the adsorption of CO and CO₂. For the high temperature WGS reaction, the redox mechanism is considered as the dominant mechanism.⁵

Rhodes and Hutchings (2003)²⁹ studied the role of the copper promoter in the iron oxide/chromia catalyst for the high temperature WGS reaction. They found that the rate of reaction using both CuO/Fe₃O₄/Cr₂O₃ and Fe₃O₄/Cr₂O₃ catalysts was zero-order in H₂O and first-order in CO. The WGS activation energy for the Fe₃O₄/Cr₂O₃ catalyst was found to be 118±9 kJ mol⁻¹. The addition of CuO significantly decreased the WGS activation energy to 75-80 kJ mol⁻¹. Their TPR results with H₂ and CO showed that Cu²⁺ acting in solid solution providing resistance to reduction by CO relative to the unpromoted catalyst and thus they concluded that CuO partially stabilized the catalyst with respect to reduction with CO and that high partial pressure of CO could be used in the presence of CuO as a promoter.²⁹

Scariot et al. (2008)²⁴ characterized the activation process of a high temperature WGS Fe₂O₃/Cr₂O₃/CuO catalyst of by comparing that catalyst before activation and after activation. The hematite phase was used initially and it transformed to magnetite phase during activation. After the characterization by transmission electron microscopy (TEM), XRD, X-ray absorption spectroscopy (XAS), and XPS, they concluded that Cr ions are incorporated in the iron oxide lattice and there is no segregation to separate chromia phase. Moreover, the partial reduction of the initial Cu⁺² ions suggest that the reduction of the Cu species is complex and needs *in situ* characterization to fully understand the role of Cu in the catalyst.²⁴

Kappen et al. (2001)³⁰ studied the state of the copper promoter (0.17-1.5 wt%) in Fe-Cr high temperature shift catalysts by *in situ* fluorescence X-ray absorption fine structure (XAFS) combined with on-line gas analysis. They found that the reduction behavior of copper is dependent on the copper concentration: at lower copper concentrations (0.17 wt%), the reduction proceeds via a relatively stable intermediate Cu(I) phase and at relatively high concentrations, Cu is present as copper metal under working conditions. They observed that copper could not be removed from the catalyst by chemical extraction down to less than 0.17 wt%.

Puig-Molina et al. (2010)³¹ performed *in situ* XAFS measurements of Cu-promoted Fe/Cr-oxide based high-temperature water-gas shift catalyst at 380 °C and at 12 or 24 bar and found that copper is mainly present as segregated metallic particles on the magnetite surface under these conditions that promote the WGS reaction. Furthermore, very small amounts of copper is able to promote the catalyst suggesting that the magnetite surface is the active surface and that Cu facilitates the cycle of water dissociation and hydrogen production. The Cr promoter was found to be incorporated into the bulk magnetite phase as Cr³⁺ sites.

The Mössbauer and powder x-ray diffraction measurements of the study of Magalhaes et al. (2007)³² showed that the spinel crystalline phase is formed with initial substitution of Fe_{oct}³⁺ by Cr³⁺ and for higher Cr contents, chromium also replaces Fe_{oct}²⁺ and Fe_{tet}³⁺ in the crystalline structure.

Estrella et al. (2009)³³ investigated the reduction of CuFe₂O₄ and Cu/Fe₃O₄ catalysts with *in situ* time-resolved X-ray diffraction, X-ray absorption fine structure, and atomic pair distribution function analysis under WGS reaction conditions. The copper was initially present as Cu²⁺ in CuFe₂O₄ and became reduced to metallic Cu⁰ in the presence of the WGS reactants at 400-500 °C. The lattice of the mixed-metal oxides formed O vacancies that initially introduced stress and eventually collapsed the original crystal structure to form metallic Cu particles dispersed on Fe₃O₄, which were the active phases. The interaction of Cu⁰ with the iron oxide support, however, should not be neglected.³³

Patlolla et al. (2012)²⁶ studied the phases of iron oxide water-gas shift catalysts with the application of combined *operando* XAS/XRD/Raman-MS Spectroscopy. The supported 3% Cr₂O₃/Fe₂O₃ catalyst was synthesized by impregnation of an aqueous Cr-nitrate solution on a commercial α -Fe₂O₃. These *operando* spectroscopy measurements provided the information about the oxidation state, local atomic structure, crystal structure in the bulk and in the surface, before, during and after WGS reaction. They used Raman Spectroscopy at room temperature reaction. They concluded that the bulk Fe₃O₄ phase formed

after partial reduction of the supported 3% Cr₂O₃/Fe₂O₃ catalyst by CO at 400 °C. The initial surface CrO₄²⁻ was reduced to Cr⁺³ that were embedded in the bulk lattice of the iron oxide support and crystalline Cr₂O₃ nanoparticles were not present. It was also observed that chromium oxide enhanced the structural disorder of the magnetite phase of the supported 3% Cr₂O₃/Fe₂O₃ catalyst.²⁶

Rodriguez et al. (2013)³⁴ summarized the current status of *in situ/operando* studies for the production of hydrogen through the water-gas shift reaction on different metal oxide catalysts to identify the active phase during the WGS reaction and the reaction mechanisms for WGS over these catalysts. This perspective article mentions the lack of *in situ/operando* mechanistic studies for the WGS reaction over iron oxide catalyst.³⁴

In situ and *operando* spectroscopic analysis is required to understand the dynamic surfaces under reaction conditions³⁵. Recent *in situ* and *operando* IR, Raman, and XAS spectroscopy³⁶ and temperature programmed surface reaction (TPSR) spectroscopy³⁷ studies are guiding the understanding of the catalyst structure for iron-chromium oxide under the reaction conditions and the high temperature water-gas shift (HT-WGS) reaction mechanism. These *operando* spectroscopy studies of Keturakis et al. (2016)³⁶ with chromium-iron oxide catalysts prepared by incipient-wetness impregnation revealed that the initial surface (O=)Cr⁺⁶O₂ species reduced to Cr⁺³ and dissolved into the iron oxide bulk lattice. This was further supported by the *in situ* near ambient pressure X-ray photoelectron spectroscopy (NAP-XPS) and high-sensitivity low energy ion scattering (HS-LEIS) surface analysis study of Zhu et al. (2016)³⁸ directly showing that during the HT-WGS reaction Cr⁺⁶ reduces to Cr⁺³ with the Cr⁺³ dissolving into the bulk iron oxide lattice forming a solid solution. The Fe_{3-x}Cr_xO₄ solid solution also stabilizes the iron oxide phase from reducing to metallic Fe⁰.

The *in situ* TPSR (CO-TPSR, CO+H₂O-TPSR, and HCOOH-TPSR) spectroscopy study of Zhu and Wachs (2016)³⁷ of equilibrated Cu-Cr-Fe-O catalysts prepared by co-precipitation is the first study that demonstrated the

evolution of CO₂ and H₂ during CO+H₂O-TPSR follows a redox mechanism where the catalyst surface is first reduced by CO and subsequently re-oxidized by H₂O. This is a direct proof that the associative reaction mechanism does not take place for HT-WGS since both reaction products are not simultaneously evolved.

Additional insights about the state of Cu-Cr-Fe-O catalysts during HT-WGS was obtained from *in situ* NAP-XPS and HS-LEIS surface analysis by Zhu et al. (2016)³⁸. It was found that the initial Cu²⁺ cations dissolved in the iron oxide matrix reduce to metallic Cu⁰ nanoparticles (~3 nm) on the external surface of the iron oxide. Furthermore, HS-LEIS spectroscopy indicates that the Cu nanoparticles are covered by ~1/3 monolayer of FeOx. Chemically probing reactivity with CO-TPR probe showed that Cu facilitates the removal of O from the catalyst by CO, which is the rate-determining-step for the HT-WGS reaction.

Isotopic C¹⁶O₂/C¹⁸O₂ switch and H₂-TPR experiments^{36,39} revealed that the HT-WGS reaction over iron oxide catalysts only involves oxygen from the surface layer (surface Mars-van Krevelen mechanism). This allows for quantitative determination of the number of catalytic active sites by an isotopic switch measurement and for the first time to calculate the turnover frequency (TOF).³⁹ It was found that Cr is only a textural promoter that increases the number of active sites because of increasing the catalyst surface area by ~2x and does not affect the TOF. The Cu, however, is a chemical promoter that increases the TOF by ~3x and does not affect the catalyst surface area. The net effect of both Cr and Cu promotion is to increase the overall catalyst activity by ~6x.

1.2.2. Powdered Cr-Free Iron Oxide Catalysts

Some of the elements investigated as possible replacements for Cr in Fe-based high temperature water-gas shift catalysts are Al, Zn, Ni, Co, Mg, Ti, Si, Mo, Ce, Zr, and Nb in^{2,8,9,16-20,40-45}. De Araujo and Rangel (2000)^{9,40} studied an aluminum doped catalyst and also with small amounts of copper. It was observed

for the spent catalyst that the aluminum and copper atoms went into the magnetite structure (*ex situ* inductively coupled plasma atomic emission spectroscopy (ICP/AES)). After catalytic activity test and surface area analysis (BET method), they concluded that aluminum led to a slight increase in activity; on the other hand, copper increased both the activity and the activity per area.

The *in situ* NAP-XPS study of Ye et al. (2013)⁴⁶ suggested that the surface region of Fe-Cu-Al-O was reconstructed into a double-layer structure consisting of surface layer of Fe₃O₄ and a metallic Cu layer below it upon treatment at 350 °C. Based on surface sensitivity of XPS, the thickness of the Fe₃O₄ layer could be approximately 2 nm. The strong metal (Cu)-oxide (Fe₃O₄) interface effect of this double layer structure enhances the catalytic activity of Fe₃O₄ in WGS.

Ozkan's research group¹⁶ also investigated aluminum to be a potential chromium replacement in HTS catalyst. They compared the activity of chromium (Fe-Cr), aluminum (Fe-Al), gallium (Fe-Ga), manganese (Fe-Mn) doped and un-doped (Fe-only) hematite catalysts. According to CO conversion using fixed-bed flow system with 1/1 as CO/H₂O ratio at 400 °C, Fe-Al showed higher activity than Fe-Ga and Fe-Mn and comparable activity to unpromoted Fe. Although aluminum stabilizes the magnetite phase by retarding its further reduction to FeO or metallic iron, the highest activity belongs to Fe-Cr oxide catalyst. Bao et al. (2012)⁴⁷ studied the effect of Fe/Cu molar ratio in Fe-Al-Cu catalyst for WGS under a hydrogen-rich atmosphere and they concluded that Fe/Cu molar ratio of 1:1 gives the highest CO conversion (97.4% at 350 °C) with 174 m²/g BET surface area of fresh catalyst. They observed good activity of Fe-Al-Cu catalysts at 250-550 °C and obtained 87.3% and 84.6% of CO conversions at 250 °C and 550 °C, which shows that Cu provides additional active sites at lower temperature and acts as an electronic promoter in solid solution at higher temperature.

Zhang et al. (2006)²⁰ studied the effect of addition of ZrO₂ and Nb₂O₅ promoters on the activity and stability of the Au/Fe₂O₃ catalysts in the WGS

reaction under hydrogen-rich conditions. The addition of ZrO_2 and Nb_2O_5 into iron oxide catalyst increases the surface area, decreases the magnetite crystallite sizes, and enhances the catalyst activity in the long-term WGS activity test at 200 °C. From XRD patterns, they did not observe ZrO_2 peak and they discussed this situation as the indication of high dispersion or an amorphous form of ZrO_2 in the prepared catalyst. They concluded that ZrO_2 and Nb_2O_5 acted as structural promoters.²⁰

Bliem et al. (2015)⁴⁸ studied the adsorption and incorporation of Ni, Co, Mn, Ti, and Zr at the Fe_3O_4 (001) surface by scanning tunneling microscopy, x-ray and ultraviolet photoelectron spectroscopy, low-energy electron diffraction, and density functional theory (DFT). They concluded that Zr is fully incorporated and the lowest energy configuration occurs when the foreign metal atom occupies a subsurface octahedral site.

Gangwar et al. (2016)⁴⁹ studied the structural and magnetic characterization of Zr-substituted magnetite prepared by wet chemical route. They concluded that XRD analysis shows the single-phase nature of the sample with continuous decrease in the lattice parameter by the substitution of Fe ions by Zr ions. The Zr^{4+} ions occupy both tetrahedral and octahedral sites by substituting for the Fe^{3+} ions. They observed the dissociation of physically and chemically adsorbed water with low Zr, and the ferromagnetic behavior of Zr-substituted magnetite samples.⁴⁹

Hakeem et al.⁵⁰⁻⁵³ studied the water-gas shift reaction over un-doped and doped Fe_2O_3 - ZrO_2 at 21 bar and high temperatures (623-773 K). According to H_2 -TPR⁵⁰ measurements, bulk Fe_2O_3 was completely reduced to metallic iron (Fe_2O_3 to Fe_3O_4 at 656 K and Fe_3O_4 to Fe at 805 K). For the doped Fe_2O_3 - ZrO_2 , iron oxide was only reduced ~60% and Zr prevented the complete reduction of iron oxide to metallic iron.

Ladebeck and Kochloefl (1995)⁵⁴ studied the co-precipitated Cr-free iron based catalysts (Fe_2O_3 : 90 wt%, Al_2O_3 : 5wt%, CuO : 2.5 wt%, and other metal oxides (ZrO_2 , MnO_2 , La_2O_3 , and CeO_2) with 2.5 wt%). The iron catalyst

containing CeO₂ was found the most active at 350 and 370 °C and stabilized the activity after four aging cycles. The activity retention after four aging cycles expressed the high thermo-resistance of the CeO₂-promoted Fe₂O₃ catalyst.

Yamaguchi et al. (2010)⁵⁵ investigated the redox performance of Zr-Ce modified iron oxide catalysts to produce hydrogen by reforming natural gas at 750 °C in a fixed-bed reactor. They also tested the cyclic stability of produced catalysts. Co-precipitation method was carried out using nitrates as oxide precursors and urea as the precipitating agent. They concluded that CeO₂ improved the overall oxygen storage capacity of Ce-Fe oxide catalyst. That increased the H₂ yield, however; only ZrO₂ or CeO₂ addition to Fe oxide catalyst did not show good performance. In the second cycle, they saw a dramatic decrease of the performance of Ce-Fe oxide catalyst. Addition of Zr to the Ce-Fe oxide catalyst provided the same performance even after 8th cycle. The addition of Zr to the Ce-Fe oxide catalyst provides better thermal stability and prevents the dramatic decrease of the performance of Ce-Fe oxide catalyst.

Ceria is a very good promoter of the water-gas shift reaction, which can be linked to the fact that its hydroxyl groups are extremely mobile and reactive. This function can also be related to having high oxygen storage capacity of ceria and the ability to shift easily between oxidized and reduced state (Ce⁴⁺ ↔ Ce³⁺). The oxygen storage capacity (OSC) is related to the most reactive oxygen species and the most readily available oxygen atoms. OSC may characterize the dynamics of the system.⁵⁶

Ceria is a rare earth metal and has high oxygen mobility and oxygen vacancy. The OSC plays an important role in the WGS reaction and this capacity is increased when coupled with a metal.² Pradhan et al. (2009)⁵⁷ have studied the copper supported ceria and copper supported ceria-zirconia catalysts for the water-gas shift reaction and they observed that presence of Zr⁴⁺ in the structure enhanced the structural stability of ceria towards sintering according to the corresponding surface area.

Ou et al. (1999)⁵⁸ examined the mechanically mixed CeO₂- γ -Fe₂O₃ catalyst for the water-gas shift reaction. Because of the preparation method, they observed CeO₂ peaks in XRD and concluded that the main effect of CeO₂ on iron-oxide catalyst is not a structural one, but the reason is the valence change of CeO₂ and the electronic effect on catalytic activity.

Reddy et al.^{59,60} studied the co-precipitated Fe-Ce-Cu (10:1:0.25) catalyst for high temperature water gas-shift reaction. They observed that copper has a negative effect on the activation of this catalyst. The XRD results exhibited that activation of the catalyst leads to formation of the wustite (FeO) phase. The addition of Cu to the Fe/Ce catalyst decreases the transition temperature of hematite to magnetite and the transition temperature of magnetite to wustite. XPS and Mössbauer results show that Cu and Ce enter into the octahedral site of magnetite and form the wustite phase along with the magnetite phase. The lower performance of the Fe-Ce-Cu catalyst than Fe-Ce catalyst was attributed to the presence of the FeO phase.

Cerium can cycle easily between reduced and oxidized states (Ce³⁺ \leftrightarrow Ce⁴⁺) that is the crucial role for redox catalysis. At elevated temperatures, however, the catalytic efficiency of ceria may be reduced as a consequence of sintering and loss of surface area.⁶¹ The study of Zerva and Philippopoulos (2006)⁶² showed the influence of the preparation method on the activity of copper-doped cerium catalysts for the water-gas shift reaction. They observed that aqueous solutions resulted in higher specific surface areas. The catalysts prepared by co-precipitation showed lower specific surface areas than the catalysts prepared by impregnation. The catalysts prepared by co-precipitation, however, possessed the highest activity at 300-350 °C.

Reddy et al. (2011)⁶³ studied the effect of the amount of cerium doping in Fe-Ce co-precipitated catalysts. The XRD results revealed that cerium could be incorporated into hematite up to a Fe/Ce atomic ratio of 10:2. Further increase of cerium leads to a separate bulk CeO₂ phase. Cerium oxide was found to promote the reduction of hematite to magnetite during H₂-TPR. Mössbauer

spectroscopy indicated that addition of Ce replaces Fe^{2+} and Fe^{3+} ions at bulk octahedral sites in equal amounts and optimal amounts of cerium to hematite stabilizes the magnetite phase during the WGS reaction. The Fe/Ce catalyst with a ratio of 10:2 exhibited the highest activity in a fixed-bed reactor (400 and 500 °C).

In heterogeneous catalysis, several applications involving Nb compounds as a promoter or as a support for other metals mainly due to increasing the catalytic activity and stability of the catalyst have been reported.^{64,65} Nb-doped iron oxide catalyst is interesting because of the comparable ionic radius of Nb^{5+} with Fe^{3+} , and this dimension similarity favors niobium to isomorphically replace iron in the iron oxide structures.⁶⁴⁻⁶⁶

Silva et al. (2009)⁶⁴ studied co-precipitated Nb-containing hematite catalysts for degradation reactions in the presence of H_2O_2 or ultraviolet light. Mössbauer measurements suggested the formation of the crystalline phase with partial substitution of Fe^{3+} by Nb^{5+} . This was accompanied by a significant increase in the BET surface area due the decrease in particle size and pore diameter (XRD and Mössbauer analyses). Moreover, they studied the reduction of the structure with H_2 by doing TPR experiments. During H_2 -TPR, a reduction peak appeared at 449 °C and a second broad peak at 500-700 °C. From comparison of the H_2 -TPR profile with XRD analysis of hematite, it was concluded that the structure after first reduction peak is for the magnetite phase. After H_2 -TPR analysis of Nb-doped hematite, the first shifted to 551 °C and the second broad peak remained the same. It was concluded that, niobium is in the structure of hematite and was expelled from the structure after the first reduction. Therefore, niobium did not affect reduction of the magnetite phase.

Rahim Pouran et al. (2015)⁶⁶ studied niobium substituted magnetite for wastewater treatment. During the preparation of the samples, they used N_2 flux to prevent Fe^{2+} oxidation and just obtain magnetite phase. They selected different amounts of Nb and observed from XRD and BET analyses that magnetite inverse spinel structure was maintained, and there was a significant

decrease in crystal size (~two times) and increase in specific surface area (~three times). The imported Nb^{5+} ions substituted the octahedral Fe^{3+} cations that are mainly exposed on the surface and contributed to the increase in surface area by primarily reducing the pore size of the particles.

1.2.3. Well-Defined Model Catalysts

Joseph et al.^{67,68} investigated the adsorption of water on epitaxial Fe_3O_4 (111) films with scanning tunneling microscopy (STM), low-energy electron diffraction (LEED), photoelectron (ultraviolet photoelectron spectroscopy (UPS), XPS) and thermal desorption spectroscopy (TDS). They found that on the surface terminated by $\frac{1}{4}$ monolayer of Fe atoms (Fe_{tet1}) located over a closely packed oxygen layer, water dissociates to form adsorbed OH groups. From LEED pattern and STM images, they understood the dominant type of defects on the surface from the missing protrusion as the Fe vacancies. The concentration of defects changes from film to film⁶⁹. They observed the maximal concentrations of Fe vacancies to be 30%. The saturation coverage ($\sim 2 \times 10^{14}$ water molecules cm^{-2}) corresponds to about one OH+H per Fe atom exposed on the regular Fe_3O_4 (111) surface (3.3×10^{14} molecules cm^{-2}), which is much higher than the surface defect concentrations. Therefore, the dissociation of water on Fe_3O_4 (111) was not related to defects but took place predominantly on regular surface areas. After water dissociation, the resulting surface OH^- group remains at the Fe site and surface H^+ species coordinate onto a neighboring O site.⁶⁷

The STM, LEED, XPS study of Paul et al. (2007)⁷⁰ showed that the stoichiometric surface corresponds to the regular Fe_{tet1} termination for the Fe_3O_4 (111) single-crystal surface. Cutting et al. (2008)⁷¹ have examined the surface structure of the ultra-high vacuum (UHV) prepared (111) terminated surface of single crystal Fe_3O_4 and the STM results indicated that the dissociation of H_2O takes place on a termination of Fe_3O_4 (111) that contains a $\frac{1}{4}$ monolayer of

$\text{Fe}_{\text{tetl}}^{3+}$. They discuss the differences of the dissociation on $\text{Fe}_{\text{oct}2}^{2+}$ for the thin film.

1.2.4. Theoretical Studies of Iron Oxide Catalysts

Experimental and Density Functional Theory calculations are complementary for investigating the fundamental details of surface reactions. This has led to theoretical studies of (100), (110), and (111) surfaces of Fe_3O_4 both as clusters and slab surface structures.

Van Natter et al. (2008)⁷² studied the (100), (110) and (111) surfaces of Fe_3O_4 , where octahedral cations contain both Fe(II) and Fe(III), by DFT models for the high temperature water-gas shift reaction. They optimized small clusters of Fe_3O_4 surfaces using Jaguar, version 7.0 with B3LYP hybrid exchange and correlation functions and TZV** basis sets. They preferred the microkinetic model of redox mechanism, which involves only the vacant sites and sites containing an oxygen adatom. According to this study, the minimum energy of localization of an oxygen adatom (-668 kJ mol^{-1}) belongs to (111) surface of Fe_3O_4 . They have also shown the result of Bohlbro's study^{73,74} of the microkinetic model for water-gas shift over ferrochrome catalyst. The enthalpy of localization of a surface oxygen adatom was calculated as -611 kJ mol^{-1} using Bohlbro's published data. Since the experimental studies established the chromium as a textural promoter, they did not expect that the presence of chromium atom in the cluster model would affect the results, therefore, their catalyst clusters did not include the chromium atoms.⁷²

Van Natter et al. (2009)⁷⁵ also reported the effect of copper promotion upon cluster models for sites on the {111} surface of Fe_3O_4 . A copper atom substitutes in place of Fe cation with the formal charge of +2. It was a DFT study, which investigated the strength of bonding of water-gas shift intermediates (oxygen, carbon dioxide, and dissociated water). They concluded that the bonding energy of the intermediates decreases with copper substitution. The

bonding energy decrease is much more if copper cations substitute for iron cations in the surface of the catalyst than for iron cations below the surface of the catalyst.⁷⁵

DFT studies using Vienna ab initio simulation package (VASP) with the projector-augmented wave (PAW) method and generalized gradient approximation (GGA) by including the Hubbard parameter U (U-J=3.8 eV) show that the optimized lattice parameter of the bulk Fe₃O₄ structure is close to the experimental value and the most stable surface is (111) with Fe_{tet} (1/4 monolayer of iron over a close-packed oxygen layer underneath) and Fe_{oct} (two layers of iron over a close-packed oxygen layer) terminations.⁷⁶⁻⁷⁸

Yang et al. (2010)⁷⁹ studied the surface structures of Fe₃O₄ (111), (110), and (001) with DFT calculations. According to this study, the computed surface free energy indicated that (111) is less favorable thermodynamically than (110) and (001), and the formation of (111) should be kinetically controlled, the (111) surface maybe more active for reactions, and Fe_{tet2} and Fe_{oct-} were the most stable terminations of (111) surface.

Yu et al. (2012)⁷⁶ studied the structures and stabilities of the Fe₃O₄(111), (001) and (110) surface terminations with DFT calculations by including the Hubbard parameter U (GGA+U). They found the ideal U value as 3.8eV according to the similarity of lattice parameter of *a* (8.405 Å) with the experimental value (8.396 Å). According to the their study, surface stability was on the order of (111)>(001)>(110). It is possible to get 6 non-equivalent bulk termination on (111) surfaces. Among these terminations, Fe_{tet} which exposes 1/4 monolayer of iron over a close-packed oxygen layer underneath and Fe_{oct} which exposes two layers of iron over a close-packed oxygen layer were given as the most stable terminations with lowest energy.⁷⁶

Santos-Carballal et al. (2014)⁷⁷ studied Fe₃O₄ crystals by using DFT methods within the GGA+U approximation. They have concluded that Fe-terminated (001) and (111) planes are the most stable Fe₃O₄ surfaces and the O

vacancies are likely to migrate towards the bulk with changing the phase structure.

Kiejna, Ossowski and Pabisiak (2012)⁸⁰ presented a detailed DFT and DFT+U study of the clean magnetite (111) surface and showed that inclusion of on-site Coulomb correlations in the GGA+U approach modifies the electronic structure of magnetite surfaces and half-metallic character of the surfaces were calculated with the GGA+U.⁸⁰

Some studies have investigated the reactants of WGS reaction separately. Grillo et al. (2008)⁷⁸ investigated water adsorption on Fe₃O₄(111) surfaces with different surface termination. They calculated with DFT and the GGA in the VASP package with special treatment of on-site Coulomb interactions (U-J=3.8 eV). Their study showed that ¼ monolayer termination of iron on top of a full oxygen layer is consistent with low-energy electron diffraction analysis, however, the calculated negative slope of the surface energies versus oxygen partial pressure showed that a ½ monolayer iron termination would become stable under oxygen poor conditions. Initially, water dissociatively adsorbs and saturates when all Fe sites are occupied by OH groups while the H atoms bind to surface oxygen. After saturation, they observed hydronium ion like structure OH₃⁺-OH after bridging the OH and H groups.

The other groups observed similar results. Yang et al. (2009)⁸¹ studied the structures and energetics of water adsorption on the Fe₃O₄ (111) surfaces with different surface termination using DFT. They concluded that Fe_{tet1} terminated Fe₃O₄ (111) with the energy of -1.25 eV is more favored for water adsorption than the Fe_{oct2} terminated surface. They have observed the dissociative adsorption of water on Fe_{tet1} termination of Fe₃O₄ (111) surface; however, there is molecular adsorption on Fe_{oct2} surface. Zhou et al. (2010)⁸² suggested that water dissociative chemisorption to form a surface hydroxyl group and a H atom on Fe_{oct-tet1} terminated Fe₃O₄ (111) surface with the energy of -1.33 eV is more favorable than Fe_{tet1} terminated surface. Li and Paier (2016)⁸³

concluded that water adsorbs dissociatively and strongly exothermic on the $\text{Fe}_{\text{oct}2}$, and molecularly adsorbs on the $\text{Fe}_{\text{tet}1}$ termination is molecularly.

Huang et al. (2006)⁸⁴ studied the slab of 4-layered iron and 4-layered oxygen atoms for CO adsorption on Fe_3O_4 (111) surfaces and they have found that CO adsorption on $\text{Fe}_{\text{oct}2}$ terminated Fe_3O_4 (111) surface is more stable than on the $\text{Fe}_{\text{tet}1}$ terminated surface. On-top configuration is the most favored bridge-like configuration by CO interacting with the neighbor Fe atoms and the surface O is also favored for the $\text{Fe}_{\text{oct}2}$ terminated surface.

According to the results of STM images and theoretical simulations, Rim et al. (2012)⁸⁵ observed that water species present on the Fe-terminated Fe_3O_4 (111) surface, low energy barrier belongs to water dissociation with OH atop surface termination Fe^{3+} sites and H atop under-coordinated oxygen sites and CO and H_2O compete for the Fe^{3+} binding sites, and dissociated water molecule (OH+H) is the most stable state.

Huang et al. (2015)⁸⁶ studied the reaction mechanism of the water-gas shift reaction on the Fe_3O_4 (111) surface with the $\text{Fe}_{\text{oct}2\text{-tet}1}$ termination using DFT calculations. They mainly compared a redox mechanism, in which CO is oxidized by the oxygen atom abstracted from the water molecule, an associative mechanism, in which a *COOH intermediate species is initially formed and subsequently decomposed into COO^* and H^* , and a coupling mechanism, in which a COO^* species is directly formed through the surface rearrangement of the OH and CO species without going through OH dissociation and COOH formation. They concluded that the energetically most favorable pathway is the redox mechanism where desorption of CO_2 is the rate-limiting-step.

Dementyev et al. (2015)⁸⁷ reported the first direct calorimetric measurement and infrared reflection absorption spectroscopy (IRAS) investigation of water interaction with a well-defined model Fe_3O_4 (111) surface grown on top of Pt(111) under ultrahigh vacuum conditions and compared the findings with DFT. They concluded that the surface OH groups formed upon water dissociation establish a very stable complex with molecular water. The

DFT calculations showed that $\text{Fe}_{\text{oct}2}$ and $\text{Fe}_{\text{tet}1}$ terminations are comparably stable in the surface energy and are the most stable ones for a broad range of oxygen chemical potentials. With single water molecule adsorption, non-dissociative adsorption of water on $\text{Fe}_{\text{tet}1}$ surface was found in contrast to the $\text{Fe}_{\text{oct}2}$ terminated surface. They claimed that a dimer-like structure with two water molecule is reasonable with the similar results of adsorption energies and vibrational frequencies of experimental and theoretical results.

Fu et al. (2015)⁸⁸ reported effect of Cu doping on (2x2) Fe_3O_4 (111) surface with the $\text{Fe}_{\text{tet}1}$ termination in the DFT of water-gas shift reaction. In order to see the effect of Cu, they replaced one Fe atom on different positions with one Cu atom. They examined the substitution effect of Cu by the adsorption of CO and H_2O as the reactants of WGS reaction. The adsorption energy of CO on the Fe atom was calculated as 0.54 eV, on the other hand CO adsorbed on Cu atom with the energy of 0.96 eV. The adsorption energies of H_2O on Fe and Cu atoms were calculated as 0.92 eV and 0.73 eV, respectively. The doping effect of Cu on the catalyst activity was attributed to strengthening the CO adsorption and inhibiting the excess water molecules from covering the active sites, improving the activity of other Fe ions for reactant adsorption, and enhancing the co-adsorption the reactants to facilitate the WGS reaction of CO and H_2O .⁸⁸

Guvelioglu et al. (2005)⁸⁹ performed DFT calculations of small copper clusters for dissociative chemisorption of hydrogen and they used lowest number of 7 for the triangle pyramidal clusters. Chen et al. (2010)⁹⁰ have studied water adsorption on the pentagon bipyramid Cu_7 cluster with DFT calculations and found that the water molecules were preferentially adsorbed on the pentagon sites, the first dissociation step to form OH and H species was exothermic with a moderately high barrier. They also concluded that the size of the cluster does not have significant effect on water dissociative chemisorption after calculating same steps on Cu_{10} .

Xue et al. (2015)⁹¹ examined the adsorption of CO and H_2O on the small Cu_x ($x=1-4$) cluster modified Fe_3O_4 (111) surface ($\text{Fe}_{\text{tet}1}$) in order to figure out

the mechanism for the promoting effects of the Cu-modified Fe₃O₄ catalysts. They investigated linear, regular triangle and regular tetrahedron shapes according to the number of Cu. The copper atoms tended to bind with the surface oxygen atom. It was concluded that for pure Fe₃O₄ surface, the adsorption energies of CO and H₂O were -0.44 and -1.26 eV, respectively (adsorption occurs on Fe atom for both molecules), on the other hand, the presence of Cu clusters weakened the adsorption of H₂O and strengthened the adsorption of CO. From the calculation of the co-adsorption of a second adsorbate (CO or H₂O), they concluded that the adsorption energies of the second adsorbate were less than a single molecule.⁹¹

Model catalysts and slab model-DFT results show that the (111) surface is the most stable surface and Fe_{tet1} and Fe_{oct2} are the most stable terminations of (111) surface. Magnetic properties of magnetite and the on-site Coulomb correlations should be included in DFT calculations to obtain the close values to the experimental ones like lattice parameter, net magnetic moment, elastic modulus etc. Although there are counter-views on the adsorption type of H₂O, many studies observed the dissociative adsorption of water on Fe_{oct2} termination of (111) surface of Fe₃O₄. There is a lack of DFT study for chromium substitution on magnetite structure. On the other hand, copper effect has been studied as copper cluster or copper atom substitution on the structure. All these studies show that there is an effect of copper on the adsorption energies of CO and H₂O.

1.3. Motivation and Research Objectives

The importance of the HT-WGS reaction motivates further research on this reaction to obtain fundamental insights at the molecular- and atomic-scale about the surface and bulk structures, catalytic active sites, and finding non-toxic promoters that can substitute for Cr.

There are three key questions:

(i) What is the catalytic active site of the HT-WGS catalyst?

There is a phase transformation of the iron oxides during the HT-WGS reaction and a challenge is to characterize and determine the catalytic active site, which is an unclear point. The general roles of the chromium and copper in the Fe oxide-based HT-WGS catalyst system still need to be investigated to obtain a molecular- and atomic-model of this important catalytic system.

(ii) What are the possible elements that can substitute for chromium?

Some environmental and health issues are caused by the presence of Cr⁶⁺ in this catalyst system forces us to investigate a replacement for chromium to be structural promoter which prevents thermal sintering of iron oxide at high temperatures. In the present study, zirconium, cerium and niobium are proposed as potential promoters for Cr-free iron oxide-based catalysts. The main question is to determine if these elements act as structural promoter that prevent thermal sintering and provides HT-WGS activity as high as the Cr-promoted iron oxide-based catalysts.

It is difficult to find answers to these questions by classical *ex situ* characterization methods because of the dynamic nature of the catalyst, especially the surface, in different environments. *In situ* measurements of the catalysts can establish the chemical state, structural properties, relation between structure and catalytic activity under the reaction conditions. Moreover, theoretical investigation provides the information of the reaction pathway, the geometries and energetics of reactants and products, and transition states. It is also possible to define the catalytic active sites for the HT-WGS catalytic reaction.

This Ph.D. study is a combined theoretical and experimental approach. The theoretical investigation was carried out at the METU Computational Laboratory. The Density Functional Theory (DFT) method was applied by utilizing VASP (the Vienna ab initio simulation program) codes. The calculations were performed at TUBITAK (Scientific and Technical Research

Council of Turkey) ULAKBIM, High Performance and Grid Computing Center (TR-Grid e-Infrastructure). The complementary experimental studies of Cr-free iron oxide catalysts were carried out at Lehigh University's *Operando* Molecular Spectroscopy & Catalysis Research Laboratory. In summary, the objective of this research is to apply the complementary theoretical and experimental studies to investigate the high temperature WGS catalytic reaction system at the molecular- and atomic-scales over iron based oxide catalysts.

1.4. Thesis Outline

Background information about Raman Spectroscopy and Low Energy Ion Scattering analyses and the experimental methodology are given in Chapter 2. The background information on computational chemistry and characterization developments and the details of all computational methodology are provided in Chapter 3. Chapter 4 summarizes the results of LDA+U approach for WGS over oxygen terminated Fe_3O_4 (111) surface of Cr_2O_3 - Fe_2O_3 catalysts. Chapter 5 provides the results of the spin-polarized GGA(91)+U calculations of WGS over iron terminated Fe_3O_4 (111) surface of CuO - Cr_2O_3 - Fe_2O_3 catalysts. Copper is modelled as Cu_4 cluster on the $\text{Fe}_{\text{oct}2}$ surface. Mainly redox property of the terminations and the adsorption of the CO and H_2O molecules were investigated. In Chapter 6, the Zr, Nb, Ce, and Al promoted iron oxide catalysts will be compared after the investigation by XRD, *in situ* Raman Spectroscopy, High-Sensitivity Low Energy Ion Scattering, and flow BET surface area as characterization technique under the WGS reaction conditions except XRD. Moreover, the catalytic activity of the prepared catalyst were obtained with the steady-state measurements. Chapter 7 presents the conclusions and future outlook.

CHAPTER 2

EXPERIMENTAL METHOD

2.1. Characterization Developments: *Operando* and *in situ* Approach

The limitation of accessing to atomic-scale information about the state of the heterogeneous catalysts while the catalysis is taking place has been left for a few decades by the development of *in situ* techniques and the *operando* studies⁹²⁻⁹⁵.

In situ studies refer to the real-time investigation of a catalyst, typically by spectroscopy or microscopy techniques, during exposure to reactants or other external stimuli. In *operando* studies, the catalyst is interrogated via one or more spectroscopy or microscopy techniques under realistic reaction conditions with simultaneous real-time online analysis of reaction product. By this way, the catalysts can be probed directly under working conditions⁹⁴.

The structure of a heterogeneous catalyst is dynamic and depends intimately on the reaction conditions. Moreover, the surface reconstruction may also result in complete morphology changes. The active state of a catalyst only exists during the process of catalysis emphasizes the need for *operando* conditions. Therefore, direct links between the catalytic activity and the surface chemistry/surface structure can be established. Establishment of whether adsorbed species are reaction intermediates involved in the catalytic reaction or whether they are just spectator species occupying sites on the surface can be obtained by temperature programmed surface reaction. Moreover, the combination of different types of *in situ* and *operando* measurements may provide very detailed insight into the reaction mechanism⁹².

In order to characterize the catalytic systems, spectroscopic analysis are important. The reaction environment shapes the state of a working catalyst leading to an information gap between its structures as determined before or after

operation (*ex situ*), in controlled atmosphere (*in situ*), or under real working conditions. Real-time spectroscopy during operation to bridge the gap is named as *operando* methodology. The term *operando* is used to emphasize the simultaneous evaluation of both catalyst structure and catalytic performance^{95,96}.

- **Raman Spectroscopy:** Raman Spectroscopy is based on the inelastic scattering of photons, which lose energy by exciting vibrations in the sample. In this process, monochromatic light of frequency, ν_0 falls onto a sample, where the majority of the photons undergoes Rayleigh (scattering without energy exchange). The molecule is excited to an unstable state with energy, $h\nu_0$ above the ground state, then it decays back to the ground state. During this, energy is not exchanged between the molecule and the photon. However, when the excited molecule decays to the first vibrational level with frequency ν_{vib} , it effectively takes an amount of energy equal to $h\nu_{\text{vib}}$ away from the photon. Thus, the scattered light exhibits intensity at the frequency $\nu_0 - \nu_{\text{vib}}$ which is Raman peak called as Stokes band. Raman spectroscopy provides insight into the structure of oxides, and the coordination of metal oxide sites⁹⁷⁻¹⁰¹. There are the application of Raman spectroscopy in catalysis under *in-situ* or *operando* conditions. *In-situ* and *operando* Raman cells are designed as catalytic reactors which provides to obtain simultaneous structure and catalytic data without mass or energy transfer limitations, bypassing or back-mixing⁹⁶.
- **Low-Energy Ion Scattering (LEIS):** This technique is a unique tool in surface analysis, since it provides the atomic composition of the outer atomic layer. In catalysis, LEIS is applied in order to understand and improvement of catalysts, site of poisoning, quantification of promoters and size of nanoclusters. In LEIS, a sample is bombarded with noble gas ions (He^+ , Ne^+ or Ar^+) with energies between 0.5 and 10 keV^{102,103}. LEIS

is an exclusively sensitive for the outer surface layers. Because, the incident ion is neutralized inside the solid and the majority of ions that reach the detector must have scattered off the outermost layer and the detection of low-energy particles requires an electrostatic analyzer, thus; only ions can be detected and backscattered neutrals are not measured⁹⁷. The ion beam is directed towards the surface at an angle with respect to the surface normal and only projectiles that are backscattered into a certain solid angle element are analyzed (Figure 2.1⁹⁷). For quantitative surface analysis, only the signal of scattered ions is analyzed¹⁰². In general ion scattering a beam of ions with energy E_i scatters elastically from atoms in a solid. Scattering process is described by the laws of classical mechanics. The energy of the outgoing ion is determined by the laws of energy and momentum conservation, and reveals the mass of the target atom from which it scattered⁹⁷:

$$K_M = \frac{E_f}{E_i} = \left(\frac{(M^2 - M_{ion}^2 \sin^2 \theta)^{1/2} + M_{ion} \cos \theta}{M + M_{ion}} \right)^2 \quad (2-1)$$

where:

- K_M is the kinematic factor, equal to E_f/E_i ;
- E_i is the energy of the incoming ion;
- E_f is the energy of the scattered ion;
- M_{ion} is the atomic mass of the incoming ion;
- M is the atomic mass of the scattering atom in the sample;
- θ is the scattering angle.

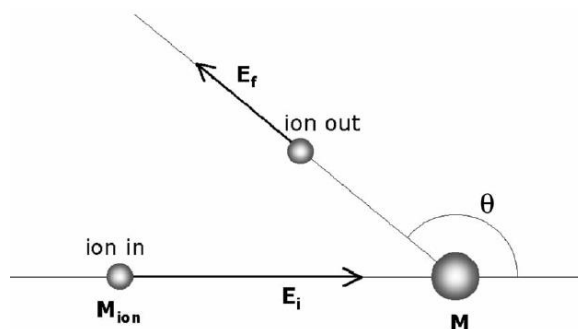


Figure 2.1. Geometry of an ion-scattering experiment. An incident ion with mass M_{ion} and energy E_i collides with a sample atom of mass M and loses energy. Its final kinetic energy E_f , after scattering over an angle θ is a measure for the mass of the target atom⁹⁷

2.2. Experimental Procedure

2.2.1. Catalyst Preparation

Zirconium, cerium, niobium, chromium, aluminum, and copper doped iron oxide catalysts were prepared by using zirconyl nitrate hydrate ($ZrO(NO_3)_2 \cdot H_2O$, Sigma-Aldrich 99.99% trace metal basis), cerium nitrate ($Ce(NO_3)_3 \cdot 6H_2O$, Alfa Aesar), niobium (V) oxalate hexahydrate ($Nb(HC_2O_4)_5 \cdot 6H_2O$, Alfa Aesar), chromium (III) nitrate nonahydrate ($CrN_3O_9 \cdot 9H_2O$, Sigma-Aldrich 99.997% trace metal basis), aluminum nitrate nonahydrate ($AlN_3O_9 \cdot 9H_2O$, Sigma-Aldrich 99.99%, trace metal basis), copper (II) nitrate hemi(pentahydrate) ($CuN_2O_6 \cdot 2.5H_2O$, Aldrich 99.99% trace metal basis), and iron (III) nitrate nonahydrate ($FeN_3O_9 \cdot 9H_2O$, Sigma-Aldrich 99.99% trace metal basis). Niobium oxalate hexahydrate is insoluble in water. Therefore, it was firstly dissolved using 10% (w/v) oxalic acid solution^{104,105}. Other precursors were measured to be the desired percentages and were dissolved in 100 ml of distilled water.

Co-precipitation method was applied for catalyst preparation. In this method, an ammonium hydroxide solution (30%, m/v) was slowly added, at

room temperature, into a Zr-Fe, Ce-Fe, Cr-Fe and Nb-Fe solutions, which were previously dissolved in water together. The previous clear solution started to precipitate as the ammonium hydroxide solution was added. After waiting 24h to let the solution precipitate totally, the precipitate was filtered and was put into the oven. It was dried at 80 °C for 12h then the samples were calcined in static air at 400 °C for 4h. In order to see the effect of copper, incipient wetness impregnation method was applied. Previously prepared catalysts were impregnated with copper precursor using the incipient wetness impregnation technique (3wt% CuO). After 24 h of aging, the catalysts were dried (80 °C, 12h) and calcined in static air (400 °C, 4h).

Aluminum doped catalysts mainly prepared by the co-precipitation of aluminum, copper and iron precursors at the same time. After 24 h of aging, the catalysts were dried (80 °C, 12h) and calcined in static air (400 °C, 4h).

The calcined catalysts were ground to make powder catalysts. Naming of the catalysts were done according to the weight percentage and the symbol of the dopant elements. Slash in the abbreviation shows that the element at the left of the slash was impregnated. Table 2.1 gives the abbreviations of the catalysts, which will be shown through the text.

2.2.2. Catalyst Characterization

X-Ray Diffraction (XRD), *In situ* Raman Spectroscopy, Flow BET Surface Area and *in situ* High Sensitivity Low Energy Ion Scattering (HS-LEIS) were used to characterize the prepared catalyst in order to understand the bulk structure at room temperature and pressure (XRD), the present structure under oxidation and RWGS reaction conditions (Raman spectroscopy), surface area of fresh and spent catalysts (Flow BET) and the surface structure of fresh calcined and activated catalyst (*in situ* HS-LEIS).

Table 2.1 Abbreviations of the catalysts

Abbreviation	Meant	Abbreviation	Meant
Fe	100% iron oxide	3Cu/8ZrFe	3wt% CuO impregnated on 8wt% ZrO ₂ -Fe ₂ O ₃
8ZrFe	8wt% ZrO ₂ -Fe ₂ O ₃	3Cu/8NbFe	3wt% CuO impregnated on 8wt% Nb ₂ O ₅ -Fe ₂ O ₃
8NbFe	8wt% Nb ₂ O ₅ -Fe ₂ O ₃	3Cu/8CeFe	3wt% CuO impregnated on 8wt% CeO ₂ -Fe ₂ O ₃
8CeFe	8wt% CeO ₂ -Fe ₂ O ₃	3Cu8AlFe	3wt% CuO-8wt% Al ₂ O ₃ -Fe ₂ O ₃
8CrFe	8wt% Cr ₂ O ₃ -Fe ₂ O ₃	3Cu/8CrFe	3wt% CuO impregnated on 8wt% Cr ₂ O ₃ -Fe ₂ O ₃

2.2.2.1. X-Ray Diffraction (XRD)

Powder X-ray diffraction patterns of fresh calcined catalysts were measured by Panalytical Empyrean Xray Diffraction Unit. Cu attenuator mask was utilized for alignment. Full scans of 20-80 degrees (2 θ) were performed with a scan rate of 5 deg/min. The Fe₂O₃ (110) peak at 34.5-36.5 degrees was scanned with a rate of 1 deg/min to examine the possible formation of solid solutions of promoters and iron oxide.

2.2.2.2. *In situ* Raman Spectroscopy

The Raman studies were performed with a Horiba-Jobin Yvon LabRam High Resolution instrument equipped with a confocal microscope (50X long

working distance objective, Olympus BX-30-LWD), a laser excitation at 442 nm (generated by a He-Cd laser, 110 mW), and single stage monochromator with 900 grooves/mm grating. D1 filter was used to minimize any laser-induced alterations of the sample. The scattered light from the sample was passed through the monochromator grating and collected with a visible sensitive LN2-cooled CCD detector (Horiba-Jobin Yvon CCD-3000V). The Raman spectra of the all catalysts were collected firstly under ambient conditions then under dehydrated and reverse water-gas shift (RWGS) reaction conditions using the *in situ* Harrick cell. The catalysts were maintained as loose powder in Harrick cell and firstly dehydrated at 400 °C for 30 minutes under flowing 10% O₂/Ar (Praxair) with 30 mL/min flow rate to remove any possible adsorbed organic impurities and adsorbed moisture. Then the Raman spectra were collected. For spectra of the activated catalyst during the RWGS reaction, the catalyst were first dehydrated with 10% O₂/Ar (PRAXAIR) at 400 °C for 1h followed by switching to the RWGS reaction conditions (30 mL/min 5% CO₂/Ar (GTS-WELCO) and 15 mL/min 10% H₂/Ar (Airgas)).

2.2.2.3. High Sensitivity Low-Energy Ion Scattering (HS-LEIS)

The HS-LEIS experiments of the catalysts were performed in an ION-TOF Qtac¹⁰⁰ instrument. The copper impregnated powder catalyst samples were prepared for analysis by compressing the powder into appropriate sample holders for heat treatments within the HS-LEIS spectrometer. The protocol was for each sample to be held within ~ 100 mbar O₂ (g) at 400°C for 60 min and then depth profiled using 3 keV He⁺ and 5 keV Ne⁺ ion probes. Each sample was then held at ~ 100 mbar in a mixture of CO₂/H₂~1 again at 400°C for 60 min and then depth profiled again using 3 keV He⁺ and 5 keV Ne⁺ ion probes. Charge neutralization was invoked during spectra acquisition and sputtering. Used probes are 3 keV He⁺ (2 x 10¹⁴ cm⁻² cyc⁻¹) and 5 keV Ne⁺ (1 x 10¹⁴ cm⁻² cyc⁻¹), 1.0 x 1.0 mm². For sputtering, 0.5 keV Ar⁺ (3 x 10¹⁴ cm⁻² cyc⁻¹, 1.5 x 1.5 mm²)

was applied. The data for each were accumulated from ~ 20 individual spectra and normalized by the BET surface area.

2.2.2.4. Flow BET Surface Area

The BET surface areas of both fresh and spent catalysts were measured by a 3-point flow BET method with an Altamira Instruments system (AMI 200) equipped with a TCD detector. The N₂ adsorption/desorption amount were measured at three different partial pressures ($P/P_0=0.14, 0.22$ and 0.30) for the calculation of surface areas. The activated catalysts after WGS reaction were directly measured without exposing the pyrophoric catalysts to air.

2.2.3. CO-TPR

The CO-TPR experiments were performed on an Altamira AMI-200 spectroscope equipped with a Dycor Dymaxion DME200MS online quadrupole mass spectrometer. Approximately 30 mg of the catalyst was loaded into a U-type quartz tube for analysis, and the catalyst was held in place by quartz wool. To perform CO-TPR on the activated catalysts, samples were first dehydrated under 10% O₂/Ar at 350 °C for 1h followed by activation of the WGS reaction (10 mL/min 10% CO/Ar, 30 mL/min He flowing through bubbler at room temperature) at 350 °C for 90 min. After the reaction ended, the reactor was flushed by He and then cooled down to 85 °C. A flow of 30 mL/min 10% CO/Ar was then introduced, and the temperature was ramped up to 450 °C at a rate of 10 °C /min.

2.2.4. Steady-State Activity Measurement

Steady-state forward water gas shift reaction activity measurements were performed on an Altamira AMI-200 spectroscope equipped with a Dycor

Dymaxion DME200MS online quadrupole mass spectrometer. Approximately 10 mg of the catalyst was loaded into a U-type quartz tube for the reaction, and the catalyst was held in place by quartz wool. Firstly, 10% O₂/Ar (PRAXAIR) passed with the flow rate as 40 ml/min at 400 °C for 1hr to remove any possible adsorbed organics by combustion. Then the system was flushed with He for 10 min, after which the reaction mixture was introduced (10% CO/Ar (PRAXAIR, 10 mL/min), He (Airgas, UHP certified gas, 30 mL/min), and water vapor introduced by flowing the gas through a water bubbler at room temperature). After steady-state reaction occurred at 400 °C for an hour, temperature was decreased to 370 °C, 350 °C, and 330°C one by one and had been held there for an hour. For the calibration of the system with respect to CO₂, He (Airgas, UHP certified gas, 30 mL/min), 5%CO₂/Ar (GTS-WELCO, 10 mL/min), and water vapor were fed at 330 °C and had been held for an hour. The gases exiting the quartz tube reactor were analyzed with the online mass spectrometer. The following *m/e* ratios were employed for the identification of reaction gases and products: H₂, *m/e* =2; H₂O, *m/e* =18; CO, *m/e* =28; CO₂, *m/e* =44.

CHAPTER 3

COMPUTATIONAL METHOD

3.1. Computational Chemistry

Methods for ab initio calculations of materials properties and for simulations of processes in materials have been developed for the last two decades. Quantum-mechanical description of the interactions between electrons and between electrons and atomic nuclei develops the important impact on solid-state chemistry and on materials science. Density Functional Theory (DFT) is the important cornerstone which assigns the intractable complexity of the electron-electron interactions in many-electron systems into an effective one-electron potential, which is a functional of the electron density only. DFT method is applicable for structure and phase stability, mechanical and dynamic properties, magnetism and magnetic nanostructures, semiconductors and insulators, surfaces, chemical reactions and catalysis.¹⁰⁶ The Nobel Prize in Chemistry 1998 was divided equally between Walter Kohn “for his development of the density-functional theory” and John A. Pople “for his development of computational methods in quantum chemistry”.

3.1.1. Density Functional Theory

In quantum chemistry, molecules are expressed in terms of interactions among nuclei and electrons, and molecular geometry in terms of minimum energy arrangements of nuclei¹⁰⁷. Schrödinger equation was formulated to describe how the quantum state of a physical system changes in time. The time-independent, nonrelativistic Schrödinger equation¹⁰⁸:

$$\hat{H}\Psi(\vec{x}_1, \vec{x}_2, \dots, \vec{x}_N, \vec{R}_1, \vec{R}_2, \dots, \vec{R}_M) = E_i\Psi(\vec{x}_1, \vec{x}_2, \dots, \vec{x}_N, \vec{R}_1, \vec{R}_2, \dots, \vec{R}_M) \quad (3.1)$$

where \hat{H} is the Hamilton operator for a molecular system consisting of M nuclei and N electrons without magnetic or electric fields. \hat{H} is a differential operator which represents the total energy:

$$\hat{H} = -\frac{1}{2} \sum_{i=1}^N \nabla_i^2 - \frac{1}{2} \sum_{A=1}^M \frac{1}{M_A} \nabla_A^2 - \sum_{i=1}^N \sum_{A=1}^M \frac{Z_A}{r_{iA}} + \sum_{i=1}^N \sum_{j>i}^N \frac{1}{r_{ij}} + \sum_{A=1}^M \sum_{B>A}^M \frac{Z_A Z_B}{R_{AB}} \quad (3.2)$$

A and B, and i and j denote the M nuclei and the N electrons in the system, respectively. The first two terms describe the kinetic energy of electrons and nuclei respectively. The remaining three terms represent the attractive electrostatic interaction between the nuclei and the electrons and the repulsive potential due to the electron-electron and nucleus-nucleus interactions, respectively. Ψ_i stands for the wave function of the i'th state of the system which contains all information that can possibly be known about the quantum system. And, E_i is the numerical value of the energy of the state.

The differences between the masses of nuclei and electrons may simplify the Schrödinger equation. The nuclei move much slower than the electrons since the lightest of all nuclei (the proton, ^1H) weighs 1800 times more than an electron. The consideration of the electrons as moving in the field of fixed nuclei is known as *Born-Oppenheimer* approximation. The complete Hamiltonian reduces to the electronic Hamiltonian where the kinetic energy of the nuclei is zero by fixed in space and the potential energy due to nucleus-nucleus repulsion is a constant:

$$\hat{H}_{elec} = -\frac{1}{2} \sum_{i=1}^N \nabla_i^2 - \sum_{i=1}^N \sum_{A=1}^M \frac{Z_A}{r_{iA}} + \sum_{i=1}^N \sum_{j>i}^N \frac{1}{r_{ij}} = \hat{T} + \hat{V}_{Ne} + \hat{V}_{ee} \quad (3.3)$$

where \hat{T} represents the kinetic energy of the electrons, \hat{V}_{Ne} represents electron-nucleus attraction, and \hat{V}_{ee} represents the repulsive electron-electron interactions which depends on the coordinates of two electrons at the same time.

Equation 3.3 can be soluble for a single atom, i.e. hydrogen atom. Wave-function methods provide the required chemical accuracy for sufficiently small molecules¹⁰⁹. It is clear that the solution of this equation for a molecular system is quite complicated and needs sophisticated methods. Hartree-Fock approximation is a typical example, which is used to know wave-function. If wave function Ψ is known, all information can be known about the particular state of the target system; however, the wave function is very complicated quantity and cannot be probed experimentally and depends on three spatial and one spin variable for each of the N electrons. Wave function treatment to understand the systems with many atoms and many electrons makes a computational treatment very difficult. Instead of wave-function, electron density $\rho(\vec{r})$ which depends only on the three spatial variables can be used to solve the Schrödinger equation¹⁰⁸. It determines the probability of finding any of the N electrons within volume element $d\vec{r}$. To solve Schrödinger equation, Hamilton operator, \hat{H} , should also be defined by the number of electrons (N), the position of the nuclei in space (R_A), and the charges of nuclei (Z_A). Electron density $\rho(\vec{r})$ provides these informations by:

- (i) the density integrates to the number of electrons: $\int \rho(\vec{r}_1) d\vec{r}_1 = N$
- (ii) $\rho(\vec{r})$ has maxima only at the positions R_A of the nuclei
- (iii) the density at the positions of the nucleus contains information about the nuclear charge Z: $\lim_{r_{1A} \rightarrow 0} \left[\frac{\partial}{\partial r} + 2Z_A \right] \bar{\rho}(\vec{r}) = 0$

Density functional theory focuses on quantities in the real, three dimensional coordinate spaces, principally on the electron density $\rho(\vec{r})$. The first application of the electron density rather than the wave function was dated to the

work of Thomas and Fermi, 1927. In Thomas-Fermi (TF) model, the energy of an atom can be expressed as:

$$E_{TF}[\rho(\vec{r})] = \frac{3}{10} (3\pi^2)^{2/3} \int \rho^{5/3}(\vec{r}) d\vec{r} - Z \int \frac{\rho(\vec{r})}{r} d\vec{r} + \frac{1}{2} \iint \frac{\rho(\vec{r}_1)\rho(\vec{r}_2)}{r_{12}} d\vec{r}_1 d\vec{r}_2 \quad (3.4)$$

where first term is the TF expression for the kinetic energy based on the uniform electron gas, second and the third terms are the classical expressions for the nuclear-electron attractive potential and the electron-electron repulsive potential, respectively. This expression is important for the relation between the energy and the electron density, but it does not consider the exchange and correlation effects¹⁰⁸. After application of exchange energy by Dirac, new model appeared as Thomas-Fermi-Dirac model which includes the kinetic and classical Coulomb contributions as well as the quantum mechanical exchange effects.

The basis of the modern day density functional theories is the theorems of Hohenberg and Kohn published in 1964¹¹⁰. They proved two theorems¹¹¹:

1. First theorem states that the electron density uniquely determines the external potential and thus the Hamiltonian operator. Electron density uniquely determines the positions and charges of the nuclei and thus determines the Hamiltonian and all the properties of the system. This theorem demonstrates the existence of a one-to-one mapping between the ground state electron density and the ground state wave-function of a many particle system. It is possible to say that energy is a functional of the density.

2. Second theorem states that the ground state energy (E_0) can be obtained by variational method. The density that minimizes the total energy is the exact ground state density for every trial electron density ($\tilde{\rho}$).

$$E_o \leq E[\tilde{\rho}] = T[\tilde{\rho}] + E_{Ne}[\tilde{\rho}] + E_{ee}[\tilde{\rho}] \quad (3.5)$$

In 1965, Kohn and Sham obtained set of self-consistent equations by using the formalism of Hohenberg and Kohn¹¹². In these equations, they included exchange and correlation effects to approximate the kinetic and electron-electron functionals. Kohn-Sham (KS) equations have the same structure as the Hartree-Fock (HF) equations, the non-local exchange potentials used in HF equations are replaced by the local exchange-correlation potential.¹¹¹ They set up a fictitious system of N non-interacting electrons with a Hamiltonian with an effective local potential. As seen from equation (3.6), Hamilton operator describes a non-interacting system since it does not contain any electron-electron interactions.

$$\hat{H}_S = -\frac{1}{2} \sum_{i=1}^N \nabla_i^2 - \sum_{i=1}^N V_S(\vec{r}_i) \quad (3.6)$$

The total energy of the interacting system in terms of the separation can be expressed as:

$$E[\rho] = T_s[\rho] + J[\rho] + E_{Ne}[\rho] + E_{XC}[\rho] \quad (3.7)$$

Where $E_{XC}[\rho]$ is the exchange-correlation energy and the sum of the error made in using a non-interacting kinetic energy and the error made in treating the electron-electron interaction classically and defined as:

$$E_{XC}[\rho] \equiv (T[\rho] - T_s[\rho]) + (E_{ee}[\rho] - J[\rho]) \quad (3.8)$$

Kinetic energy term:

$$T_s[\rho] = -\frac{1}{2} \sum_i^N \langle \varphi_i | \nabla^2 | \varphi_i \rangle \quad (3.9)$$

Classical electron-electron repulsion term:

$$J[\rho] = \frac{1}{2} \iint \frac{\rho(\vec{r}_1)\rho(\vec{r}_2)}{r_{12}} d\vec{r}_1 d\vec{r}_2 = \frac{1}{2} \sum_i^N \sum_j^N \iint |\varphi_i(\vec{r}_1)|^2 \frac{1}{r_{12}} |\varphi_j(\vec{r}_2)|^2 d\vec{r}_1 d\vec{r}_2 \quad (3.10)$$

Nucleus-electron interaction portion of potential energy:

$$E_{Ne}[\rho] = \int V_{Ne}\rho(\vec{r})d\vec{r} = - \sum_i^N \int \sum_A^M \frac{Z_A}{r_{1A}} |\varphi_i(\vec{r}_1)|^2 d\vec{r}_1 \quad (3.11)$$

In these equations, the φ_i are the orbitals of the non-interacting system.

The final form of Kohn-Sham equations:

$$\left(-\frac{1}{2}\nabla^2 + \left[\int \frac{\rho(\vec{r}_2)}{r_{12}} d\vec{r}_2 + V_{XC}(\vec{r}_1) - \sum_A^M \frac{Z_A}{r_{1A}} \right] \right) \varphi_i = \left(-\frac{1}{2}\nabla^2 + V_{eff}(\vec{r}_1) \right) \varphi_i = \varepsilon_i \varphi_i \quad (3.12)$$

$$\text{where} \quad V_s(\vec{r}) = V_{eff}(\vec{r}) = \int \frac{\rho(\vec{r}_2)}{r_{12}} d\vec{r}_2 + V_{XC}(\vec{r}_1) - \sum_A^M \frac{Z_A}{r_{1A}} \quad (3.13)$$

In the above equations, V_{XC} which is the potential due to the exchange-correlation energy E_{XC} and E_{XC} are unknown and approximations should be implemented to take exchange and correlation energy into account¹⁰⁸.

3.1.2. Approximations

3.1.2.1. Local Density Approximation (LDA) & Local Spin-Density Approximation

Local density approximation (LDA) is one of the most widely used and simplest approximations. This model is based on the idea of a hypothetical uniform electron gas. In this system, the electrons are subjected to a constant external potential and thus charge density is constant. Uniform electron gas is important for density functional theory since it is the only system for which the

form of the exchange and correlation energy functionals is known exactly. The exchange-correlation energy is given as:

$$E_{XC}^{LDA}[\rho] = \int \rho(\vec{r}) \varepsilon_{XC}(\rho(\vec{r})) d\vec{r} \quad (3.14)$$

where $\varepsilon_{XC}(\rho(\vec{r}))$ is the exchange energy of an electron in a uniform electron gas of a particular density and is a function of only the local value of the density.¹⁰⁸

LDA can be used for properties such as structure, vibrational frequencies, elastic moduli and phase stability for many systems. However, there will be overestimation of the binding energy of many systems and absence of energy barriers in chemical reactions¹¹¹.

A spin-polarized form of LDA is the local spin-density approximation. The exchange-correlation energy is given as:

$$E_{XC}^{LSDA}[\rho_\alpha, \rho_\beta] = \int \rho(\vec{r}) \varepsilon_{XC}(\rho_\alpha(\vec{r}), \rho_\beta(\vec{r})) d\vec{r} \quad (3.15)$$

where $\rho_\alpha(\vec{r}) \neq \rho_\beta(\vec{r})$, spin polarized case. For the simple, spin compensated situation $\rho_\alpha(\vec{r}) = \rho_\beta(\vec{r}) = 1/2 \rho(\vec{r})$.

3.1.2.2. The Generalized Gradient Approximation

Besides the LDA, the generalized gradient approximation (GGA) uses the information about the density $\rho(\vec{r})$ at a particular point \vec{r} and also the gradient of the charge density. The gradient of the charge density, $\nabla\rho(\vec{r})$ accounts the non-homogeneity of the true electron density.¹¹⁰ The exchange-correlation energy is given as:

$$E_{XC}^{GGA}[\rho] = \int \rho(\vec{r}) \varepsilon_{XC}(\rho(\vec{r}), \nabla\rho(\vec{r})) d\vec{r} \quad (3.16)$$

For open systems such as surfaces GGA should be used since there are strong variations of the electronic density over the surfaces. There are possible options to perform GGA calculation. Some of these are Perdew-Becke (PB), Perdew-Wang86 (PW), Perdew-Wang91 (PW91), and revised Perdew-Burke-Ernzerhof (RP).

3.1.2.3. LDA/GGA+U

The application of LDA or GGA to materials with ions that contain incomplete d shells such as transition-metal oxides fails since these approximations have the mean-field character of the Kohn-Sham equations and do not consider the strong Coulomb repulsion between electrons^{106,113}. LDA/GGA+U include the interactions between electrons localized on the same atomic center (on-site Coulomb interaction) in the LDA/GGA Hamiltonian, which makes the potential as spin and orbital dependent. Orbital-dependent potential reduces the fluctuations of the d occupancy¹¹³ which improves the description of the measured electron energy loss spectra, values of the lattice constant, and magnetic moments¹¹⁴. LDA/GGA+U (DFT+U) energy functional can be defined as following:

$$E_{DFT+U} = E_{DFT} + \frac{U-J}{2} \sum_{\sigma} Tr[\rho^{\sigma} - \rho^{\sigma} \rho^{\sigma}] \quad (3.17)$$

where U is the Hubbard parameter which is an adjustable parameter and measures the increase in the energy caused by placing an additional electron into a particular site, J is an exchange parameter and ρ^{σ} is the spin-dependent on-site density matrix.¹⁰⁶

3.1.3. The VASP Software

Vienna Ab-initio Simulation Package (VASP)¹¹⁵⁻¹¹⁷ was initially written by Mike Payne at the MIT, was brought to Vienna by Jürgen Hafner and was developed by Furtmüller and co-workers in the University of Vienna. VASP is the density functional theory algorithm for the self-consistent solution of the Kohn-Sham equations. Ultra-soft pseudopotentials or the projector-augmented wave (PAW) method is used to describe the interaction between the ions and electrons. Plane wave basis sets with periodic boundary conditions are used to express the electronic properties such as charge density and orbitals. Periodic surface is the infinite repetition of the unit cell which is the smallest crystal structure. Total energy, forces, and the geometry optimization can be evaluated by VASP package. POTCAR, POSCAR, KPOINTS, and INCAR are the required input files for the calculations.¹¹⁸

- POTCAR: This file contains the pseudopotentials for each atomic species and the information about the atoms (mass, valence...). This file also contains default energy cutoffs.
- POSCAR: This file contains the lattice geometry, the number of atoms and their atomic positions.
- KPOINTS: This file contains k-point coordinates and the mesh size for creating the k-point grid.
- INCAR: This file is the central input of VASP which contains large number of parameters to define the calculation.

More detailed information can be found from:

http://cms.mpi.univie.ac.at/vasp/vasp/vasp.html.4_

Identification of the lowest energy path for atoms from one stable configuration to another is mostly used to define reaction coordinates for transitions. This path is called as “minimum energy path” (MEP). From this path,

it is possible to estimate the activation energy barrier. The nudged elastic band (NEB) is a method to find saddle points and minimum energy paths between known reactants and products¹¹⁹. VASP supports the elastic band method to calculate energy barriers. According to the defined number of images between reactants and products, it is possible to see the change of the surfaces or components during the chemical reactions.

3.2. Computational Procedure

Magnetite (Fe_3O_4) is considered to be the active phase in the WGS reaction. Before the analysis of catalytic activity, the bulk phase structure was optimized. Afterwards, selected surfaces to be used in the catalytic activity analysis were cleaved from the bulk structure and geometry optimization studies were carried out. Firstly, most stable surface of (111) was studied with all different layers. Possible locations for the addition of chromium and copper atoms on the cleaved surfaces were studied respectively.

3.2.1. Clean Magnetite Bulk Calculations

Fe_3O_4 has a cubic Bravais lattice with 8 formula units, 32 oxygen anion sites and 24 cation sites, per unit cell. Magnetite has the inverse spinel structure where oxygen atoms form a close-packed face centered cubic (FCC) lattice, 8 Fe^{3+} ions fill tetrahedral sites, 8 Fe^{3+} reside in octahedral positions and remaining 8 Fe^{2+} ions fill again octahedral sites. Being the negatively charged layers of fcc close packed O^{2-} ions and positively charged Fe containing layers make both iron- and oxygen- terminated Fe_3O_4 (111) surfaces are polar type of III according to the Tasker's¹²⁰ classification. Space group is $Fd3m$ (no.227)¹²¹. The unit cell edge length is $a = 8.3941 \text{ \AA}$. The coordinates of tetrahedrally and octahedrally positioned Fe atoms are $(1/8, 1/8, 1/8)$ and $(1/2, 1/2, 1/2)$, respectively. O atoms occupy the position 32(e) with (u, u, u) and u is found in the study of Fleet as

0.2549. Table 3.1 gives the observed and calculated bond distances and u parameters for normal and inverse structure.

Table 3.1. Observed and calculated bond distances and u parameter ¹²²

Bond distances (Å)	observed	calculated
Tetrahedral: Fe ²⁺ -O	2.03	
Fe ³⁺ -O	1.89	1.888
Octahedral: (Fe ²⁺ , Fe ³⁺)-O	2.113	
Fe ³⁺ -O	2.045	2.0584
Parameter u		
Normal structure	0.2618	
Inverse structure	0.2527	0.2549

3.2.2. Computational Details

Vienna Ab-initio Simulation Package (VASP) was used for periodic DFT calculations applying the projector augmented-wave (PAW) method^{76,122,123}. Both local density approximation (LDA) and generalized gradient approximation (GGA) were used to take exchange and correlation energy into account. Moreover, Hubbard parameter, U , and exchange parameter, J , were also considered in LDA/GGA+ U method in order to include the interactions between electrons localized on the same atomic center (on-site Coulomb interaction)^{124–126}. The Hubbard parameter measures the increase in the energy caused by placing an additional electron into a particular site and describes the on-site Coulomb interaction of iron and chromium 3d electrons. This should be considered for transition-metal oxides¹²⁴. These U and J values should be taken by trials to represent the system well.

Spin polarized calculation of Fe₃O₄ bulk structure were continued without spin polarization for the surface structures in Chapter 4. For the bulk

structure optimization, J was kept constant as 0.89eV, whereas different U values were tested in range of 0-7eV in order to get correct lattice parameter for LDA+U calculations. (19 x 19 x 19) Monkhorst-Pack mesh k-point grids were used for bulk structure's relaxation.

Chapter 5 gives the results of spin-polarized periodic DFT calculations of ferromagnetic Fe₃O₄ structure. Here J and U were taken as 1 and 5 eV, respectively. (11 x 11 x 11) Monkhorst-Pack mesh k-point grids were used for bulk structure's relaxation.

The valence electron configurations 4s¹3d⁷, 4s¹3d⁵, 2s²2p⁴, 2s²2p², 1s¹ were used to describe Fe, Cr, O, C and H atoms in all calculations. (4 x 4 x 1) grid is used for the surface optimization and reaction step calculations¹²⁷. The cutoff energy for the plane wave basis was fixed at 520 eV. After obtaining the optimized Fe₃O₄ structure, (111) surfaces, the most stable surface, were cleaved with all possible different ending layers. 15 Å of vacuum space were added on the top of the surface to avoid interactions. All layers were kept relaxed except the bottom layer for during surface optimization. Bulk optimization was carried out with totally relaxed structure.

3.2.2.1. Energy Analysis

The stability of the surface terminations were considered by computing the surface energy according to the following equation¹²⁸

$$E_{surf} = \frac{(E_{slab} - N \cdot E_{bulk})}{2 \cdot A_{slab}} \quad (3.18)$$

Where, E_{surf} is the energy for the surface formation; E_{slab} is the total energy for the slab; E_{bulk} is the energy of the optimized bulk structure per

molecule unit; N is the number of the molecule units in the slab and A is the surface area of the slab.

In the models with Cr doping, Cr atoms were substituted at the some convenient positions on the surface. Different initial guess of magnetic moment and spin direction for Cr atoms were carried out for spin-polarized DFT calculations. The structure with the lowest surface energy were considered as the possible Cr-doped surface.

The substitution of any atom on the surface changes the energy of the system. Energy change due to atom substitution on the surface can be calculated as following:

$$\Delta E_{substitution} = (E_{atom-surface} + NE_{Fe}) - (E_{surface} + NE_{atom}) \quad (3.19)$$

Where; $\Delta E_{substitution}$ is the energy change of the surface due to the atom substitution; $E_{atom-surface}$ and $E_{surface}$ are the energy of the present surface; E_{Fe} and E_{atom} is the energy of the presence of an one iron atom and a substitution atom, respectively, in a similar supercell under vacuum. Lastly, N is the number of atom, which is substituted.

After construction of the surfaces, oxygen vacancy formation and adsorption and desorption of the reactants (CO and H₂O) were studied. Oxygen formation energy can be calculated as following:

$$E_{vac} = E_{oxygen\ vacant\ surface} + 0.5E_{oxygen\ molecule} - E_{surface} \quad (3.20)$$

Where, E_{vac} is the required energy for the vacancy formation; $E_{oxygen\ vacant\ surface}$ is the energy of the optimized oxygen vacant surface;

$E_{oxygen\ molecule}$ is the energy of the gas phase oxygen molecule; and $E_{surface}$ is the energy of the optimized structure of the surface.

Adsorption energies can be calculated as following:

$$E_{adsorption} = E_{adsorbate\ on\ the\ surface} - (E_{adsorbate} + E_{surface}) \quad (3.21)$$

Where, $E_{adsorption}$ is the adsorption energy of the considered adsorbate; $E_{adsorbate\ on\ the\ surface}$ is the energy of the optimized surface and adsorbate on this; $E_{adsorbate}$ is the energy of the gas phase adsorbate; and $E_{surface}$ is the energy of the optimized structure of the surface.

CHAPTER 4

Cr₂O₃-Fe₂O₃ CATALYSTS OXYGEN TERMINATED Fe₃O₄ (111) SURFACE

4.1. Abstract

As part of high temperature water gas shift reaction mechanism, CO and H₂O adsorption on Fe₃O₄ (111) and chromium atom substituted Fe₃O₄ (111) slab surfaces are investigated by means of periodic DFT approach using VASP. Fe₃O₄ bulk structure has been computed by LDA+U (Local Density Approximation with on-site Coulomb interaction). One oxygen site (O_{oct1}) is studied as a probable site among the six Fe₃O₄ (111) terminations. Cr atom substitution on this surface is also examined. Cr atoms prefer being on the surface rather than in the bulk structure and Cr atoms substitute on the octahedral iron atom layer (O_{oct2}Cr). Adsorption energies of CO on O_{oct1} and O_{oct2}Cr are found as -96 kcal/mol and -47 kcal/mol. Water adsorption on O_{oct1} surface is molecular with -54.88 kcal/mol adsorption energy. On the other hand, water adsorption on O_{oct2}Cr surface is dissociative with nearly same adsorption energy, -55.12 kcal/mol, indicating the catalytic effect of chromium atom.

4.2. Results and Discussion

4.2.1. Bulk Optimization

The Fe₃O₄ iron oxide phase has a cubic, inverse spinel structure with the space group of *Fd3m*. The Fe cation is the transition metal with the electron configuration of [Ar]3d⁶4s². The incomplete *d* shells in transition-metal oxides make the application of LDA fail since it does not consider the strong Coulomb repulsion between electrons^{106,113}. Therefore, Hubbard and exchange parameters

were applied in order to consider on-site Coulomb interaction. The experimentally measured lattice parameter is 8.3941 Å¹²². The optimized bulk lattice parameters are tabulated in Table 4.1.

Table 4.1 Optimized bulk lattice parameter for different methods

Method	LDA	LDAU U=4.5 eV J=0.89 eV	LDAU U=5 eV J=0.89 eV	LDAU U=7 eV J=0.89 eV	LDAU U=8 eV J=0.89 eV
Optimized Value, Å					
Fe₃O₄	7.8454	8.0154	8.3355	8.3133	8.2952

After application of the Hubbard and the exchange parameters, the results improved. For the calculations, the J parameter was kept constant and the U value was varied. An increase in the U value increases the lattice parameter up to a point. From the LDA+U calculation, the Fe₃O₄ structure can be defined with the lattice parameter of 8.3355 Å, which is the closest value to the experimental one (8.3941 Å¹²²) when U is 5 eV and J is 0.89 eV⁸⁰. In addition, the bond distances of Fe_{tet}-O and Fe_{oct}-O are found to be 1.8932 and 2.0340 Å, respectively. These are in good agreement with the experimental values of 1.888 and 2.0584 Å respectively¹²². The optimized structure of Fe₃O₄ is given in Figure 4.1. The magnetic moments of both tetrahedral and octahedral sites exhibit nearly 4 μ_B, corresponding to an average magnetic moment of 4.066μ_B that is very close to the experimental value of 4.05μ_B¹²⁹.

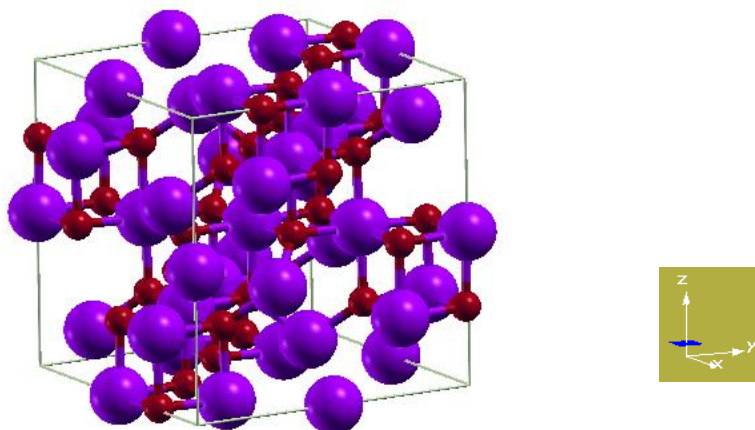


Figure 4.1. Bulk structure of Fe_3O_4 with LDA+U (Fe: purple, O: red)

4.2.2. Surface Optimization

Close packed planes tend to grow more slowly and these slow growing faces dominate the morphology. In magnetite, the oxygen ions are regularly cubic close packed along the $[111]^{121}$ and the (111) surface is found as the most stable surface among all surfaces on the basis of the computed surface energy in the study of Yu et al.⁷⁶. Six different terminations of (111) surface of Fe_3O_4 were cleaved. All the layers except the bottom layer were allowed to relax and the only the bottom layer was kept fixed for the prepared (2x1x1) supercells. A 15 Å of vacuum space was applied to avoid interactions. All terminations have the same a, b, β values of 11.7882 Å, 5.8941 Å, and 120°, respectively. The six optimized terminations of (111) surface are shown in Figure 4.2.

There are 3 different terminations: octahedral and tetrahedral coordinated iron and oxygen layers with 2 different permutations. The Fe_{Oct1} termination reveals three Fe atoms located at octahedral sites over a four oxygen atom layer. The Fe_{Oct2} termination reveals two Fe atoms located at octahedral sites over the four oxygen atom layer. The Fe_{Tet1} termination reveals one Fe atom located at the tetrahedral site over the four oxygen atom layer. The Fe_{Tet2} termination reveals three Fe atoms located at three different sites on three layers: the top and bottom

layers are tetrahedral sites and the middle one is octahedral site with a closely packed oxygen layer underneath. The O_{oct1} termination reveals four O atoms over a layer of three Fe atoms located at octahedral sites. The O_{oct2} termination exposes four oxygen atoms over three different Fe atom layers. In the O_{oct1} termination, the top iron layer is located at an octahedral site. The bottom following three iron layers are located at tetrahedral, octahedral and tetrahedral sites, respectively. The (111) surface with oxygen termination (O_{oct1}) was investigated in this study for the reaction mechanism of WGS reaction with the a, b, c, β lattice parameter values of 11.7882 Å, 5.8941 Å, 22.1716 Å, and 120°, respectively.

4.2.3. O_{oct1} Termination of Fe_3O_4 (111)

4.2.3.1. Chromium Atomic Substitution on O_{oct1} Termination of Fe_3O_4 (111)

Chromium substituted surfaces were prepared replacing a Fe atom with a Cr atom at different sites and at different surface coverage. Chromium can make substitutional solid solution having complete solubility with the iron atoms since Fe and Cr atoms both have BCC structure with very close atomic radius (0.124 and 0.125nm, respectively) and electronegativity (1.8 and 1.6, respectively)¹²³. The energy change due to chromium substitution on the surface was calculated with Eq. (3.19) and the values are tabulated in Table 4.2. The initial structure for the chromium located surfaces with different numbers of Cr atom is also illustrated in Figure 4.3.

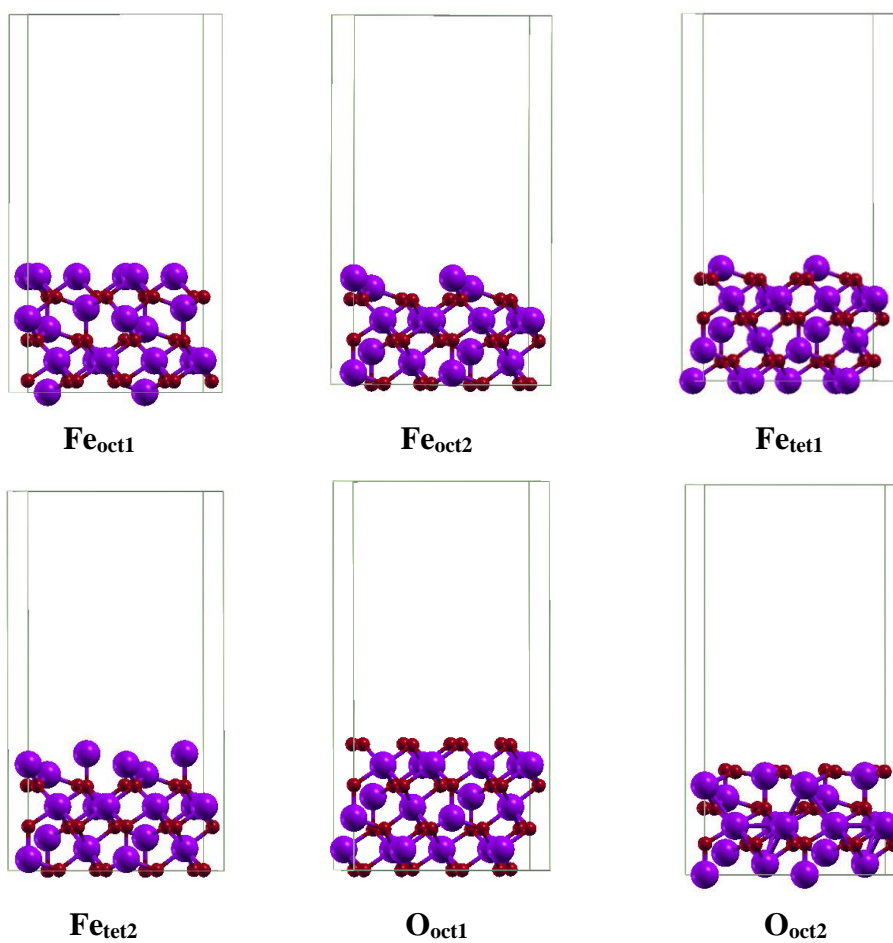


Figure 4.2. Six terminations of Fe₃O₄ (111) surface (Fe: purple, O: red)

Table 4.2. Energy change values due to Cr atom substitution on O_{oct1} surface

Surface	Energy Change (eV)
Ooct1Cr	-4.0
Ooct2Cr	-6.8
Ooct3Cr	-7.5
Ooct2Cr-a	-6.2
Ooct2Cr-aa	-7.1
Ooct2Cr-aal	-4.1

The surfaces of Ooct1Cr, Ooct2Cr, and Ooct3Cr were examined in order to see the effect of number of Cr atom on the surfaces. For the surfaces of Ooct1Cr, Ooct2Cr, and Ooct3Cr there are one, two and three Cr atoms located on octahedral position. Increasing the number of chromium atoms makes the energy changes smaller as indicated in Table 4.2. This means that increasing the percentage of chromium in the system, chromium terminating surfaces are more stable than other surfaces. The supported 9% Cr₂O₃ in the Cr₂O₃/Fe₂O₃ catalyst series reported in the experimental section⁵ corresponds to approximately two Cr atoms in the optimized Ooct1 surface structure of this study. Substitution of a Cr atom on the surface is energetically preferred to Cr atom substitution in the bulk unit cell in line with experimental studies^{21,25}.

The location of the Cr atoms also affects the stability of the surface. Therefore 4 different structures were optimized with 2 Cr atoms in the system of the oxygen terminated (111) surface of Fe₃O₄. Besides Ooct2Cr, there are also Ooct2Cr-a, Ooct2Cr-aa, and Ooct2Cr-aal. In Ooct2Cr-a, there are two substituted atoms: one is located at the top octahedral site and the other is at the first tetrahedral site. In Ooct2Cr-aa, both Cr atoms are located at the first tetrahedral site. In the last configuration, the chromium atoms are substituted with the iron atoms located under the second layer of oxygen: one atom is at the first tetrahedral site and the other is at second octahedral site. The initial and optimized structures are given in Figure 4.4. As reported in Table 4.2, the energy change is highest for the Ooct2Cr-aa surface and the lowest one belongs to the surface Ooct2Cr-aal. Although, Ooct2Cr-aa has the lowest energy, the structure reconstructed in this case and the chromium atoms tend to stay at the top layer. Therefore, the Ooct2Cr was taken as the most stable surface for chromium substitution.

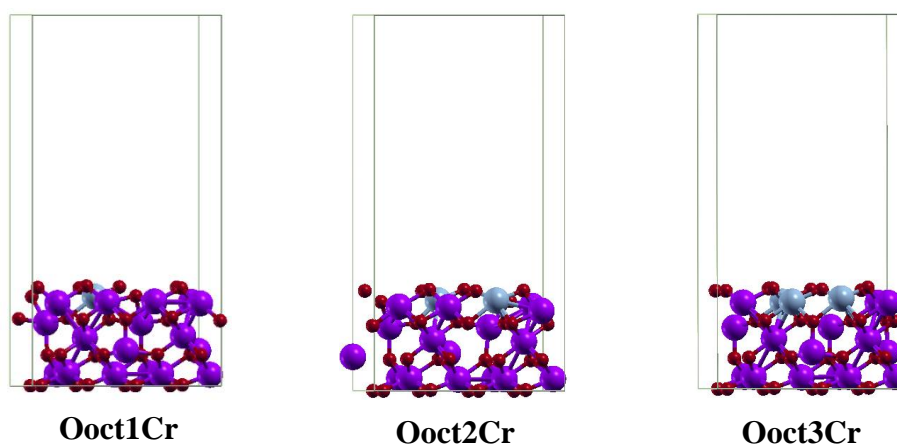


Figure 4.3. Possible chromium substitution with iron atoms on $O_{\text{oct}1}$ termination of Fe_3O_4 (111) surface (Fe: purple, O: red, Cr: gray)

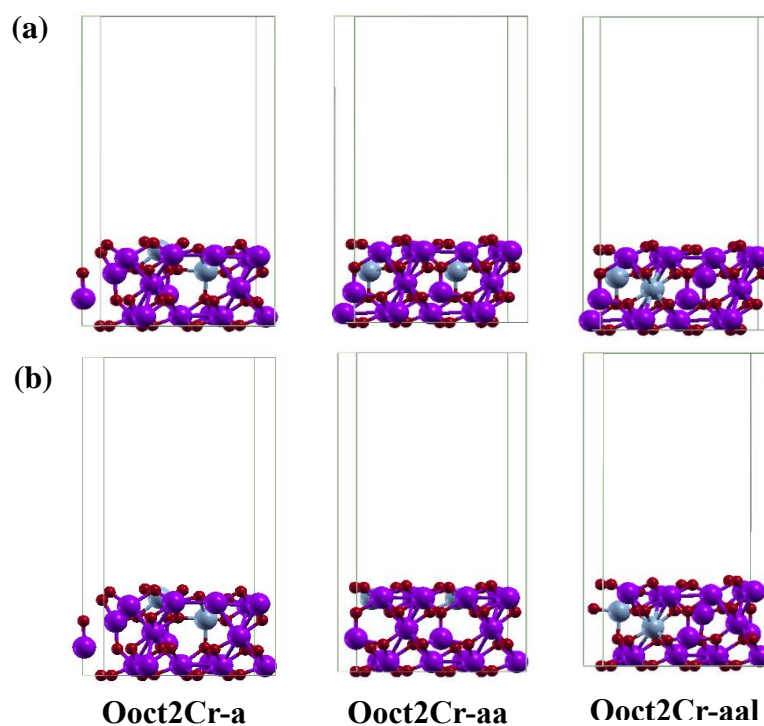


Figure 4.4. (a) Initial (b) Optimized structures of possible location of 2 chromium atoms on $O_{\text{oct}1}$ termination of Fe_3O_4 (111) surface (Fe: purple, O: red, Cr: gray)

For the Ooct2Cr surface, the average Cr-O distance is 1.89 Å and the average distance Fe-O distance is 1.95 Å. This difference is in good agreement with the literature. Gaudry et al. (2003) found the Cr-O and Fe-O mean distances to be 1.97 and 2.01 Å, respectively in the study of substitutional Cr³⁺ and Fe³⁺ ions in corundum structure by EXAFS analysis¹³⁰. The theoretical investigation of α -Fe₂O₃-Cr₂O₃ by Benny et al. (2009)¹³¹ found that in spite of the similar geometries, the difference in the interlayer distance is smaller for the Cr₂O₃ phase than for the Fe₂O₃ phase. From this point onwards, thus, the reaction step computations for the water gas shift reaction will be performed on the Ooct2Cr surface.

4.2.3.2. Regenerative Mechanism on the Surfaces

The water-gas shift reaction can be represented by the regenerative (redox) mechanism¹. The catalyst surface is reduced by CO to form CO₂. The surface is then subsequently oxidized by H₂O to H₂. After this series reaction steps, the catalyst surface returns to its original, fully oxidized pre-reaction state.

The regenerative mechanism can be divided into four reaction steps:

1. adsorption of CO on the surface,
2. desorption of CO₂ from the surface by taking one O atom from the lattice of catalyst,
3. adsorption of H₂O on this O vacancy site, and
4. desorption of H₂ after leaving one oxygen on the vacancy.

4.2.3.2.1. Regenerative Mechanism on O_{oct1} Terminated Surface

The optimized geometries belong to each reaction steps and energy profiles of these steps on O_{oct1} termination are illustrated in Figure 4.5. The

relative energies of redox mechanism steps on O_{Oct1} termination are tabulated in Table 4.3.

The bond length of CO molecule is 1.135 Å and the adsorption energy of CO is evaluated from the total energy calculations, Eq. (3.21), as -95.9 kcal/mol. When CO adsorbs on surface O atom (O_{lattice}), it forms a bond with length of 1.19 Å and the length between C and O of carbon is 1.15 Å. Desorption of produced CO_2 from the surface needs an energy of 20.8 kcal/mol. The C-O bond length in the CO_2 molecule is 1.168 Å. Desorption of CO_2 creates an O vacancy ($[]_{\text{Ovac}}$) on the surface. When water molecules are present in the vapor state, H_2O adsorbs on this vacancy site. The molecular adsorption energy of water on the O_{Oct1} surface is evaluated as -54.9 kcal/mol. The O-H bond length of the water molecule in the vapor phase is 0.9724 Å. When molecular H_2O adsorbs on the vacancy, the distance between Fe and O atom of water is 2.041 Å. One O-H distance is 1.072 and the other O-H distance is 0.981 Å. The energy between the vapor phase water molecule and H_2 is 82.1 kcal/mol and the bond length of gaseous H_2 is 0.768 Å.

Table 4.3 Regenerative mechanism steps of water gas shift reaction on O_{Oct1} surface

Reaction Step	Relative Energy, eV (kcal/mol)
$CO_{(g)} + O_{\text{lattice}} \rightarrow CO_{2(\text{ads})}$	-4.2 (-95.9)
$CO_{2(\text{ads})} \rightarrow CO_{2(g)} + []_{\text{Ovac}}$	0.9 (20.8)
$[]_{\text{Ovac}} + H_2O_{(g)} \rightarrow H_2O_{(\text{ads})}$	-2.4 (-54.9)
$H_2O_{(\text{ads})} \rightarrow H_{2(g)} + O_{\text{lattice}}$	3.6 (82.1)

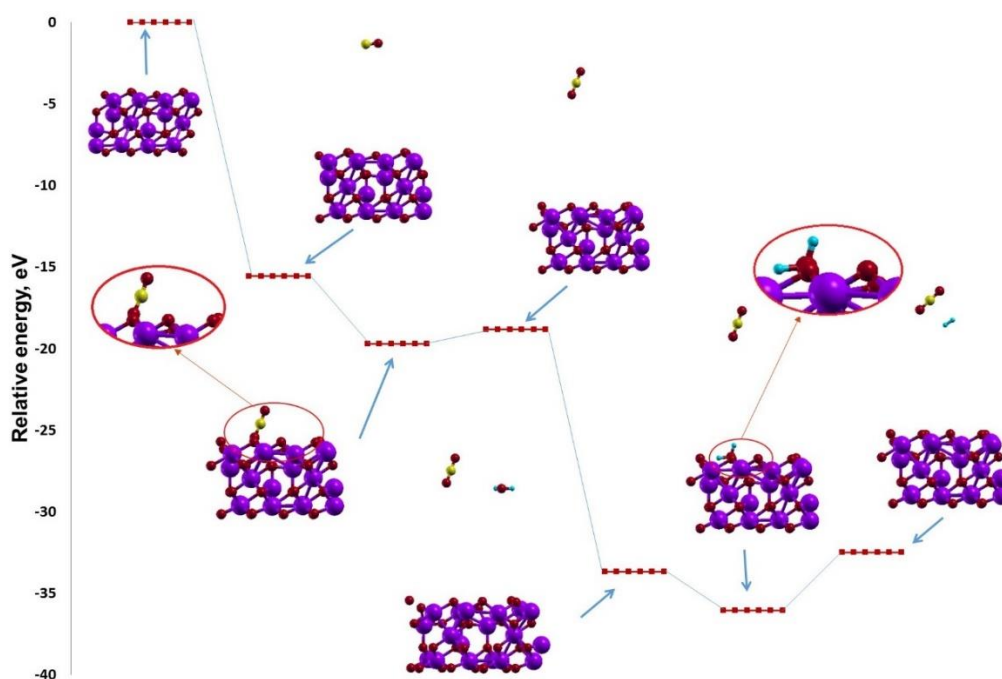


Figure 4.5. Energy profiles & optimized configurations of reaction steps on O_{oct1} surface (Fe: purple, O: red, C: yellow, H: blue)

4.2.3.2.2. Regenerative Mechanism on O_{oct2Cr} Termination

The geometries and energy profiles belonging to each reaction step on O_{oct2Cr} surface termination are displayed in Figure 4.6. The relative energies of redox mechanism steps on O_{oct1} termination are listed in Table 4.4. The molecular bond lengths of CO, CO₂, H₂O, and H₂ were found the same as previously given. The adsorption energy of carbon monoxide was evaluated from total energy calculations as -46.6 kcal/mol without an activation barrier. When CO adsorbs on the surface O atom ($O_{lattice}$), the distance between the C- $O_{lattice}$ is 1.185 Å and the distance between C and O of carbon is 1.155 Å. Desorption of produced CO₂ from the surface requires an energy of 19.8 kcal/mol that creates an O vacancy ($[]_{O_{vac}}$) on the surface. The dissociative adsorption energy of water on the O_{oct2Cr} surface vacancy site was evaluated as -55.12 kcal/mol. When the H₂O molecule adsorbs on the vacancy, the distance

between Fe and O atom of the hydroxyl group ($[\text{OH}]_{\text{Ovac}}$) is 1.954 Å and the Cr-O distance between of the hydroxyl group is 1.909 Å. The O-H bond length of this hydroxyl group is 0.980 Å. The distance between the H atom and the O atom that catches H atom is 0.977 Å. The energy changes as 71.0 kcal/mol after H_2 formation from the adsorbed water molecule.

Table 4.4. Regenerative mechanism steps of water gas shift reaction on Ooct2Cr surface

Reaction Step	Relative Energy, eV (kcal/mol)
$\text{CO}_{(\text{g})} + \text{O}_{\text{lattice}} \rightarrow \text{CO}_{2(\text{ads})}$	-2.0 (-46.6)
$\text{CO}_{2(\text{ads})} \rightarrow \text{CO}_{2(\text{g})} + []_{\text{Ovac}}$	0.9 (19.8)
$[]_{\text{Ovac}} + \text{H}_2\text{O}_{(\text{g})} \rightarrow [\text{OH}]_{\text{Ovac}} + [\text{H}]_{\text{ads}}$	-2.4 (-55.12)
$[\text{OH}]_{\text{Ovac}} + [\text{H}]_{\text{ads}} \rightarrow \text{H}_{2(\text{g})} + \text{O}_{\text{lattice}}$	3.1 (71.0)

Direct hydrogen-hydrogen interaction method and hydrogen atom desorption method were also studied as possible methods to produce hydrogen from water.

In the direct hydrogen-hydrogen interaction method, the hydrogen atom on lattice oxygen is sent to the hydrogen of the hydroxyl group (OH^-) and is allowed to produce molecular H_2 desorbs from the surface to the gas phase. The initial geometry and steps for hydrogen formation are illustrated in Figure 4.7a with the final geometry shown in Figure 5.7b. There is an energy difference of 69.64 kcal/mol between the initial and final steps.

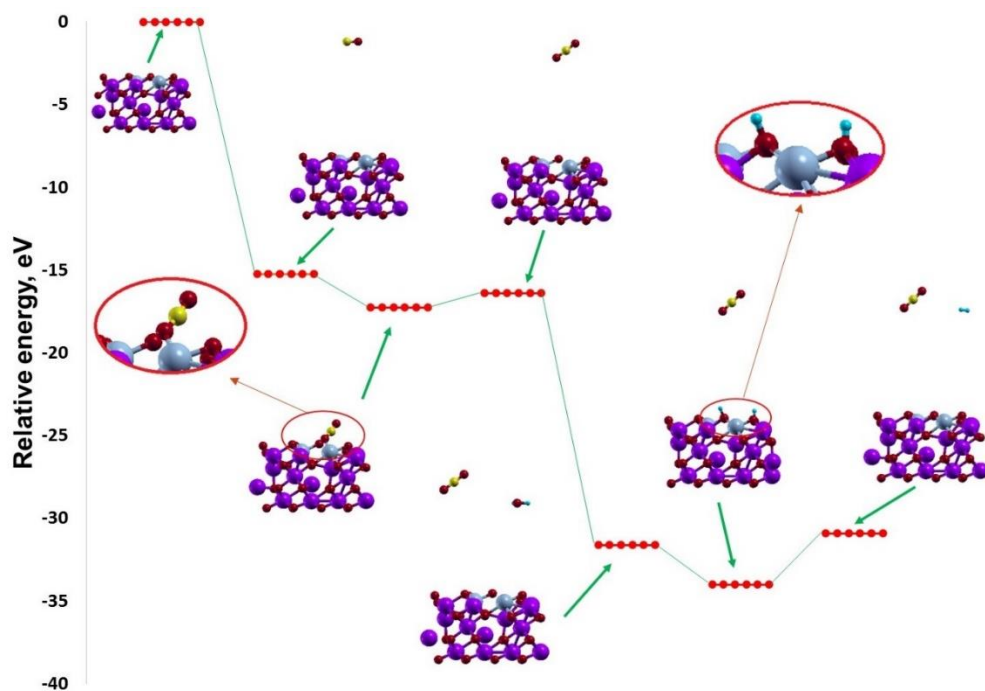


Figure 4.6. Energy profiles & optimized configurations of reaction steps on Ooct2Cr surface (Fe: purple, O: red, Cr: gray, C: yellow, H: blue)

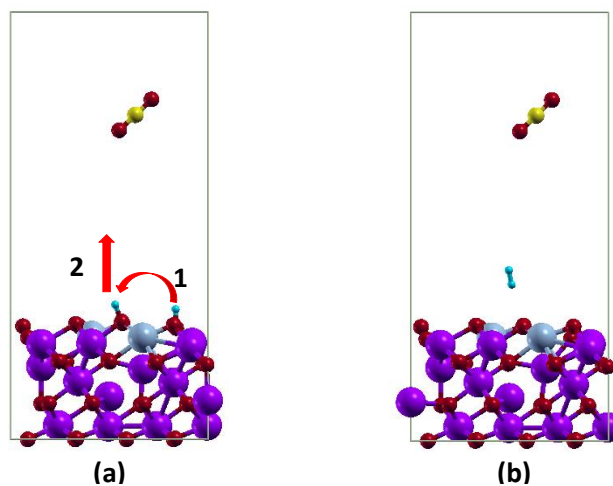


Figure 4.7. Direct hydrogen-hydrogen interaction for Ooct2Cr termination (a) initial geometry (b) final geometry (Fe: purple, O: red, Cr: gray, C: yellow, H: blue)

The hydrogen atom desorption method is illustrated in Figure 4.8. In this method, one of the hydrogen atoms desorbs from the surface with the hydrogen

atom on lattice oxygen being selected (Figure 4.8a). After obtaining the desorption of one hydrogen atom, another hydrogen atom is allowed to desorb (Figure 4.8b). Both atoms directly form hydrogen molecule since the gas phase radicals. Desorption of the first hydrogen requires an energy of 116.5 kcal/mol. With such a large value making this method energetically unfavorable. There is an energy difference of 46.6 kcal/mol between desorption of the second hydrogen atom and the final geometry.

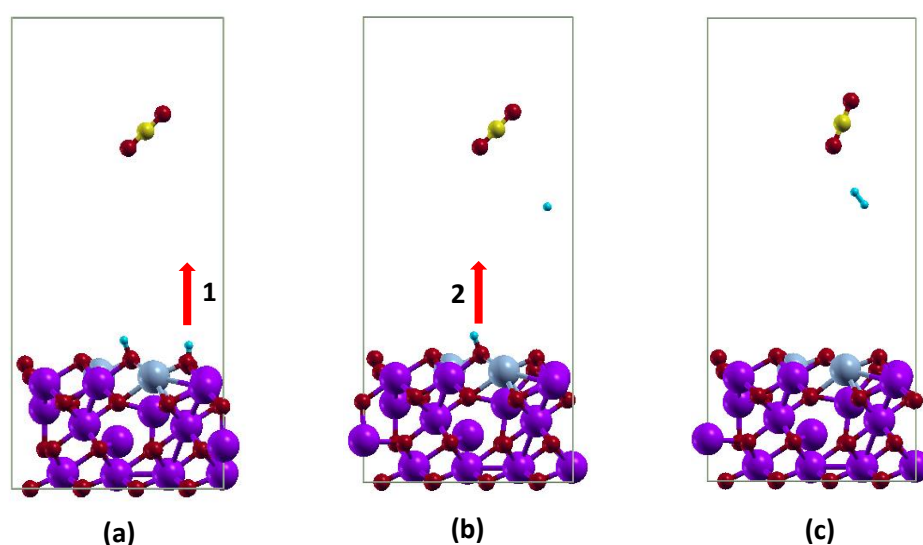


Figure 4.8. Hydrogen atom desorption for Ooct2Cr termination (a) desorption of first hydrogen atom (b) desorption of second hydrogen atom (c) final geometry (Fe: purple, O: red, Cr: gray C: yellow, H: blue)

When the regenerative WGS mechanism on these two different terminated surfaces is compared, CO adsorption is more favorable on the O_{oct1} surface with lower adsorption energy and in the presence of Cr, the dissociative adsorption of H₂O also exhibits with a relatively lower adsorption energy. The presence of the chromium atom on the surface, thus, eases the dissociative adsorption of water molecule. This maybe an indication of a catalytic effect of chromium on the water gas shift reaction. The CI-NEB (climbing image nudged

elastic band) method, however, would help to calculate activation barriers for assessing this effect correctly.

4.2.3.2.3. Bader Charge Analysis of Regenerative Mechanism on O_{oct1} and O_{oct2}Cr

In order to understand the underlying effects of the presence of Cr atoms on the surface, Bader charge analysis¹³² for all atoms has been implemented on O_{oct1} and O_{oct2}Cr surfaces via the redox mechanism. To discuss the bond formation in the adsorption of CO and H₂O, Bader charges of selected atoms on the catalytic surfaces were calculated. Figures 4.9 and 4.10 show the selected atoms to compare with respect to their Bader charges that are tabulated in Table 4.5 for CO adsorption. In addition, Figures 4.11 and 4.12 illustrate the selected atoms under the effect of H₂O adsorption and the corresponding charge values are given in Table 4.6.

In this charge calculation, the total charge was maintained neutral and the electrons were shared between the atoms. In case of CO adsorption, the positive charge values of the C atom increase while the negative charge values of the lattice oxygen atom to which CO adsorbs increases. This increase of the negative charge value on the lattice oxygen, however, remains and the related charges on the atoms are the nearly same for CO_(ads) and CO_{2(g)}. The charge on the oxygen atom that is not related directly to CO adsorption does not change much. The positive charge values of the Cr atoms are higher than the values of the Fe atoms. Generally, the positive charge on the metal atoms (Fe and Cr1) slightly decreases. This charge distribution may reveal that electrons are transferred from C to the lattice O atom.

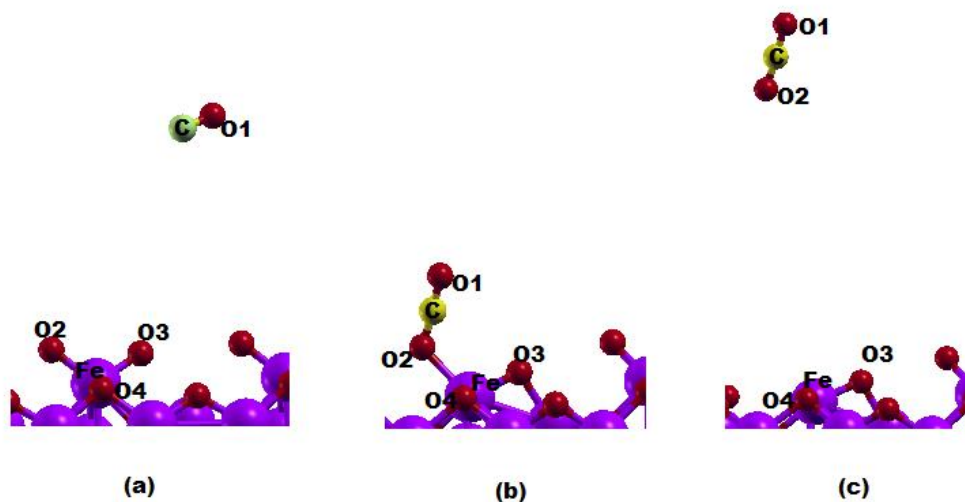


Figure 4.9. Selected atoms of CO adsorption on O_{oct1} surface (Fe: purple, O: red, C: yellow)

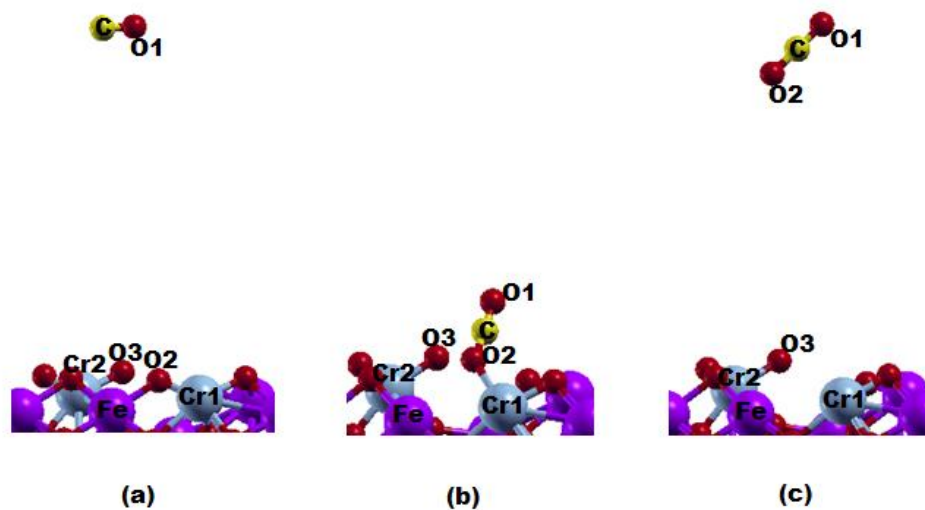


Figure 4.10. Selected atoms of CO adsorption on O_{oct2Cr} surface (Fe: purple, O: red, C: yellow, Cr: gray)

Table 4.5. Bader charge of selected atoms for CO adsorption on the surfaces

Atom	O _{oct1}			Ooct2Cr		
	CO (g)	CO (ads)	CO ₂ (g)	CO (g)	CO (ads)	CO ₂ (g)
C	1.13	2.11	2.08	1.12	2.15	2.11
O1	-1.13	-0.96	-1.04	-1.12	-1.01	-1.06
O2	-0.64	-1.08	-1.04	-0.66	-1.13	-1.06
O3	-0.65	-0.78	-0.76	-0.64	-0.64	-0.63
O4	-0.76	-0.82	-0.78			
Fe	1.43	1.32	1.31	1.28	1.26	1.25
Cr1				1.81	1.69	1.65
Cr2				1.82	1.76	1.75

For non-dissociative adsorption of H₂O at the vacancy of the O_{oct1} surface, the charge of the system remains the same. For the dissociative adsorption of H₂O at the vacancy of the O_{oct1} surface, the charge on H remains nearly the same but the negative charge on the lattice O increases with the H atom adsorption. The charge value on the Cr atoms is again higher than on the Fe atoms. For the dissociative adsorption pathway, electrons transfer from the Cr metal to the lattice O. The presence of Cr atoms with a more positive charge makes neighboring oxygen atoms more electronegative and this may be the reason of the different adsorption on the Cr substituted surface.

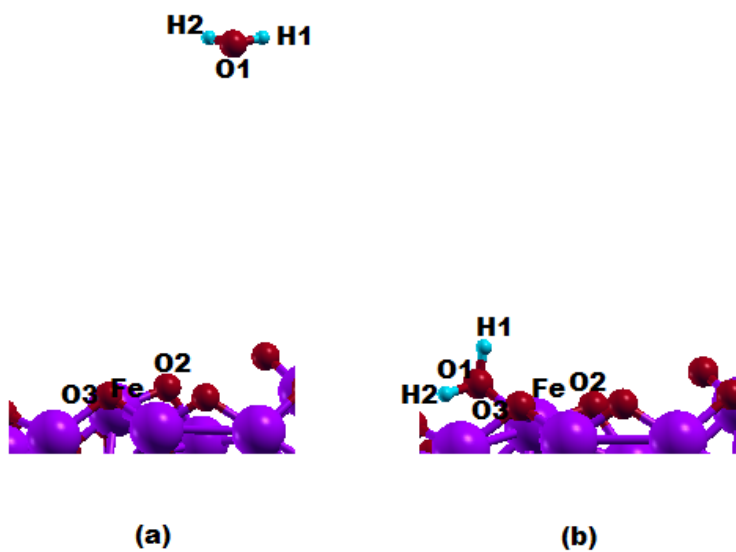


Figure 4.11. Selected atoms of H₂O adsorption on O_{oct1} surface (Fe: purple, O: red, H: blue)

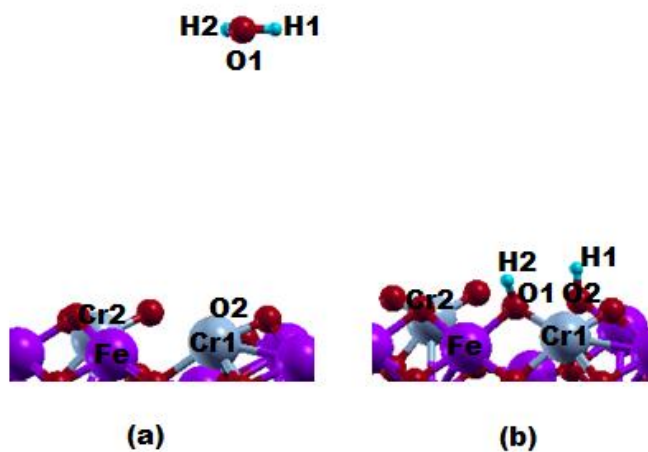


Figure 4.12. Selected atoms of H₂O adsorption on O_{oct2Cr} surface (Fe: purple, O: red, H: light blue, Cr: gray)

Table 4.6 Bader charge of selected atoms for H₂O adsorption on the surfaces

Atom	O _{oct1}		O _{oct2Cr}	
	H ₂ O (g)	H ₂ O (ads)	H ₂ O (g)	H ₂ O (ads)
H1	0.60	0.65	0.61	0.61
H2	0.61	0.66	0.63	0.64
O1	-1.19	-1.16	-1.23	-1.06
O2	-0.76	-0.76	-0.79	-1.06
O3	-0.78	-0.80		
Fe	1.31	1.34	1.39	1.31
Cr1			1.65	1.73
Cr2			1.76	1.83

4.2.3.2.4. Vibrational Frequency Calculations

The vibrational frequencies are the characteristic information for each molecule. The vibrational frequency calculations were first applied for CO and CO₂ molecules in the gas phase under the vacuum the conditions and the frequency values for both the calculated and experimental vibration from the NIST database¹³³ are listed in Table 4.7.

Table 4.7 Calculated and experimental vibrational frequency values of CO and CO₂ in unit of cm⁻¹

	CO		CO ₂	
	Theoretical	Experimental ¹³³	Theoretical	Experimental ¹³³
Symmetric	2175	2170	1340	1333
Asymmetric			2429	2349
Bend			647 - 633	667

The differences between the calculated and experimental vibrational frequency values for CO and symmetric stretching of CO₂ are nearly same. The

3% difference between the values of asymmetric and bending stretching of CO₂ may be acceptable. It is important to keep in mind that DFT is a very successful technique for understanding the vibrational properties of molecular systems, but these calculations also depend on the calculation approach such as basis sets and exchange functionals¹¹⁷.

The vibrational frequency calculations are also applied for the CO adsorption step on the O_{oct1} and Ooct2Cr surfaces. The O_{oct1} and Ooct2Cr surfaces during CO adsorption step are shown in Figures 4.9 and 4.10, respectively, and the corresponding calculated frequency values are given in Table 4.8.

Table 4.8. Vibrational frequency values (cm⁻¹) of CO adsorption on O_{oct1} and Ooct2Cr

		Ooct1	Ooct2Cr	Difference,%
CO _{gas}		2176	2174	-0.12
CO _{ads}	Symmetric	1297	1338	3.15
	Asymmetric	2407	2398	-0.37
	Bend	541-607	531-600	-1.15 -- -1.85
CO _{2gas}	Symmetric	1359	1345	-0.99
	Asymmetric	2431	2422	-0.35
	Bend	625-636	637-644	1.19 – 2.00

The vibrational frequency values of the CO and CO₂ molecules with and without the surfaces in the same vacuum volume are not exactly the same. The reason may be the tags in the INCAR file to define the calculation specifications for the surfaces. The frequency values are not identical for the O_{oct1} and Ooct2Cr surfaces. While some kinds of stretching values are greater on one surface, the remaining stretching values are greater on the other surface. There is no regular increasing or decreasing trend. The differences percentages are also given in Table 4.8. These values are not too great but the presence of Cr in the system create differences and also affects the vibrational frequencies of the CO and CO₂

molecules in the gas phase. The bigger difference created by the presence of Cr in the structure is the symmetric stretching values of CO.

Stretching values when CO adsorbs on the surface are close, but less than the stretching frequency values of produced CO₂ molecule which leaves the surface. In the present study, the CO tends to adsorb on a lattice O atom site since cleaved surfaces are terminated with O atoms. The similarity between the CO_{ads} and CO₂ in the gas phase demonstrate that there is chemisorption of CO on the oxygen terminated surface. The frequency difference between adsorbed and gas-phase C-O should be interpreted in terms of chemisorption bond strength only. The formation of a chemisorption bond between C-O and the substrate alters the distribution of electrons over the molecular orbitals and weakens the C-O bond. Generally, the linearly adsorbed CO exhibits its vibrational frequency in the range of 2000-2200 cm⁻¹ ⁹⁷.

4.3. Conclusions

Regenerative mechanism steps of water gas shift reaction on bare and Cr substitute (111) surface of Fe₃O₄ as high temperature shift catalyst are studied using DFT. 5 eV Hubbard parameter is suitable to build the Fe₃O₄ bulk structure where lattice parameters are in line with experimental values. The O_{oct1} termination which reveals four O atoms over a layer of three Fe atoms located at octahedral sites is studied among the six Fe₃O₄ (111) terminations. According to the Cr atom substitution on this surface, Cr atoms prefer being on the surface rather than in the bulk structure. The percentage of 9% Cr₂O₃/Fe₂O₃ in the experimental studies corresponds approximately two Cr atoms in the optimized O_{oct1} structure in this study. Therefore, O_{oct2}Cr is optimized where 2 Cr atoms are substituted with iron atoms which are located on octahedral site. Adsorption energies of CO on O_{oct1} and O_{oct2}Cr are respectively found as -96 kcal/mol and -47 kcal/mol. Water adsorption on O_{oct1} surface is molecular with -54.88 kcal/mol of adsorption energy; whereas, water adsorption on O_{oct2}Cr surface is

dissociative with nearly same adsorption energy, -55.12 kcal/mol. This is an indication of a catalytic effect of chromium on water-gas shift reaction; however, activation barrier calculations should be necessary to assess this effect correctly.

CHAPTER 5

CuO-Cr₂O₃-Fe₂O₃ CATALYSTS IRON TERMINATED Fe₃O₄ (111) SURFACE

5.1. Abstract

Fe_{oct2} termination of Fe₃O₄ (111) and Cr atoms substituted Fe₃O₄ (111) slab surfaces as the HT-WGS catalysts are investigated by means of spin-polarized periodic DFT approach using the Vienna Ab-initio Simulation Package (VASP) with the projector-augmented wave (PAW) method. The DFT calculations indicate that Cr atoms prefer being below the FeO₆ sites. There is a minor effect of Cr on the dissociative H₂O adsorption but no effect on the CO adsorption indicating that Cr does not act as a chemical promoter. Copper promotion of Fe_{oct2} structure with a Cu₄ cluster facilitates the CO adsorption at the new active sites on the copper-iron oxide interfacial.

5.2. Results and Discussion

5.2.1. Bulk Optimization

The Fe₃O₄ iron oxide phase has a cubic, inverse spinel structure with the space group of *Fd3m*. With the application of Hubbard and exchange parameters to consider on-site Coulomb interaction of d-Fe orbitals (GGA+U), Fe₃O₄ structure is defined with the lattice parameter of 8.4537 Å which is in agreement with the experimental one (8.3941 Å¹²²) when U-J is 4 eV⁸⁶. In addition, the bond distances of Fe_{tet}-O and Fe_{oct}-O are found as 1.9061 and 2.0706 Å, respectively. They are in good agreement with the experimental values of 1.888 and 2.0584 Å, respectively¹²². The optimized structure of Fe₃O₄ is given in Figure 5.1. In the spin-polarized calculations, the initial magnetic moments were set as ferrimagnetic structure (opposite spins in the tetrahedral and octahedral

sites). The magnetic moments of both Fe atoms at tetrahedral site, Fe atoms at octahedral sites, and O atoms are calculated to be 4.06, 3.95 –3.96, and 0.04 μ_B , respectively. These results are consistent with previous bulk calculations of Fe_3O_4 where net magnetic moments for bulk Fe_{oct} , Fe_{tet} , and O atom are found to be 3.96-3.98 μ_B , 4.09 μ_B , and 0.03 μ_B with GGA (PBE)+U ($U_{eff} = 4$ eV)¹³⁴. Moreover the total spin magnetization per formula unit is 4.012 μ_B which is very close to the experimental value of 4.05 μ_B ¹²⁹.

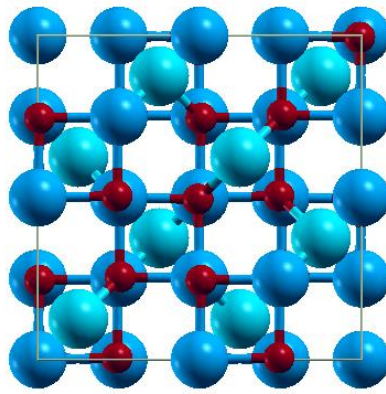


Figure 5.1. Bulk structure of Fe_3O_4 with spin polarized GGA+U (Fe_{tet} : light blue, Fe_{oct} : blue, O: red)

5.2.2. Surface Optimization

Fe_3O_4 (111) surface which is the predominant natural growth face¹²¹ was cleaved with six different terminations. (2x1x1) supercells were prepared. All layers except the bottom layer of 6 layered surfaces were allowed to relax. Among the six different terminations, Fe_{tet1} and Fe_{oct2} are the energetically most stable surfaces. Using Eq. (3.18), the surface energy of Fe_{tet1} is found to be 0.9198 J/m² and the surface energy of Fe_{oct2} is calculated as 0.9197 J/m². The optimized structures of Fe_{tet1} and Fe_{oct2} are shown in Figure 5.2. The corresponding a, b, c, and β lattice parameter values are 11.9553, 5.9776, 19.2707 Å, and 120°, respectively. The Fe_{tet1} termination reveals one Fe atom

layer located at a tetrahedral site over a four oxygen atom layer. The $\text{Fe}_{\text{oct}2}$ termination reveals two Fe atom layers located at octahedral (topmost) and tetrahedral sites over a four oxygen atom layer. $\text{Fe}_{\text{tet}1}$ termination is observed in naturally grown single crystals at room temperature, whereas $\text{Fe}_{\text{oct}2}$ appears only when the sample is prepared under oxygen conditions¹³⁴. Magnetite structure is obtained under reducing conditions from hematite structure. Therefore, $\text{Fe}_{\text{oct}2}$ is selected for further studies. In the side view of $\text{Fe}_{\text{oct}2}$ (Figure 5.2.b), $\text{Fe}_{\text{oct}2}$, $\text{Fe}_{\text{tet}1}$, $\text{O}_{\text{oct}1}$, $\text{Fe}_{\text{oct}1}$, $\text{O}_{\text{oct}2}$, and $\text{Fe}_{\text{tet}2}$ layers are seen from top to bottom. Magnetization properties change for different surface structures. The magnetization values for bulk structure tetrahedral sites are exactly the same; however, the value of the second layer from the top $\text{Fe}_{\text{tet}1}$ is lower ($3.691 \mu_{\text{B}}$) than the value of the bottom layer of $\text{Fe}_{\text{tet}2}$ ($3.906 \mu_{\text{B}}$). The topmost layer, $\text{Fe}_{\text{oct}2}$, has a magnetization value as $3.565 \mu_{\text{B}}$ and the other Fe layer, $\text{Fe}_{\text{oct}1}$, has a magnetization value of $4.197 \mu_{\text{B}}$. The magnetization of O atoms are different at different locations but all are very close to zero. Ferromagnetic ordering remains also in the surface structure. The difference in the magnetization of surface and bulk structures are in line with the calculated values in the theoretical study of Noh et al¹³⁴.

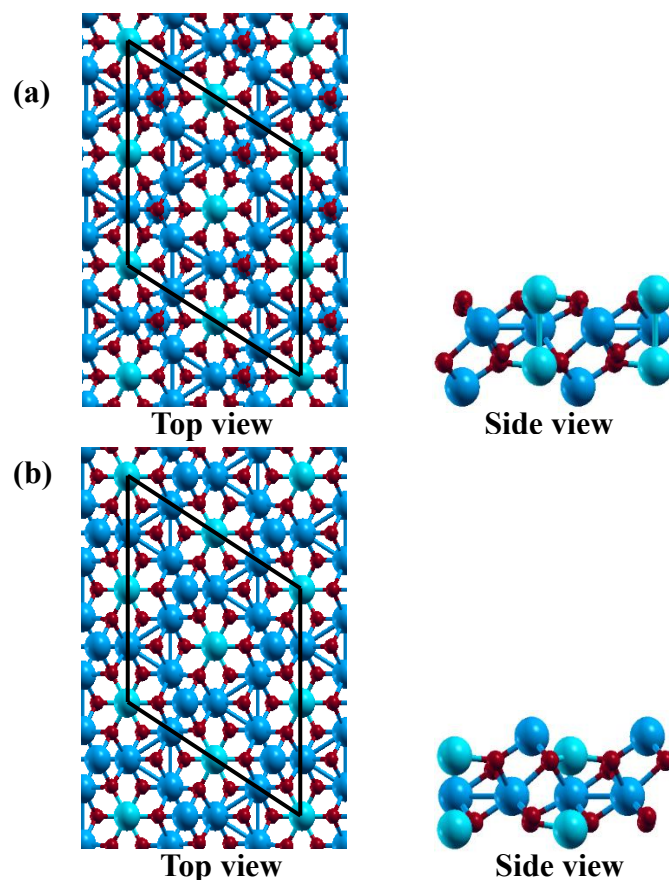


Figure 5.2. Optimized structures of (a) Fe_{tet1} and (b) Fe_{oct2} terminations (Fe_{tet}: light blue, Fe_{oct}: blue, O: red)

5.2.3. Chromium Substitution on the Fe_{oct2} Surface

In order to understand the effect of chromium atoms in the structure, the structures with two Fe atoms replaced by two chromium atoms at different sites were prepared. As shown in Figure 5.3, mainly four different locations in the initial Fe_{2.75}Cr_{0.25}O₄ structures were selected for Cr atoms. It is thought that chromium can make substitutional solid solution having complete solubility with iron atom since Fe and Cr atoms have BCC structure with very close atomic radii (0.124 and 0.125 nm, respectively) and electronegativities (1.8 and 1.6, respectively)¹²³. Moreover, *operando* NAP-XPS-MS spectra, *in situ* XANES spectra, and HS-LEIS depth profile of activated Cr₂O₃-Fe₂O₃ catalyst show that

Cr³⁺ is incorporated into the iron oxide bulk lattice forming Fe_{3-x}Cr_xO₄ mixed oxide solid solution phase³⁸. According to the magnetization properties (spin up or spin down) at the specific location, a different initial magnetization guess was made for each initial structure guess as given in Table 5.1.

Table 5.1. Energy change and magnetic moment of Cr doped Fe_{oct2} surface

Surface	Initial Magnetic Moment (μ_B) Guess for Cr	Optimized Magnetic Moment (μ_B) of Cr	Energy Change (eV)
Feoct2_Cr_oo_1	2*2	3.847	-2.0
Feoct2_Cr_oo_2	2*0	3.174	-2.3
Feoct2_Cr_oo_3	2*-4	-3.686	-2.2
Feoct2_Cr_ot_1	2*2	3.825 (oct) – 2.920 (tet)	-2.0
Feoct2_Cr_to_1	2*2	2.874 (tet) – 3.028 (oct)	-3.2
Feoct2_Cr_to_2	2*0	2.867 (tet) – 1.031 (oct)	-2.2
Feoct2_Cr_to_3	1*2 1*-2	2.863 (tet) – -2.988(oct)	-3.2
Feoct2_Cr_ooa_1	2*-2	-2.977	-4.5
Feoct2_Cr_ooa_2	2*2	3.039	-4.6

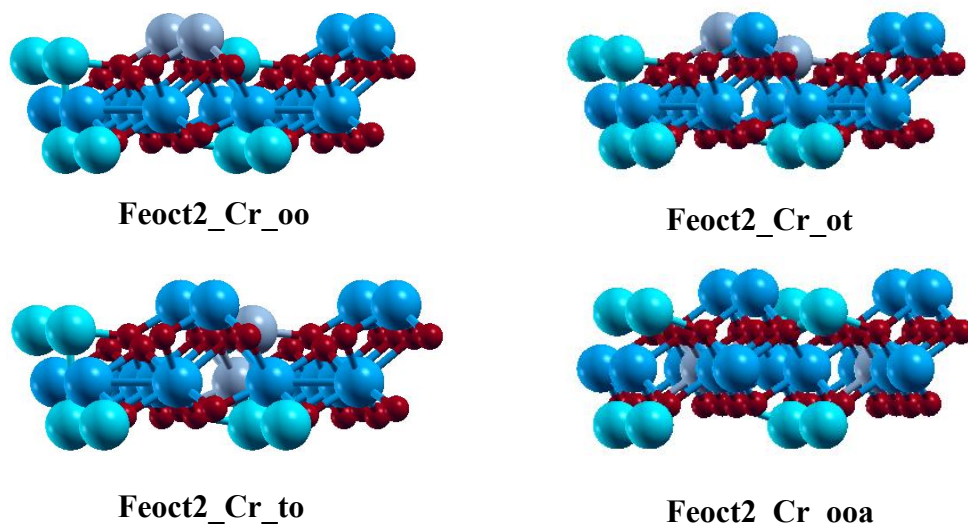


Figure 5.3. Initial structures of differently located Cr atoms in $\text{Fe}_{\text{oct}2}$ structure (Fe_{tet} : light blue, Fe_{oct} : blue, O: red, Cr: gray)

In this figure, Feoct2_Cr_oo means that Cr atoms are located at topmost octahedral site. Feoct2_Cr_ot means that one Cr atom is located at topmost octahedral site and another Cr atom is located at uppermost tetrahedral site. Feoct2_Cr_to means that one Cr atom is located at uppermost tetrahedral site and another Cr atom is located at below octahedral site. Feoct2_Cr_ooa means that two Cr atoms are located at below octahedral site. Magnetization values of Fe atoms at tetrahedral and octahedral sites are in opposite sign. In some cases the same sign, in some other cases the opposite sign of magnetization value were taken for Cr atoms. Using Eq. (3.19), the minimum energy of the structure was observed for Feoct2_Cr_ooa structure as given in Table 5.1. According to this result, it can be said that chromium atoms in $\text{Fe}_{\text{tet}}(\text{Fe}_{1.75}\text{Cr}_{0.25})_{\text{oct}}\text{O}_4$ are not exactly located at uppermost layers. There is not any reconstruction of the surface. The optimized structure is given in Figure 5.4. Cr atoms prefer being below FeO_6 sites and this result is in line with the HT-LEIS³⁸ surface analysis of Cr-Fe oxide catalyst activated under WGS reaction conditions and the ^{57}Fe Mössbauer study^{135,136} of $(\text{Fe}^{3+})(\text{Fe}_{1-x}^{3+}\text{Fe}^{2+}\text{Cr}_x)\text{O}_4$. The magnetic moment of Cr atoms are $3.039 \mu_B$. This value is opposite and smaller than the magnetic

moment values ($-4.183 \mu_B$) of Fe atoms in the same layer. There are some increases and decreases in the magnetic moment values of Fe atoms; however, these differences are not dramatic. The opposite sign of Cr atoms in their layer decreases the net magnetic moment of the structure that is in line with the Mössbauer analysis¹³⁵, which shows the decrease in magnetic moment with the Cr concentration increasing.

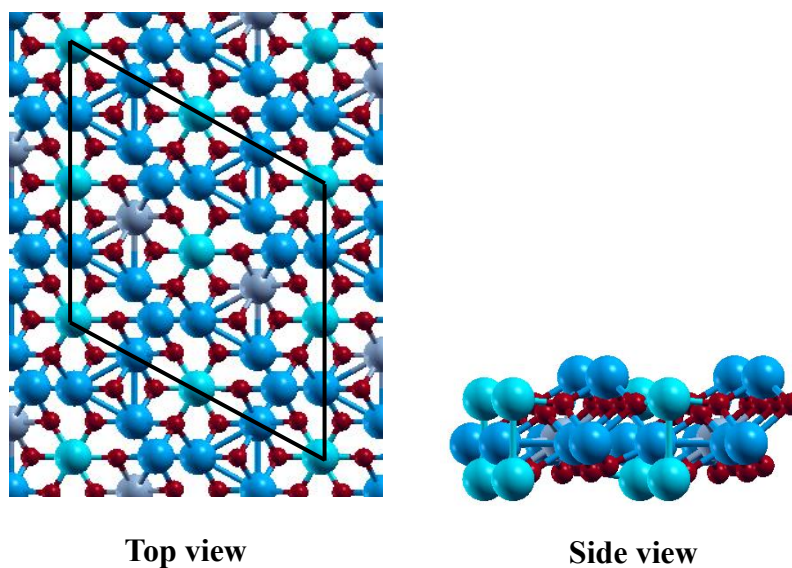


Figure 5.4. Optimized structure of Feoct2_Cr_ooa surface (Fe_{tet}: light blue, Fe_{oct}: blue, O: red, Cr: gray)

5.2.4. Reduction of the Fe₃O₄ (111) Surface

A DFT study of Huang et al. (2015)⁸⁶ showed that redox mechanism was the energetically most favorable pathway for the water gas shift reaction on the Fe_{oct2-tet1}-terminated Fe₃O₄ (111) surface when they compared three possible reaction mechanisms, namely the redox, associative, and coupling mechanisms. For the redox mechanism, they proposed the total dissociation of water molecule to H and O atoms and the oxidation of CO by atomic oxygen, which is left on the bridge site. However, a recent study of temperature-programmed surface reaction (TPSR) spectroscopy (CO-TPSR, CO+H₂O-TPSR, and HCOOH-

TPSR)³⁷ demonstrated for the first time that HT-WGS reaction follows the redox mechanism, and the associative mechanism does not take place. CO is firstly oxidized by lattice surface oxygen and creates surface vacant sites for re-oxidation by H₂O.

In order to understand the active oxygen sites for CO adsorption, different positions for the creation of the O vacancies in the Fe_{tet1}, Fe_{oct2} and Feoct2_Cr_oaa surfaces to find the lowest-energy configuration were explored. Figures 5.5a and 5.5b show the different oxygen sites of Fe_{tet1} and Fe_{oct2} surfaces, respectively. Table 5.2 gives the energies for the oxygen formation.

The calculations show that the O₂ triplet ground state has an equilibrium bond length of 1.23 Å and a binding energy of -6.14 eV, which lies 0.97 eV below the experimental binding energy (-5.17 eV)¹³⁷. Therefore, half of the over-binding of the O₂ molecule, 0.49 eV, has been also added to correct the vacancy formation energies with respect to one O atom⁷⁷.

Oxygen atom, which is located at topmost layer and bonds to bottom Fe atoms located at octahedral site, is energetically favorable for the oxygen vacancy formation of Fe_{oct2} surface. The oxygen vacancy formation energy is higher on the Fe_{tet1} surface. Top most layer tends to lose oxygen with a lower vacancy formation energy.

Table 5.2. Oxygen vacancy formation energies on Fe_{oct2} and Fe_{tet1} surfaces

Fe _{oct2}			Fe _{tet1}		
Oxygen Position	E _{vac} (eV)		Oxygen Position	E _{vac} (eV)	
	Uncorrected	Corrected		Uncorrected	Corrected
V1	2.6	3.09	V1	3.0	3.49
V2	3.2	3.69	V2	3.8	4.29
V3	3.5	3.99			

Cr atoms in the lattice affect the energy of oxygen vacancy formation. The schematic representation of the (111) surfaces with and without Cr atoms

after relaxation is shown in Figure 5.6. The required energy for oxygen vacancy is increased by the presence of Cr in the structure for the same sites of $\text{Fe}_{\text{oct}2}$ and Cr-doped $\text{Fe}_{\text{oct}2}$ ($\text{Fe}_{\text{oct}2}\text{-Cr}_{\text{ooa}}$), Table 5.3. This result is in line with the kinetic measurements. Steady-state WGS kinetics³⁸ over Fe_2O_3 and 8wt.% Cr-iron oxide catalysts show that the apparent activation energy is 85 kJ/mol for iron oxide catalysts; whereas this value is 105 kJ/mol for Cr-iron oxide catalysts. These results verify that chromium is a textural promoter and does not have a positive effect on the catalytic activity.

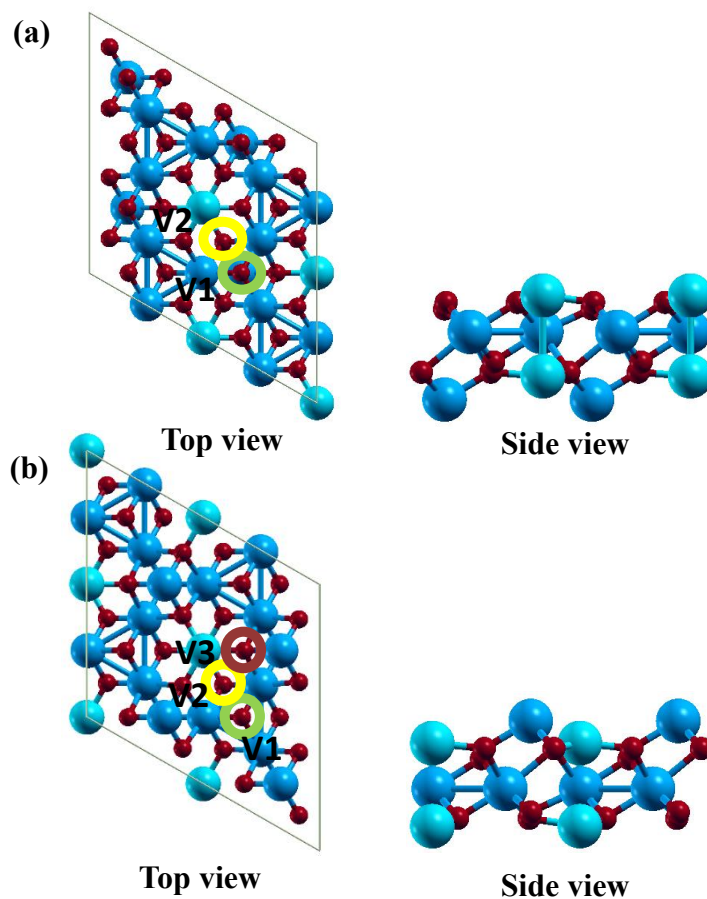


Figure 5.5. Possible oxygen sites on (a) $\text{Fe}_{\text{tet}1}$ surface and (b) $\text{Fe}_{\text{oct}2}$ surface (Fe_{tet} : light blue, Fe_{oct} : blue, O: red)

A Bader charge analysis¹³² was performed to see the charge distribution on the atoms while keeping the total charge as neutral and allowing the electron sharing between the atoms. Selected atoms on Fe_{oct2} and Cr-Fe_{oct2} surfaces are shown in Figure 5.4 and the charge values are given in Table 5.4. The charge of the Cr atom is lower than the charge of the Fe atoms. This makes a slight increase in the electronegativity of the O atom, which is directly bonded to Cr. After vacancy formation, the Fe atoms and the Cr atom, which are close to the vacancy show a variation in charge of 0.17 e⁻. The positive charge of a Fe atom at the topmost layer is just decreased by a negligible amount (0.01 e⁻), where this small variation may be accounted by the defect that was created at the relatively farthest O location. The electronegativity of the other O atoms at the same row was not affected much.

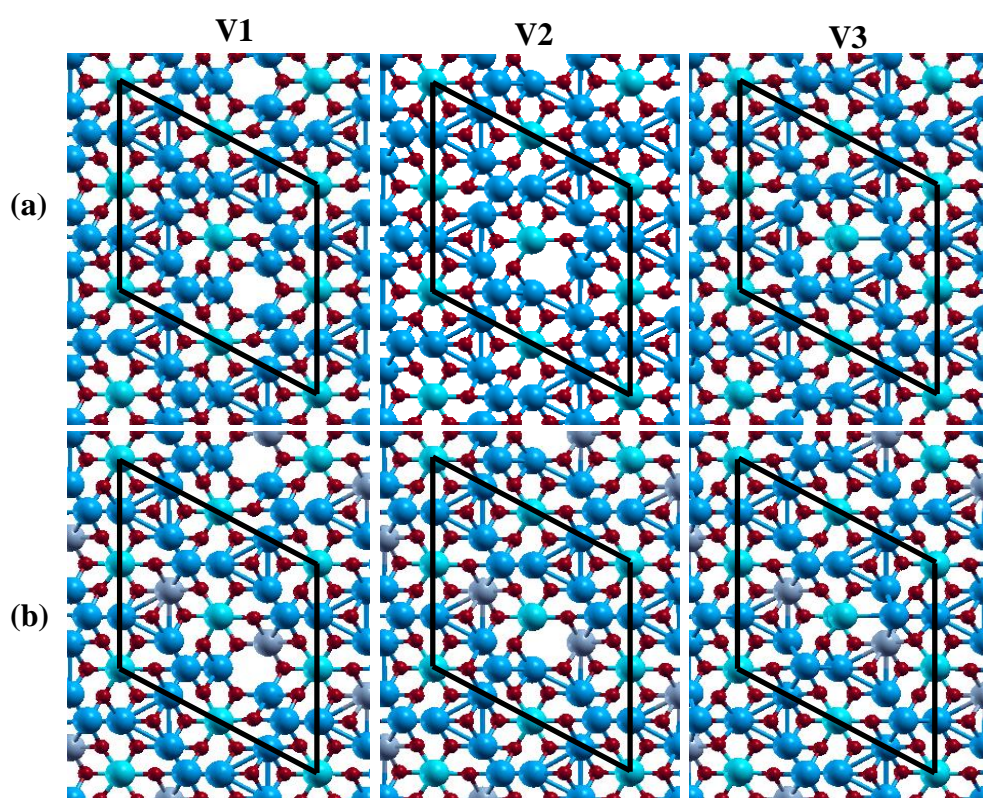


Figure 5.6. Top view of the schematic representation of the (111) surface after relaxation: (row a) Fe_{oct2} and (row b) Fe_{oct2}_Cr_oaa surface (Fe_{tet}: light blue, Fe_{oct}: blue, O: red, Cr: gray)

Table 5.3. Oxygen vacancy formation energies on Fe_{oct2} and Feoct2_Cr_ooa surfaces

Fe _{oct2}			Feoct2_Cr_ooa		
Oxygen Position	E _{vac} (eV)		Oxygen Position	E _{vac} (eV)	
	Uncorrected	Corrected		Uncorrected	Corrected
V1	2.6	3.09	V1	2.7	3.19
V2	3.2	3.69	V2	3.4	3.89
V3	3.5	3.99	V3	3.9	4.39

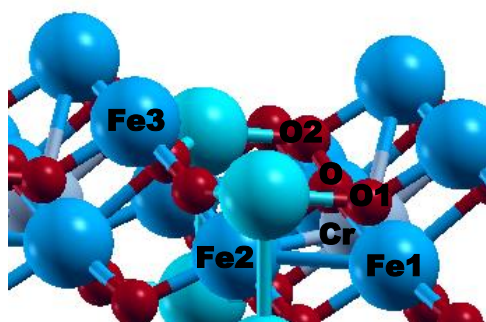


Figure 5.7. Selected atoms on Feoct2_Cr_ooa for Bader charge comparison (Fe_{tet}: light blue, Fe_{oct}: blue, O: red, Cr: gray)

Table 5.4. Bader charges of selected atoms on Fe_{oct2} and Feoct2_Cr_ooa surfaces before and after oxygen vacancy

Atom	Fe _{oct2}		Feoct2_Cr_ooa	
	Clean Surface	Oxygen Vacancy (V1)	Clean Surface	Oxygen Vacancy (V1)
Fe-Cr	1.70	1.53	1.67	1.50
O	-1.12		-1.11	
O1	-1.19	-1.20	-1.19	-1.19
O2	-1.19	-1.20	-1.19	-1.21
Fe1	1.70	1.55	1.70	1.52
Fe2	1.70	1.53	1.70	1.53
Fe3	1.20	1.19	1.19	1.18

5.2.5. Single H₂O and CO Adsorption on Fe_{oct2} and Feoct2_Cr_ooa Surfaces

5.2.5.1. H₂O Adsorption on Fe_{oct2} and Feoct2_Cr_ooa Surfaces

Single water molecule can adsorb with spontaneous dissociation to form OH and H surface species upon geometry optimization on both Fe_{oct2} and Feoct2_Cr_ooa surfaces. The related adsorption structure and the bond distances are shown in Figure 5.8. The calculated dissociative chemisorption energy is -1.7 eV (-38 kcal/mol) on Fe_{oct2} terminal surface and the energy for the Feoct2_Cr_ooa surfaces is -1.6 eV (-37 kcal/mol). This result corresponds to a strongly exothermic adsorption process and the calculated value is slightly more exothermic than the PBE+U(3.8)⁸³ calculation value (-1.5 eV). There is a minor effect of Cr on the water adsorption. The dissociation leads to two hydroxyl groups on both surfaces. OH group of H₂O tends to adsorb on a nearby Fe atom located at octahedral site; on the other hand, H atom is caught by a lattice oxygen

to form the second OH group. The bond length O_{lat}-H group is a little longer for the Cr substituted surface.

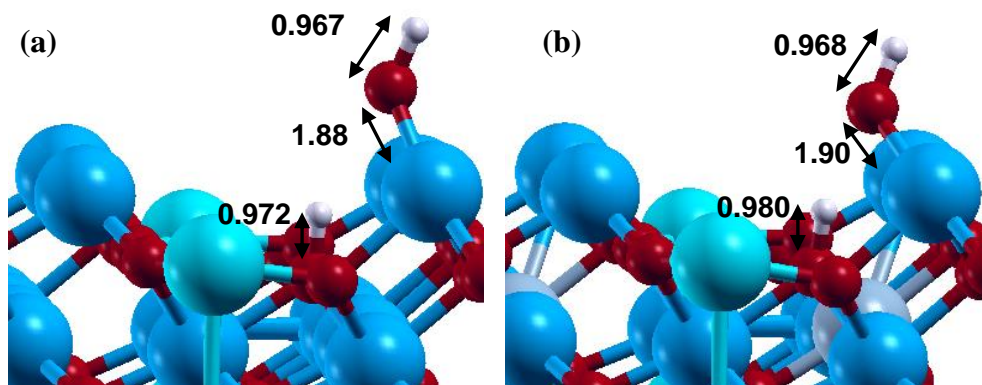


Figure 5.8. H₂O adsorption on the (a) Fe_{oct2} terminated and the (b) Fe_{oct2_Cr_ooa} terminated Fe₃O₄ (111) surface. The bond length unit is angstrom. (Fe_{tet}: light blue, Fe_{oct}: blue, O: red, Cr: gray, H: white)

5.2.5.2. CO Adsorption on Fe_{oct2} and Feoct2_Cr_ooa Surfaces

CO molecule on the both Fe_{oct2} and Feoct2_Cr_ooa surfaces tends to adsorb on the surface Fe_{oct} site. DFT⁸⁴ and experimental¹³⁸ studies also show that the on-top configuration is most favored. The adsorption energies of CO on the Feoct2 surface and Feoct2_Cr_ooa surfaces are the same (-0.96 eV or -22 kcal/mol). As seen in Figure 5.9, the distances between the O-C and C-Fe_{oct} are the same. This indicates that Cr substitution does not have an effect on CO adsorption. The effect may be seen on CO₂ formation using lattice O, which is bonded to Cr atom.

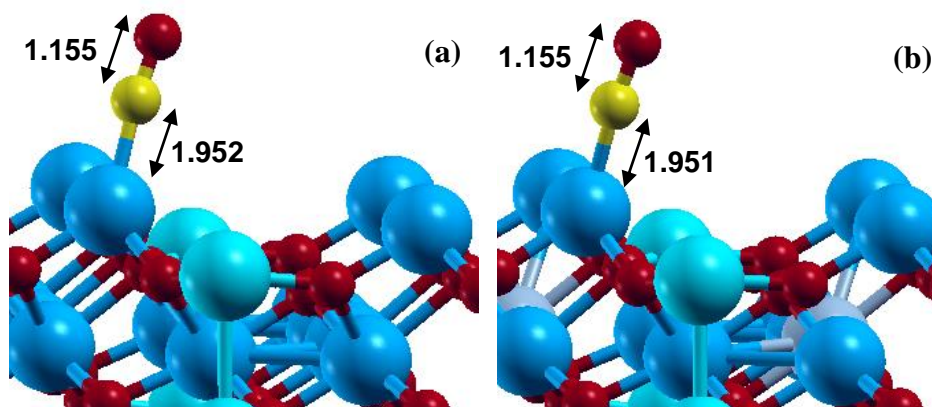


Figure 5.9. CO adsorption on the (a) Fe_{oct2} terminated and the (b) Fe_{oct2_Cr_ooa} terminated Fe₃O₄ (111) surface. The bond length unit is angstrom. (Fe_{tet}: light blue, Fe_{oct}: blue, O: red, Cr: gray, C: yellow)

5.2.6. H₂O Adsorption on Fe_{oct2} Termination

In order to understand the saturation effect on hydroxyls on the surface, adsorption of a second H₂O molecule is also studied. Figure 5.10 shows that there is also dissociative chemisorption on the similar oxygen site. The dissociative adsorption energy of second H₂O molecule is slightly lower than the first one with -1.6 eV (-37 kcal/mol). The study of Li et al. (2015)⁸³ also shows that bigger supercells contain more active sites to allow dissociative adsorption of H₂O. When the active sites are blocked by the H atoms water tends to adsorb molecularly. Presence of molecularly adsorbed water would make the model more realistic.

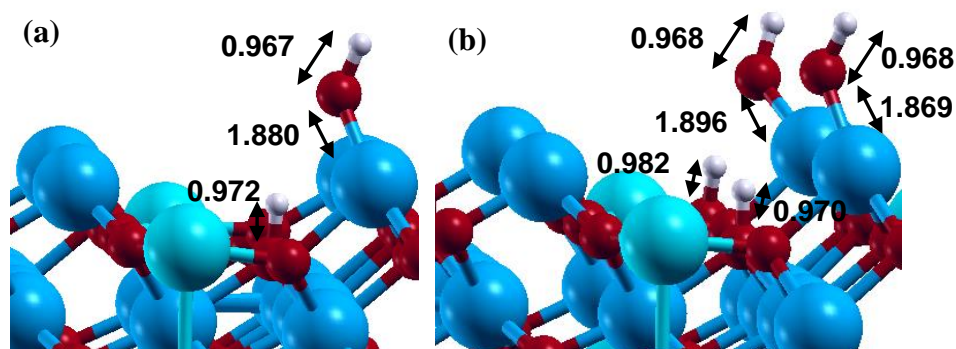


Figure 5.10. Structure optimized for (a) one and (b) two H₂O molecules adsorbed at the Fe_{oct2} terminated Fe₃O₄ (111) surface. The bond length unit is angstrom. (Fe_{tet}: light blue, Fe_{oct}: blue, O: red, H: white)

5.2.6.1. CO Adsorption on Fe_{oct2} Termination with Hydroxyl Groups

Adsorption of CO is compared with free surface and surface occupied by OH groups. Figure 5.11 shows the change in the atomic distances on the optimized structures of adsorbed CO and H₂O molecules. The adsorption energy of CO on surface Fe_{oct} atom was found as -0.96 eV (-22 kcal/mol). Presence of hydroxyl groups on the surface make easier the adsorption of CO with the adsorption energy calculated as -1.4 eV (-33 kcal/mol). However, further dissociative adsorption of H₂O makes harder the adsorption of CO. The adsorption energy of CO on the surface with 2 dissociated H₂O molecules was found to be -0.93 eV (-21 kcal/mol). The adsorption energy of CO molecule on the Fe_{tet} site (-0.42 eV or -10 kcal/mol) and the adsorption energy of CO molecule on the same Fe_{oct} site with OH (-0.66 eV or -15 kcal/mol) indicate that free Fe_{oct} sites are the most favorable sites for the CO adsorption. As seen from Figure 5.11, CO and H₂O tend to adsorb on the same Fe_{oct} site indicating the competition between the CO and H₂O molecules under the co-presence conditions⁸⁵. This may obstruct the adsorption of CO on the surface with a higher hydroxyl groups coverage.

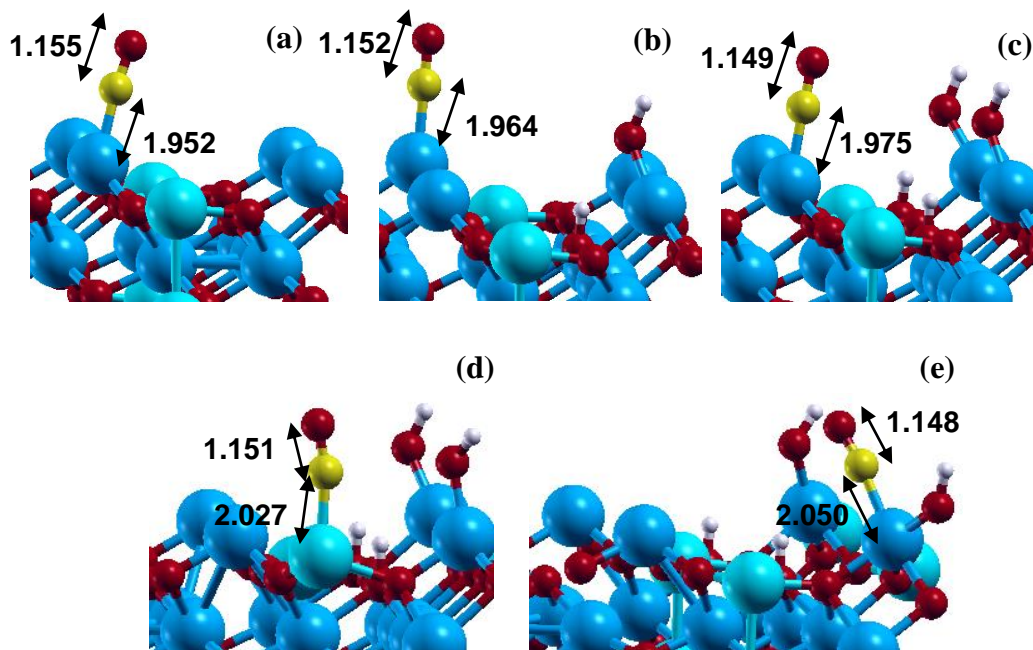
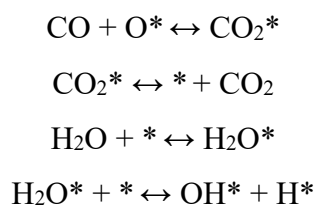
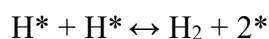
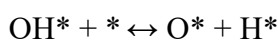


Figure 5.11. Optimized structure of CO adsorbed on the $\text{Fe}_{\text{oct}2}$ terminated Fe_3O_4 (111) surface (a) without a hydroxyl group, (b) with two hydroxyl groups, (c) with four hydroxyl groups (d) top of Fe_{tet} site, and (e) some Fe_{oct} site with OH group. The bond length unit is angstrom. (Fe_{tet} : light blue, Fe_{oct} : blue, O: red, H: white, C: yellow)

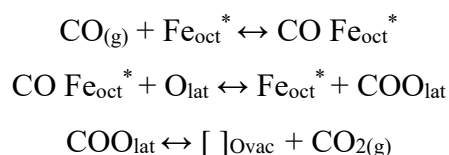
5.2.7. Redox Reaction on $\text{Fe}_{\text{oct}2}$ Termination

A recent study of temperature-programmed surface reaction (TPSR) spectroscopy (CO-TPSR, CO+H₂O-TPSR, and HCOOH-TPSR)³⁷ demonstrated for the first time that HT-WGS reaction follows the redox mechanism and CO is firstly oxidized by lattice surface oxygen and creates surface vacant sites for re-oxidation by H₂O. The authors propose the following redox reaction mechanism³⁷ on chromium-iron mixed oxide catalyst for the HT-WGS reaction:





However, the results in this study and the previous DFT calculations^{84,85} show CO firstly tends to adsorb on surface Fe_{oct} site. Moreover the above-mentioned TPSR study³⁷ showed that CO_2 formation obtained by the lattice oxygen and the O from H_2O molecule is required to oxidize surface to the original surface. Therefore, the mechanism may be modified as following:



Both iron and oxygen sites should be involved in the CO_2 formation step. Figure 5.12 shows the possible CO_2 formation step. C-O bond distance of the gas phase CO molecule was calculated as 1.142 Å, which is a close value to the experimental value of 1.128 Å and the previously found DFT result⁸⁶. Adsorbed CO molecule onto Fe_{oct} site has a longer C-O bond due to the back-donation of d-electron to the antibonding π^* orbital of CO ⁸⁶. CO may interact with the lattice oxygen (O_{lat}) for CO_2 formation. This step costs 0.5 eV. CO adsorbs onto O_{lat} like a bridge between O_{lat} and Fe_{oct} . The CO_2 molecule produced, as seen in Figure 5.12c, has a slightly longer C=O bond length (1.175 Å) than the experimental value of 1.16 Å that indicates the GGA91 calculation slightly overestimates this molecule's bond length. Figure 5.12 shows the possible adsorption of the CO and the optimization structure. In order to make a correct evaluation, CI-NEB calculations can provide the activation energy values of each step with the transition state calculations.

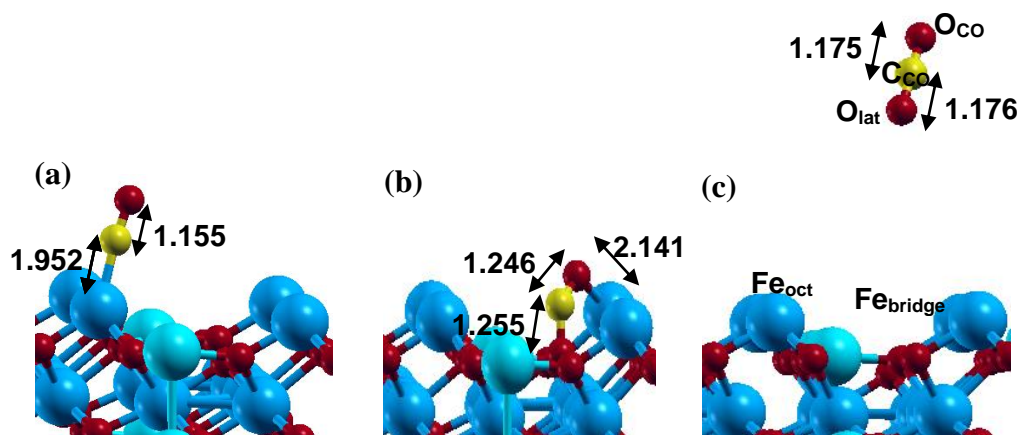


Figure 5.12. Optimized structures of CO₂ formation on the Fe_{oct2} terminated Fe₃O₄ (111) surface (a) CO adsorption on Fe_{oct} site (b) CO interaction with O_{lat} (c) CO₂ in the gas phase (Fe_{tet}: light blue, Fe_{oct}: blue, O: red, C: yellow)

Bader charge calculations were also done to analyze the charge transfer for the CO adsorption and CO₂ formation process. The Bader charge values of the selected atoms, Figure 5.12c) are tabulated in Table 5.5. C-Fe covalent bond formation occurs with the electron transfer from Fe atom to the C atom as 0.13 e⁻. Bridge like adsorption of CO onto the lattice oxygen occurs with the main electron transfer from C to the oxygen atoms. Oxygen vacancy on the surface makes the Fe_{bridge} atom less electro positive. The neutrality of the CO₂ proves that it is in the gas phase.

In the redox reaction mechanism, the next step is the oxidation of surface with H₂O. On the contrary to the clean surface, water tends to adsorb molecularly on the oxygen vacancy site with the adsorption energy of -1.8 eV. Figure 5.13 shows the water molecule adsorption and the dissociation step towards to surface Fe_{oct} site. Surface reconstruction occurs by the attraction between under-coordinated surface oxygen atoms and the H atoms of the water molecule. One possible dissociation site may be the lattice oxygen site. Another possibility is shown in Figure 5.13 for the dissociation of water molecule. Dissociation of H₂O by Fe_{oct} site costs 0.6 eV. Transferring of H atom onto the Fe_{tet} site with a huge energy of 2.6 eV indicates that dissociated H atoms are not present on the iron

sites at the same time. Surface Fe_{tet} site is unfavorable both for CO adsorption and for H_2O dissociation on the $\text{Fe}_{\text{oct}2}$ surface. One more step is the formation of H_2 molecule. H_2 may be formed by a direct hydrogen-hydrogen interaction. The H_2 molecule formed still stays on top of the Fe_{oct} atoms and desorption of the adsorbed H_2 molecule needs 0.2 eV to go to the gas phase. The gas phase H_2 molecule needs at least 1.2 eV energy to be formed from the molecularly adsorbed H_2O molecule onto the oxygen vacancy site. The evaluation would be more realistic after transition state calculations for the activation energy of each step.

Table 5.5. Bader charges of selected atoms on $\text{Fe}_{\text{oct}2}$ surfaces through CO_2 formation

Atom	$\text{CO}_{(\text{g})}$	CO adsorbed on Fe_{tet} (Figure 5.12a)	CO adsorbed on O_{lat} (Figure 5.12b)	$\text{CO}_{2(\text{g})}$ (Figure 5.12c)
Fe_{oct}	1.20	1.33	1.21	1.20
$\text{Fe}_{\text{bridge}}$	1.20	1.20	1.29	1.18
O_{lat}	-1.12	-1.12	-1.18	-1.20
O_{CO}	-1.06	-1.09	-1.17	-1.06
C_{CO}	1.06	0.89	1.53	2.13

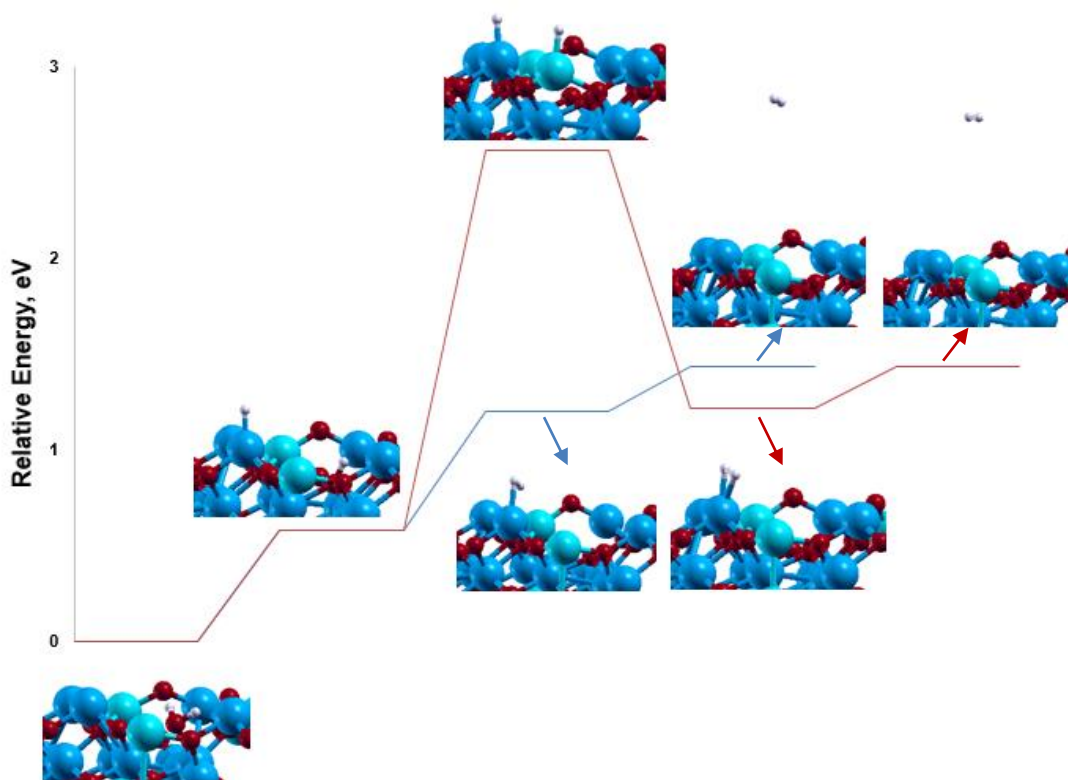


Figure 5.13. Possible pathways for H₂ formation on the Fe_{oct2} terminated Fe₃O₄ (111) surface (Fe_{tet}: light blue, Fe_{oct}: blue, O: red, H: white)

5.2.8. Cu₄ Cluster on Fe_{oct2} Termination

Conventional HT-WGS reaction catalysts (Fe₂O₃-Cr₂O₃ catalysts) contain about 80-90%(wt) of Fe₂O₃, 8-10% Cr₂O₃ and the balance being promoters and stabilizers like copper oxide⁵. Experimental studies^{24,29-31,33,38,39} show that CuO partially stabilizes the catalyst, significantly decreases the WGS activation energy (from 118±9 kJ mol⁻¹ to 75-80 kJ mol⁻¹)³⁹ and acts as a catalytic promoter. Cu is initially present as dispersed CuO and then reduces to metallic copper NPs during HT-WGS^{24,33,38}.

A three-dimensional tetrahedral structure for the 4-atom Cu cluster was proposed since there has been no report on the experimentally resolved sizes and structures of copper clusters⁹⁰. The percentage of CuO in the conventional CuO-Cr₂O₃-Fe₂O₃ catalysts is small (3% wt)⁵, and a DFT study of Cu₄ modified Fe_{tet1}

terminated $\text{Fe}_3\text{O}_4(111)$ structure shows that the CO and H_2O can be both stably adsorbed on this surface⁹¹.

The three-dimensional Cu_4 clusters in the gas phase and on the $\text{Fe}_{\text{Oct}2}$ terminated $\text{Fe}_3\text{O}_4(111)$ surface were optimized and illustrated in Figure 5.14. A slight elongation of the average Cu-Cu bonds in the gas phase of 2.38 Å on the adsorbed clusters indicates the mismatch between the tetrahedral Cu_4 clusters and $\text{Fe}_{\text{Oct}2}$ tetrahedral termination of $\text{Fe}_3\text{O}_4(111)$.

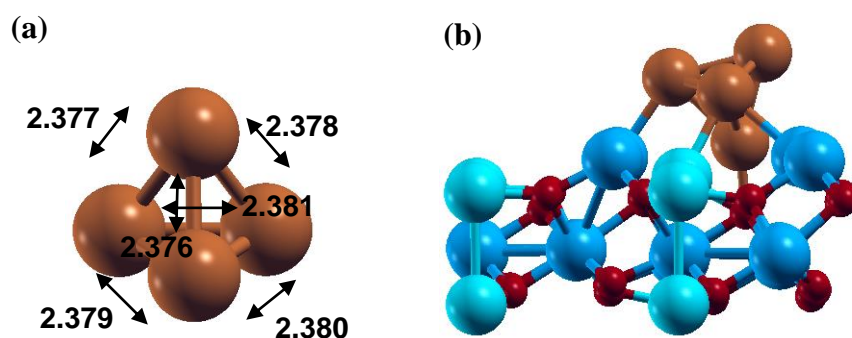


Figure 5.14. (a) Cu_4 cluster in the gas phase and (b) adsorbed Cu_4 cluster on the $\text{Fe}_{\text{Oct}2}$ terminated $\text{Fe}_3\text{O}_4(111)$ surface (Fe_{tet} : light blue, Fe_{Oct} : blue, O: red, Cu: brown)

5.2.8.1. CO Adsorption on $\text{Fe}_{\text{Oct}2}$ Termination with Cu_4 Cluster

The interaction CO molecule and the Cu-promoted surface was investigated on the copper promoter $\text{Fe}_{\text{Oct}2}$ surface in order to understand the positive effect of copper on the activity of WGS iron oxide based catalysts. CO adsorption on different sites was calculated and the optimized structures are shown in Figure 5.15.

The calculated adsorption energy for CO at the $\text{Fe}_{\text{Oct}2}$ site is -0.89 eV (-21.5 kcal/mol), which is very close to the calculated adsorption energy of CO at the Fe_{Oct} atom site on $\text{Fe}_{\text{Oct}2}$ surface (-0.96 eV or -22 kcal/mol). This indicates that presence of Cu on the structure does not affect the adsorption of CO on the Fe sites. The bridge type adsorption between Fe_{Oct} and Cu atom makes easier the adsorption of CO with very low adsorption energy (Figure 5.15b).

Another possible site for CO adsorption is the top of the Cu atoms. Figures 5.15c and 5.15d illustrate two different optimized structures with quite different adsorption energies. The most favorable site with the highest adsorption energy was exposed for the transfiguration of the tetrahedral structure by the CO adsorption. This may indicate that the structure of the copper cluster should be revised for other possible configurations.

On the other hand, the effect of the presence of the copper clusters on the CO adsorption is obvious with higher adsorption energies. Cu promotes the CO adsorption with new active sites. These new active sites can minimize the competition between the CO and H₂O molecules for the surface Fe_{oct} sites. The dissociation of H₂O molecule into the hydroxyl groups has a much stronger adsorption energy (-1.7 eV or -38 kcal/mol) as compared with that of CO (-0.89 eV or -22 kcal/mol). This may cause the desorption of CO⁸⁵ and negatively affect the redox reaction. Cu enhances the CO adsorption with the new active sites at and around the Cu cluster. These results are in line with the recent *in situ* HS-LEIS³⁸ study of HT-WGS reaction over CuO-Cr₂O₃-Fe₂O₃. The authors propose the FeO_x over layer on the metallic Cu nanoparticles during HT-WGS reaction to further provide a large number of such metal-oxide interfacial sites. The calculations prove that the interfacial sites are new active sites for CO adsorption with a stronger adsorption energy. Therefore, Cu is a chemical promoter by providing new active sites.

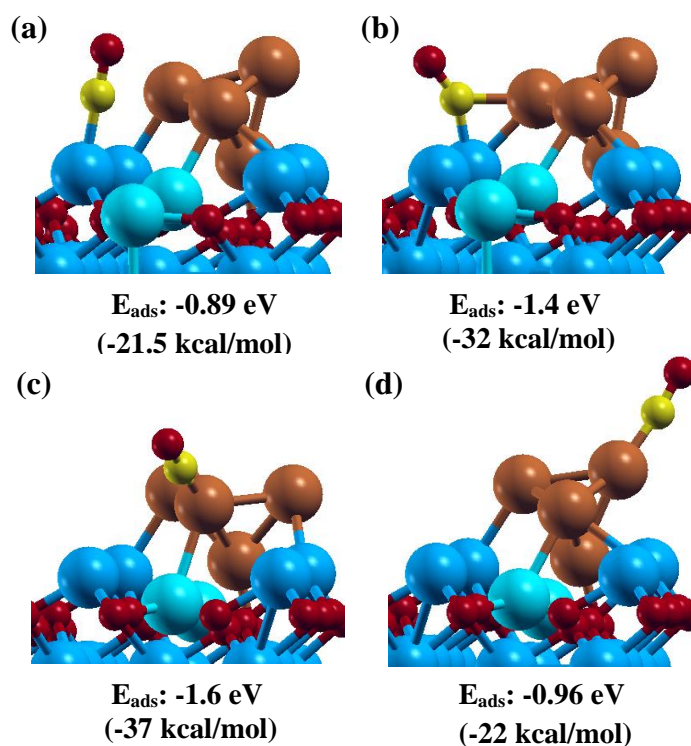


Figure 5.15. Optimized structure of CO adsorbed on the $\text{Fe}_{\text{oct}2}$ terminated Fe_3O_4 (111) surface with Cu_4 cluster at (a) Fe_{oct} site, (b) the bridge between $\text{Fe}_{\text{oct}}\text{-Cu}$, (c) Cu site bonded to Fe_{tet} , and (d) Cu site (Fe_{tet} : light blue, Fe_{oct} : blue, O: red, C: yellow, Cu: brown)

5.3. Conclusions

$\text{Fe}_{\text{oct}2}$ termination of Fe_3O_4 (111) and Cr atoms substituted Fe_3O_4 (111) slab surfaces as the HT-WGS catalysts are investigated by means of spin-polarized periodic DFT approach using the Vienna Ab-initio Simulation Package (VASP) with the projector-augmented wave (PAW) method. Ferrimagnetic Fe_3O_4 is successfully optimized with nearly the same magnetic moment for octahedral and tetrahedral sites and the results are in line with the experimental values. The $\text{Fe}_{\text{oct}2}$ termination reveals two Fe atom layers located at the octahedral site (topmost) and tetrahedral site over four oxygen atom layer is studied among the six Fe_3O_4 (111) terminations.

The DFT calculations indicate that Cr atoms prefer being below the FeO_6 sites. The oxygen atom located at the topmost layer is energetically favorable for

oxygen vacancy formation and the presence of Cr in the structure increases the oxygen vacancy formation energy. Water adsorption on both $\text{Fe}_{\text{oct}2}$ and Cr- $\text{Fe}_{\text{oct}2}$ surfaces is dissociative with the adsorption energy values of -1.7 and -1.6 eV, respectively. There is only a minor effect of Cr on dissociative adsorption of water. The adsorption energies for CO on both surfaces are the same value (-0.96 eV). Surface coverage by hydroxyl groups obstruct the adsorption of water by blocking the active Fe_{oct} sites. Copper promotion of $\text{Fe}_{\text{oct}2}$ structure with a Cu_4 cluster indicates that the new active sites on the copper-iron oxide interfacial enhance the CO adsorption with higher adsorption energies. Spin polarized DFT calculations prove that Cr does not have an effect as a chemical promoter and Cu is a chemical promoter with the new active sites.

CHAPTER 6

HIGH TEMPERATURE WATER-GAS SHIFT REACTION OVER Cr-FREE IRON OXIDE-BASED CATALYSTS

6.1. Abstract

The promotion of iron oxide and supported Cu/iron oxide was investigated with Zr, Nb, Ce and Al as potential replacements for the toxic Cr promoter currently being employed. The promoters were co-precipitated with iron oxide and Cu was subsequently impregnated onto the co-precipitated mixed oxides to form supported Cu/mixed oxide catalysts except Al promoter, which was prepared by co-precipitation of Cu-Al-Fe precursors. A suite of characterization analyses (XRD, Raman and HS-LEIS) of the calcined catalysts revealed that all the calcined catalysts contain the hematite bulk phase forming solid solutions ($\text{Fe}_{2-x}\text{M}_x\text{O}_3$). The supported Cu phase in the calcined catalysts is present below the surface as Cu^{2+} cations. Under WGS reaction conditions, the initial bulk iron oxide hematite phase transforms to the bulk magnetite (Fe_3O_4) phase, copper reduces and sinters to metallic nanoparticles, and nanoparticles of Nb_2O_5 and CeO_2 and most likely also ZrO_2 form. The Al promoter is not surface enriched and is concentrated in the bulk. The interplay between the promoters, copper and iron oxide affect the WGS catalytic performance of the different catalyst systems. These promoted catalysts without copper, however, did not perform better than the unpromoted iron oxide catalyst for the WGS reaction.

6.2. Results

6.2.1. Fe₂O₃

The iron oxide catalyst was prepared by precipitation of iron (III) nitrate nonahydrate (FeN₃O₉·9H₂O, Sigma-Aldrich, 99.99% trace metal basis) precursor. The XRD of the calcined unpromoted iron oxide catalyst was investigated under ambient conditions and the XRD diffractogram of fresh catalyst after calcination at 400 °C is presented in Figure 6.1. The bulk phase of the catalyst is identified as the crystalline α -Fe₂O₃ (hematite) phase¹³⁹ with the (110) peak appearing at $2\Theta = 35.63^\circ$ that is in agreement with the reported peak at 35.61° ¹³⁹.

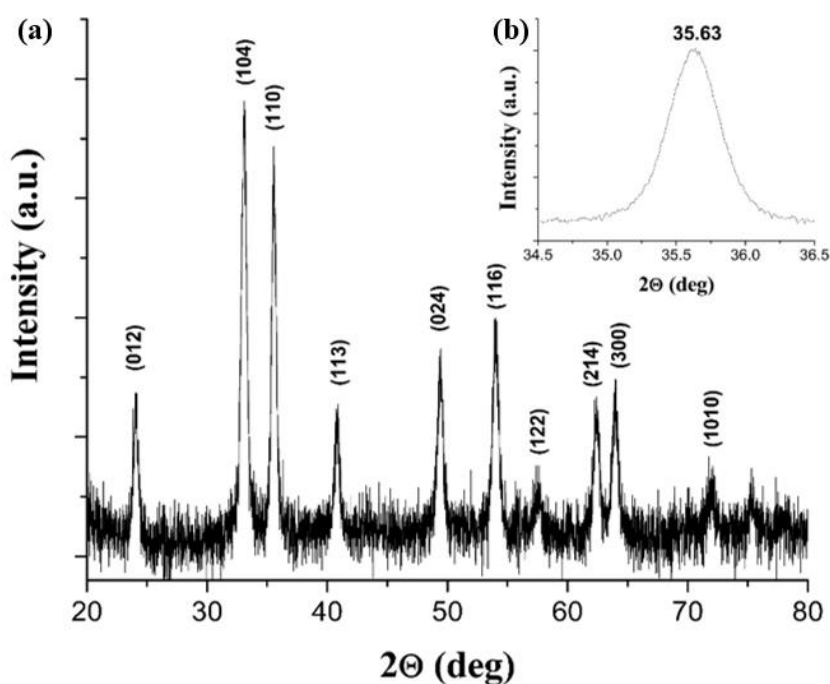


Figure 6.1. XRD diffractogram of unpromoted (α -Fe₂O₃) catalyst calcined at 400 °C and taken under ambient conditions as a function of 2Θ (a) full scan and (b) Fe₂O₃ (110) peak

The *in situ* Raman spectra of the α -Fe₂O₃ catalyst are shown in Figure 6.2 as a function of environmental conditions. Laser excitation at 442 nm (visible/violet) is selected in order to prevent any fluorescence problems caused by Fe⁺²¹⁴⁰. The Raman spectrum of the dehydrated catalyst exhibits the characteristic peaks of bulk α -Fe₂O₃ phase (hematite: 226, 245, 292, 411, 497, 612 cm⁻¹) with a minor amount of bulk γ -Fe₂O₃ (maghemite: 381, 486, 670, 718 cm⁻¹)¹²¹. Under the RWGS reaction conditions (Figure 6.2b), the bulk hematite phase reduces to the bulk Fe₃O₄ (magnetite) phase (306, 538, and 668 cm⁻¹)¹⁴¹. The bulk iron oxide phases are reversible and depend on the composition of the gas phase as shown in Figures A.1a and A.1b. The Fe₃O₄ phase is the bulk phase present under HT-WGS reaction conditions⁷. The partially reduced magnetite phase is sensitive to laser power, which may result in sample oxidation, and may be one of the reasons for different bands reported for magnetite in some published studies^{141,142}.

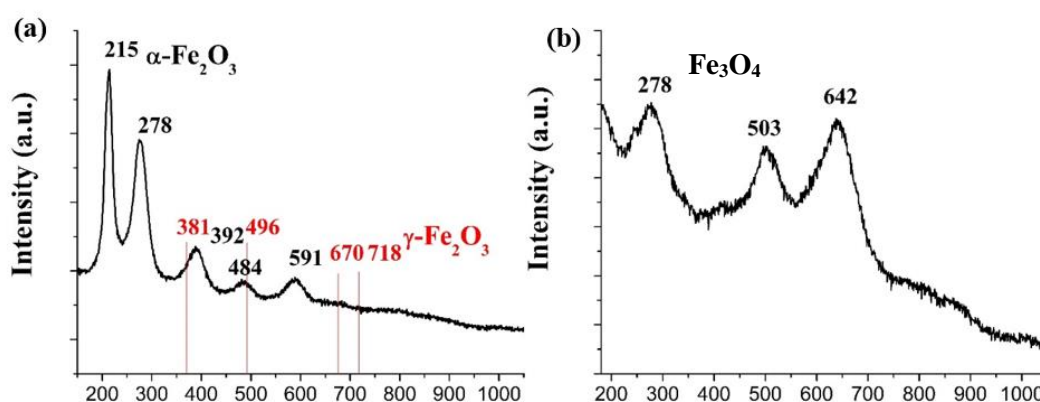


Figure 6.2. *In situ* Raman (442nm) spectra of calcined Fe₂O₃ catalyst at 400 °C: (a) dehydrated in 10% O₂/Ar, (b) RWGS reaction conditions (30 mL/min 5% CO₂/Ar and 15 mL/min 10% H₂/Ar)

The BET surface areas of the calcined and activated unpromoted iron oxide catalyst under the HT-WGS reaction as a function of temperature and reaction time, measured *in situ* without exposure to air, are listed in Table 6.1a.

The calcined Fe₂O₃ phase possessed a surface area of ~30 m²/g and the surface area decreased upon transformation to the Fe₃O₄ phase under HT-WGS with temperature and reaction time. After 1 hour of HT-WGS at 330 °C and 2-5 hours at 500°C the surface area decreased to ~13 and ~5-6 m²/g, respectively. The reaction temperature of 500°C is a much higher temperature than the normal operating HT-WGS reaction temperature of (350-450°C),⁸ but was selected to examine the thermostability of the unpromoted iron oxide catalyst, which will later be compared with the promoted catalysts.

Table 6.1. (a) BET surface area (dehydration: 10% O₂/Ar at 400 °C for 1 hr, WGS reaction: 10% CO/Ar (10 mL/min), He (30 mL/min), and water vapor (H₂O/CO ~ 1) and (b) steady-state catalytic activity via CO conversion (10% CO/Ar (10 mL/min), He (30 mL/min), and water vapor (H₂O/CO ~ 1)) of unpromoted iron oxide catalyst

(a)

Environmental Conditions	Surface Area (m ² /g)
calcined catalyst	30
330 °C 1hr WGS	13
500 °C 2hr WGS	6
500 °C 5hr WGS	5

(b)

Temperature (°C)	CO conversion (x10 ⁻⁶ mol/s.g)
330	1.9
350	3.1
370	4.8

The steady-state catalytic activity of the unpromoted iron oxide catalyst for the HT-WGS reaction is reported in Table 6.1b, and given as the conversion of CO.

6.2.2. Zr-promoted Iron Oxide Catalysts

The co-precipitated 8ZrFe catalyst was synthesized by the co-precipitation of zirconyl nitrate hydrate (ZrO(NO₃)₂.H₂O, Sigma-Aldrich, 99.99% trace metal basis) and iron (III) nitrate nonahydrate (FeN₃O₉.9H₂O,

Sigma-Aldrich, 99.99% trace metal basis) precursors. The supported 3Cu/8ZrFe catalyst was prepared by incipient wetness impregnation of aqueous copper (II) nitrate hemi(pentahydrate) ($\text{CuN}_2\text{O}_6 \cdot 2.5\text{H}_2\text{O}$, Sigma-Aldrich, 99.99% trace metal basis) Cu onto the co-precipitated 8ZrFe support followed by drying and calcination at 80 °C for 12 hours and 400 °C for 4 hours, respectively.

6.2.2.1. XRD

The diffractograms of calcined Fe_2O_3 , 8ZrFe, and supported 3Cu/8ZrFe catalysts under ambient conditions are presented both as full scans (Figure 6.3a) and the main Fe_2O_3 (110) peaks (Figure 6.3b). The Zr-promoted catalysts possess the crystalline $\alpha\text{-Fe}_2\text{O}_3$ (hematite) bulk phase¹³⁹. The X-ray diffraction patterns of the 8ZrFe and supported 3Cu/8ZrFe catalyst do not show the presence of any separate ZrO_2 , CuO_x or any new compounds between Cu-Zr-Fe.

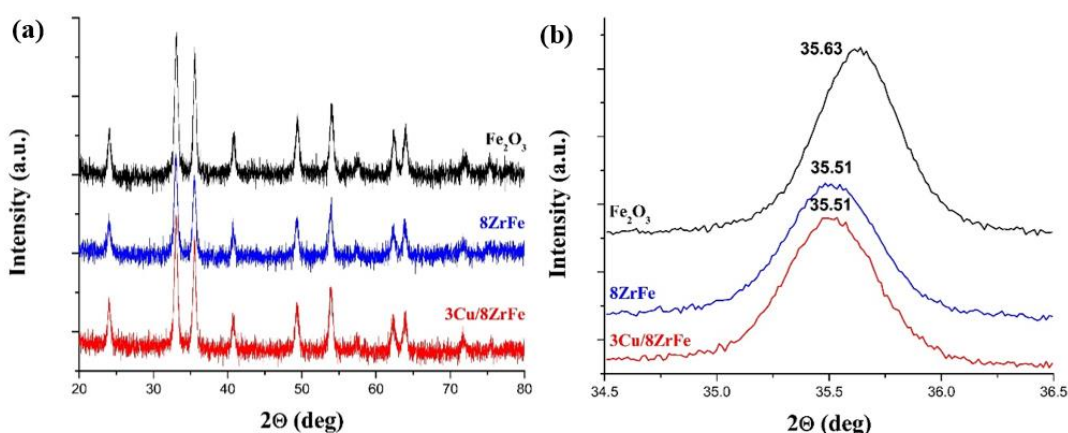


Figure 6.3. XRD diffractograms of Fe_2O_3 , 8ZrFe and supported 3Cu/8ZrFe catalysts calcined at 400 °C and taken under ambient conditions as a function of 2θ (a) full scan and (b) Fe_2O_3 (110) peak

The shift in the XRD Fe_2O_3 (110) peak position from 35.63 to 35.51° upon the addition of the Zr-promoter indicates that a $\text{Fe}_{2-x}\text{Zr}_x\text{O}_3$ solid solution has formed. The shift direction corresponds to the larger Zr^{4+} cation (72 pm)¹⁴³

than Fe^{3+} (64.5 pm)¹⁴³. An additional shift in the XRD Fe_2O_3 (110) peak was not observed after impregnation of Cu onto the $\text{Fe}_{2-x}\text{Zr}_x\text{O}_3$ support. This may be due to the lower amount of CuO (3 wt%) that would not produce a noticeable shift in the XRD or absence of the solid solution of $\text{Fe}_{2-x-y}\text{Zr}_x\text{Cu}_y\text{O}_3$.

6.2.2.2. *In situ* Raman Spectroscopy

The *in situ* Raman spectra of the 8ZrFe and supported 3Cu/8ZrFe catalysts are presented in Figure 6.4 as a function of environmental conditions. The calcined dehydrated 8ZrFe and supported Cu/8ZrFe catalysts exhibit the characteristic Raman bands of the hematite $\alpha\text{-Fe}_2\text{O}_3$ bulk phase¹²¹. A new weak and broad band is also present at 620-700 cm^{-1} and its intensity appears to increase for the calcined Cu impregnated catalyst (see Figure 6.4b). This new Raman band has been attributed to the formation of crystal disorder caused by the solid solution of $\text{Fe}_{2-x}\text{Zr}_x\text{O}_3$ with small crystal size¹⁴⁴. Discrete ZrO_2 nanoparticles (ZrO_2 : monoclinic (102, 179, 190, 222, 305, 334, 348, 381, 476, 500, 534, 556, 615, 637 cm^{-1})¹⁴⁵ and tetragonal (152, 265, 321, 468, 610, 646 cm^{-1})¹⁴⁶) are not detectable for the dehydrated 8ZrFe and supported Cu/ZrFe catalysts. In agreement with the XRD analysis, the zirconia phase is present as a solid solution of $\text{Fe}_{2-x}\text{Zr}_x\text{O}_3$. Zirconia may also be present as a surface ZrO_x overlayer or even small poorly ordered ZrO_2 nanoparticles (NPs) that can't be detected by XRD (<3 nm) or that don't give rise to detectable Raman bands against the strong Raman bands of the bulk hematite phase.

Under RWGS reaction conditions, the iron oxide bulk phase changes from hematite to magnetite with the characteristic Raman bands of Fe_3O_4 (compare with Figure 6.2 above)¹⁴¹. The Raman bands of ZrO_2 nanoparticles were not present under RWGS reaction conditions. Although *in situ* Raman analyses are able to provide information about both the bulk and the surface phases of the catalysts as a function of environmental conditions, vibrations from

the Cu promoter are not detected due to its lower concentration and small Raman cross-section relative to that of the bulk iron oxide phases³⁸.

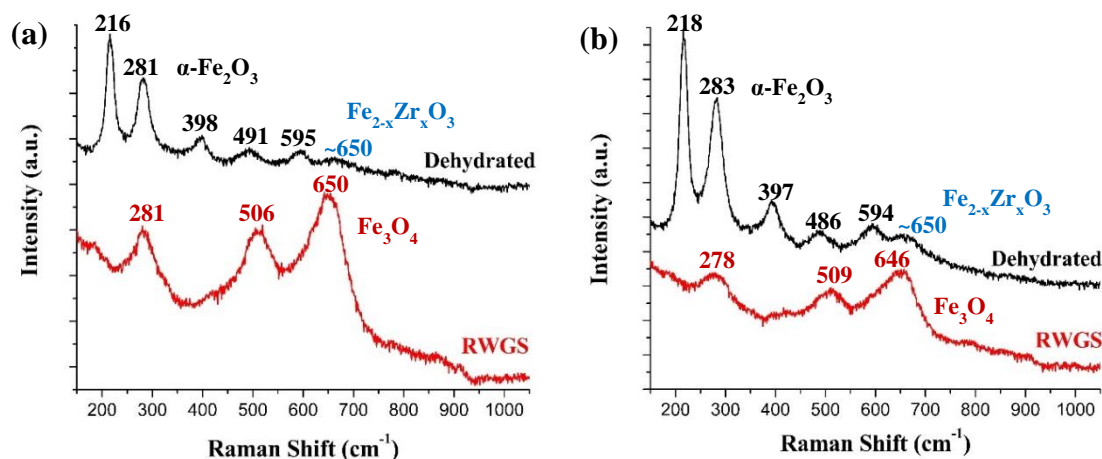


Figure 6.4. The *in situ* Raman spectra of (a) 8ZrFe and (b) supported 3Cu/8ZrFe catalysts under dehydration in 10% O₂/Ar and RWGS reaction conditions (30 mL/min 5% CO₂/Ar and 15 mL/min 10% H₂/Ar) at 400 °C

6.2.2.3. High Sensitivity Low-Energy Ion Scattering (HS-LEIS) Spectroscopy

HS-LEIS surface analysis of the 8ZrFe and supported 3Cu/8ZrFe catalysts were collected with both ⁴He⁺ and ²⁰Ne⁺ ion probes. The ⁴He⁺ (3 keV) HS-LEIS analysis was needed to collect data for lighter elements such as ¹⁶O and the ²⁰Ne⁺ (5 keV) HS-LEIS analysis to minimize signal overlap among the heavier elements ⁵⁶Fe, ^{63.5}Cu and ⁹¹Zr.

For the fresh calcined catalysts, the sample was dehydrated in static O₂ (~100 mbar) at 400 °C for 1 hr in a preparation chamber connected to the HS-LEIS spectrometer to remove any possible adsorbed organic impurities and adsorbed moisture. The catalyst sample was subsequently moved back to the preparation chamber and treated under the static RWGS reaction mixture (~100 mbar of pure CO₂/H₂ ~ 1 mixture) at 400 °C for 1 hr. After evacuation, the catalyst was again transferred to the HS-LEIS spectrometer for surface analysis.

In addition to the outermost elemental surface composition, depth profile compositions after the sputter-etching with 0.5 keV Ar⁺ were collected. The data for each catalyst sample were accumulated from ~20 individual spectra.

The BET surface area normalized HS-LEIS signals for Fe, Zr, and Cu as a function of sputtering depth for (a) calcined, dehydrated and (b) activated supported 3Cu/8ZrFe catalyst with 5keV Ne⁺ are plotted in Figure 6.5. For the calcined, dehydrated catalyst (Figure 6.5a), the HS-LEIS intensity of the Cu promoter initially increases and then decreases suggesting that Cu is being covered by another element. The corresponding HS-LEIS intensity for Zr is relatively constant with depth profiling indicating that Zr is equally distributed on outermost layer and below surface (~7 layers). The HS-LEIS intensity of the Fe signal increases with sputtering depth because of the preferential sputtering of O^{147,148}.

The BET surface area normalized HS-LEIS signals for Fe, Zr, and Cu as a function of sputtering depth for the activated supported 3Cu/8ZrFe catalyst are plotted in Figure 6.5b. The HS-LEIS intensity of the Cu promoter is dramatically diminished by either extensive sintering and/or a thick oxide overlayer (compare Figures 6.5a and 6.5b). It was previously demonstrated with in situ XPS measurements that sintered metallic Cu⁰ nanoparticles form during HT-WGS reaction conditions for Cu-Cr-Fe catalysts³⁸. The relatively constant intensity of the Cu signal with depth profile does not reveal any surface segregation as a two-dimensional dispersed phase. The HS-LEIS intensity of the Zr promoter for the activated catalyst is slightly higher relative to the calcined catalyst (compare Figures 6.5a and 6.5b) and weakly decreases with sputter depth reflecting its modest surface enrichment. The HS-LEIS intensity of Fe for the activated catalyst is much greater than that for the corresponding oxidized catalyst (compare Figures 6.5a and 6.5b) and suggests that most of the exposed sites for the activated catalysts are Fe. As mentioned above, the increase in signal intensity of Fe with sputtering depth is related to the preferential sputtering of O from iron oxide.

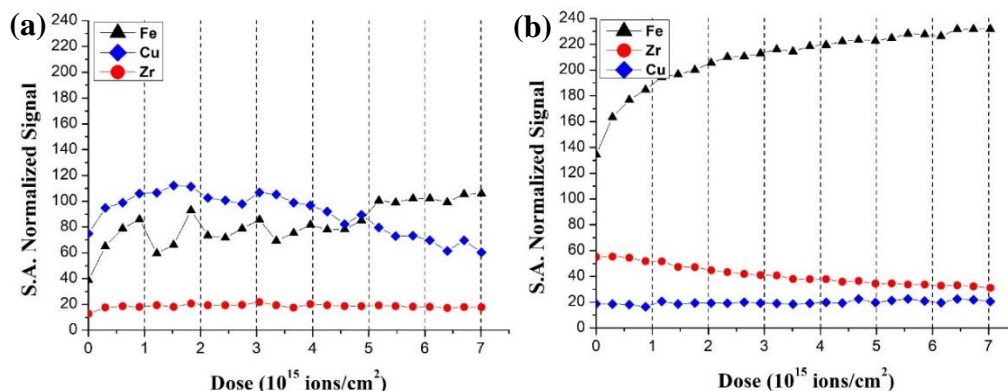


Figure 6.5. The BET surface area normalized HS-LEIS Fe, Zr, and Cu atomic density of both (a) dehydrated, calcined and (b) activated supported 3Cu/8ZrFe catalyst with the 5keV Ne⁺ dose as a function of sputtering depth. The vertical dashed lines indicate doses of $n(1 \times 10^{15} \text{ ions/cm}^2)$, with $n=1, 2, 3$, etc., that correspond to removal of a monolayer-equivalents from the catalyst¹⁴⁹

6.2.2.4. Flow BET Surface Area

The BET surface areas of 8ZrFe, supported 3Cu/8ZrFe and the un-doped Fe₂O₃ catalysts are given in Table 6.2. The surface areas for the calcined Zr-doped catalysts are slightly greater, ~1.5x, than the un-promoted Fe₂O₃ catalyst. The Zr-promoted catalysts possess greater thermostability during HT-WGS at 330 °C and 500 °C, ~2-3x greater, than the unpromoted Fe catalyst.

Table 6.2. BET surface areas of Fe, 8ZrFe and supported 3Cu/8ZrFe catalysts after dehydration: 10% O₂/Ar at 400 °C for 1 hr and WGS reaction: 10% CO/Ar (10 mL/min), He (30 mL/min), and water vapor (H₂O/CO ~ 1)

Environmental Conditions	Fe (m ² /g)	8ZrFe (m ² /g)	3Cu/8ZrFe (m ² /g)
calcined catalyst	30	45	43
330 °C 1hr WGS	13	27	27
500 °C 2hr WGS	6	20	13
500 °C 5hr WGS	5	10	10

6.2.2.5. CO-TPR

The redox properties of the activated Fe, 8CrFe, 3Cu/8CrFe, and 3Cu/8ZrFe catalysts were studied by CO-TPR. The normalized CO₂ MS signals with respect to the bed temperature are shown in Figure 6.6. The low temperature evolution of CO₂ is assigned to removal of oxygen from the surface region of the catalyst, and the high temperature CO₂ formation is associated with the reaction of oxygen from the bulk lattice³⁸. The strong peak starts after ~270 °C. 8CrFe catalyst retards the removal oxygen from the bulk lattice of the catalyst. The addition of copper decreases the low temperature peak to 147 °C and also accelerates the start of oxygen removal from the bulk lattice. Temperature regions can be divided into three peak regions for copper promoted supported iron oxide catalysts: 1st peak from surface Cu-FeO_x sites (most active), 2nd peak from surface MFeO_x sites (M: metal support, medium activity), 3rd peak from bulk MFeO_x lattice (low activity).

Supported 3Cu/8ZrFe catalyst decreases the 1st peak temperature to 133 °C; however the main peak is seen as a 2nd peak with the peak temperature of 181 °C. Moreover, this catalyst shows a lower temperature than iron oxide catalyst for lattice oxygen removal.

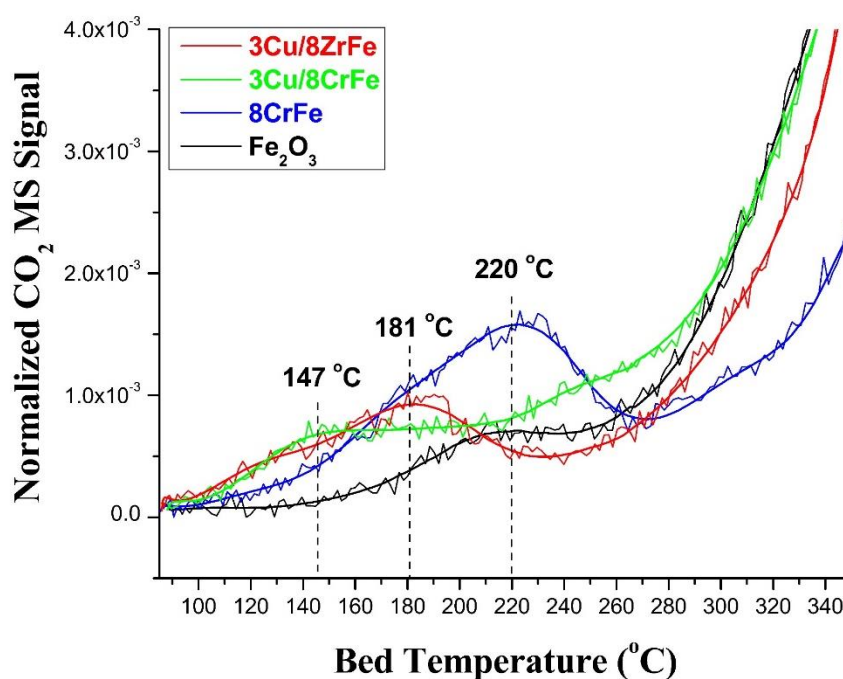


Figure 6.6. CO-TPR spectra of activated Fe, 8CrFe, 3Cu/8CrFe, and 3Cu/8ZrFe catalysts activated by WGS reaction conditions at 350 °C

6.2.2.6. Catalytic Activity during Steady-State HT-WGS Reaction

The catalytic activities of the Fe, 8ZrFe and supported 3Cu/8ZrFe catalysts for HT-WGS were studied as a function of reaction temperature after 1 hr of reaction, given in Table 6.3. The addition of Zr decreases the HT-WGS catalytic activity compared to the unpromoted iron oxide catalyst. The addition of Cu to 8ZrFe increases the catalytic activity, but the activity is still lower than that of the unpromoted Fe catalyst.

Table 6.3. Steady-state HT-WGS (10% CO/Ar (10 mL/min), He (30 mL/min), and water vapor (H₂O/CO ~ 1)) catalytic activities after 1 hr of reaction for Fe, 8ZrFe and supported 3Cu/8ZrFe catalysts based on CO conversion (x10⁻⁶ mol/s.g)

Temperature (°C)	Fe (x10 ⁻⁶ mol/s.g)	8ZrFe (x10 ⁻⁶ mol/s.g)	3Cu/8ZrFe (x10 ⁻⁶ mol/s.g)
330	1.9	0.9	1.3
350	3.1	1.4	2.0
370	4.8	2.1	3.1

6.2.2.7. Schematic Model

The schematic models for the calcined and activated supported 3Cu/8ZrFe catalyst are presented in Figure 6.7 and based on the above bulk and surface analyses. The models incorporate the (1) bulk Fe_{2-x}Zr_xO₃ solid solution and Fe_{3-x}Zr_xO₄ partial solid solution, (2) surface enrichment of Zr for the activated catalyst, dissolution of Cu²⁺ in the surface region of the calcined catalyst, (3) sintering of the metallic Cu nanoparticles during activation, (4) ZrO₄ NPs, which are not Raman active.



Figure 6.7. Schematic of the supported 3Cu/8ZrFe catalyst (a) calcined and (b) during HT-WGS

6.2.3 Nb-promoted Iron Oxide Catalysts

The co-precipitated 8NbFe catalyst was synthesized by the co-precipitation of niobium oxalate hexahydrate, which was firstly dissolved using 10% (w/v) oxalic acid solution^{104,105}, and iron (III) nitrate nonahydrate ($\text{FeN}_3\text{O}_9 \cdot 9\text{H}_2\text{O}$, Sigma-Aldrich, 99.99% trace metal basis) precursors. The supported 3Cu/8NbFe catalyst was prepared by incipient wetness impregnation of aqueous copper (II) nitrate hemi(pentahydrate) ($\text{CuN}_2\text{O}_6 \cdot 2.5\text{H}_2\text{O}$, Sigma-Aldrich, 99.99% trace metal basis) Cu onto the co-precipitated 8NbFe support followed by drying and calcination at 80 °C for 12 hours and 400 °C for 4 hours, respectively.

6.2.3.1. XRD

The diffractograms of fresh Fe_2O_3 , 8NbFe and supported 3Cu/8NbFe catalysts calcined at 400 °C are presented as full scans (Figure 6.8a) and only the main Fe_2O_3 (110) peaks (Figure 6.8b) as a function of 2θ . The Nb-promoted catalysts possess the crystalline $\alpha\text{-Fe}_2\text{O}_3$ (hematite) bulk phase¹³⁹ and do not show any separate Nb_2O_5 ¹⁵⁰, CuO_x or Cu-Nb-Fe compounds for the supported/8NbFe catalyst. Cu impregnated Nb-promoted Fe_2O_3 support. The ionic radius of Nb^{5+} is 64 pm¹⁴³ and the ionic radius of Fe^{3+} is 64.5 pm¹⁴³ and for a solid solution of $\text{Fe}_{2-x}\text{Nb}_x\text{O}_3$ the 2θ value would be expected to be shifted to slightly higher values. There is barely a shift in the XRD (110) peak for 8NbFe catalyst suggesting at best the possibility of only trace solubility of Nb in Fe_2O_3 as a solid solution. Within experimental error, the addition of Cu does not appear to perturb the Fe_2O_3 (110) peak of the supported Cu/8NbFe catalyst.

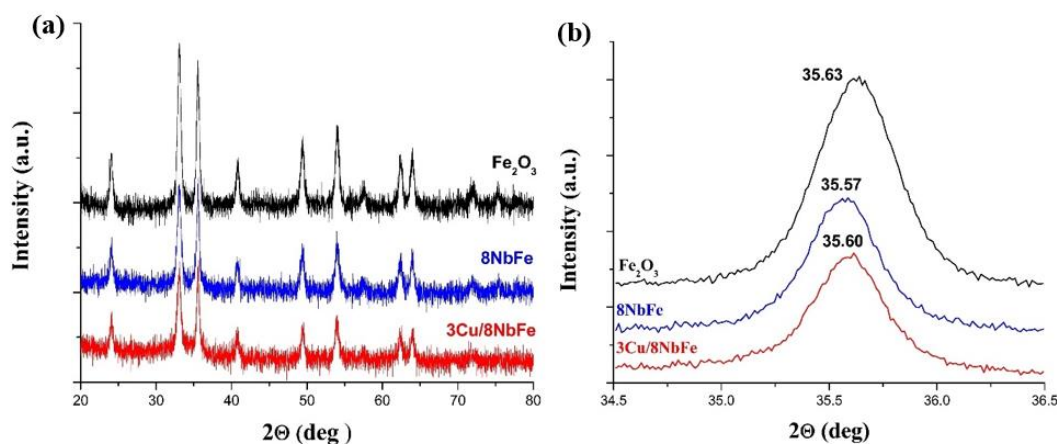


Figure 6.8. XRD diffractogram of calcined Fe₂O₃, 8NbFe and supported 3Cu/8NbFe catalysts calcined at 400 °C and taken under ambient conditions as a function of 2θ (a) full scan and (b) Fe₂O₃ (110) peak

6.2.3.2. *In situ* Raman Spectroscopy

The *in situ* Raman spectra of the 8NbFe and supported 3Cu/8NbFe catalysts are given in Figure 6.9 as a function of environmental conditions. The dehydrated calcined Nb-promoted and supported Cu/8NbFe catalysts exhibit the characteristic Raman peaks of the α -Fe₂O₃ bulk phase¹²¹. Raman bands from Nb₂O₅ nanoparticles¹⁵¹ are not present for the calcined catalysts. The intensity of the broad band at 620-700 cm⁻¹, which indicates the concentration of the promoters in the Fe₂O₃ bulk lattice³⁸, is lower for the 8NbFe and 3Cu/8NbFe catalysts than that for the 8ZrFe and 3Cu/8ZrFe catalysts, respectively. The presence of this band, however, demonstrates that Nb₂O₅ and Fe₂O₃ form a limited solid solution. The different cation charges of Nb and Fe would also be expected to introduce oxygen vacancies (e.g., substituting of 3Nb⁵⁺ for 5Fe³⁺).

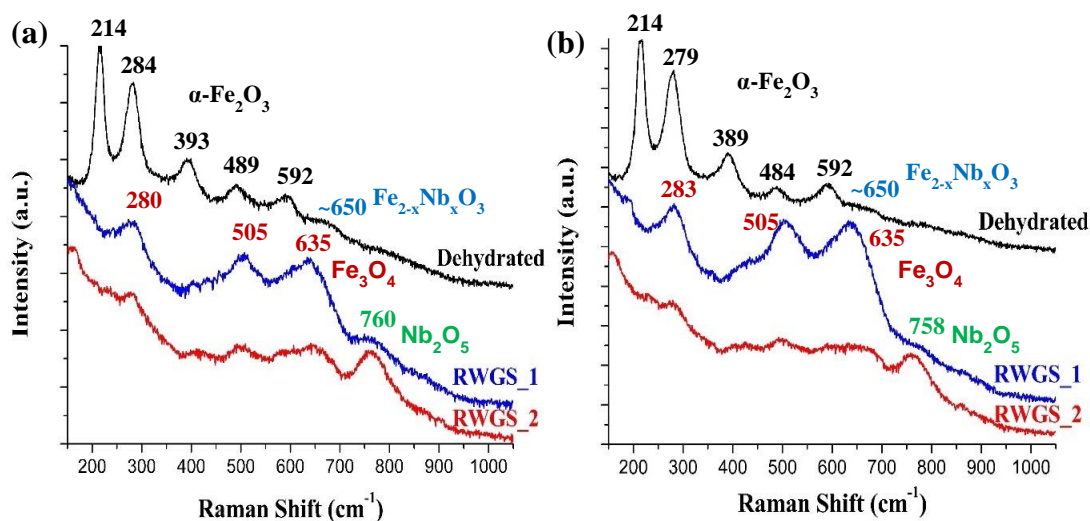


Figure 6.9. The *in situ* Raman spectra of (a) 8NbFe and (b) 3Cu/8NbFe catalysts under dehydration in 10% O₂/Ar and RWGS reaction conditions (30 mL/min 5% CO₂/Ar and 15 mL/min 10% H₂/Ar) at 400 °C. RWGS_1 and RWGS_2 signify spectral collection from different points.

Under RWGS reaction conditions, the bulk hematite phase transforms to the bulk magnetite phase with characteristic Raman bands of Fe₃O₄¹⁴¹. The Raman spectra of the activated catalysts also contain a new band at ~760 cm⁻¹ from Nb₂O₅ nanoparticles¹⁵¹. The Nb₂O₅ nanoparticles, however, are not uniformly dispersed on the magnetite support since the appearance of Nb₂O₅ Raman band varies from spot to spot (compare RWGS_1 and RWGS_2).

6.2.3.3. High Sensitivity Low-Energy Ion Scattering (HS-LEIS) Spectroscopy

For the dehydrated calcined supported 3Cu/8NbFe catalyst (Figure 6.10a), the intensity of the BET surface area normalized HS-LEIS Cu signal is much smaller than for the corresponding Zr-promoted catalyst and is related to the ~3x higher surface area of the supported Cu/8NbFe catalyst than Cu/8ZrFe catalyst (shown in Table 6.4 below). The intensity of the HS-LEIS Cu signal also varies somewhat with sputtering depth, initially increasing and then decreasing.

Such a depth profile trend is consistent with the Cu oxide being covered by another oxide. For example, the Cu^{2+} cations are situated below the iron oxide surface³⁸. As already indicated above, the intensity of the HS-LEIS Nb signal mildly decreases with sputtering depth indicating Nb_2O_5 nanoparticles and/or possibly the presence of surface NbO_x species. The intensity of the HS-LEIS Fe signal significantly increases with sputtering depth because of both removal of Nb/Cu from the surface region and preferential sputtering of the O from Fe_2O_3 ^{147,148}.

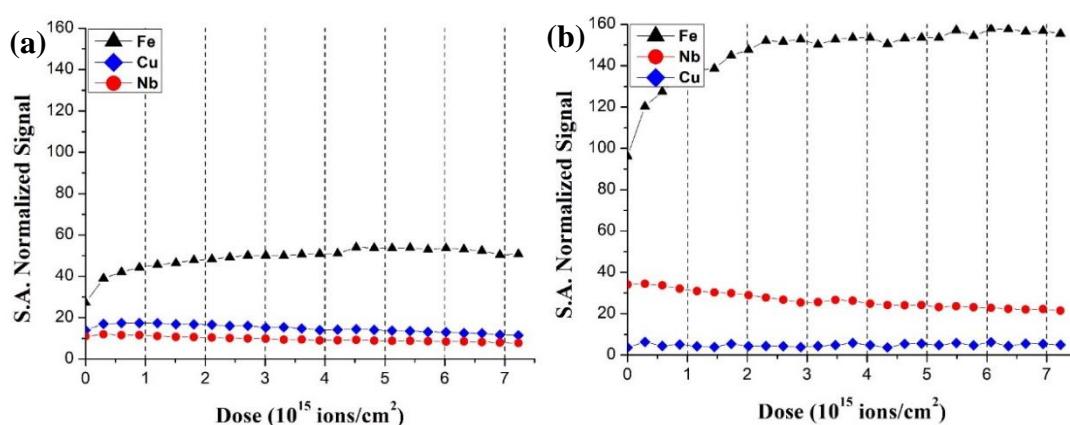


Figure 6.10. The BET surface area normalized HS-LEIS Fe, Nb, and Cu Atomic density of both (a) dehydrated, calcined and (b) activated supported 3Cu/8NbFe catalyst with the 5keV Ne^+ dose as a function of sputtering depth. The vertical dashed lines indicate doses of $n(1 \times 10^{15}$ ions/cm²), with $n=1,2,3$, etc., that correspond to removal of a monolayer-equivalents from the catalyst¹⁴⁹

For the activated supported 3Cu/8NbFe catalyst, the intensity of the HS-LEIS Nb signal is slightly greater than that for the calcined catalyst. Given that the surface area of the activated catalyst dramatically decreased by $\sim 2.5x$ (shown in Table 6.4 below), the surface NbO_x concentration did not proportionally increased by $\sim 2.5x$ and is consistent with sintering of the Nb_2O_5 phase as revealed by Raman spectroscopy (see Figure 6.8 above). The intensity of the HS-LEIS Cu signal dramatically decreased reflecting its sintering and possibly being covered by a thick oxide overlayer¹⁵². The intensity of the HS-LEIS Fe signal

significantly increases with sputtering depth because of both removal of Nb/Cu from the surface region and preferential sputtering of the O from Fe₂O₃^{147,148}.

6.2.3.4. Flow BET Surface Area

The BET surface areas for 8NbFe, supported 3Cu/8NbFe and unpromoted Fe₂O₃ catalysts are given in Table 6.4. The Nb promoter dramatically increases the surface areas of calcined 8NbFe and 3Cu/8NbFe compared to the unpromoted iron oxide by factors 3.5x and 4.5x, respectively. The increase in surface area is most likely related to the decrease in both particle size and pore diameter⁶⁴. The higher surface areas, however, are lost when the Nb-promoted catalysts are exposed to the WGS reaction. Nevertheless, the Nb-promoted catalysts still retain surface areas that are ~3x greater than the unpromoted iron oxide catalyst. Although Cu does decrease the surface area of the calcined Nb-promoted catalyst, it does not appear to influence the surface areas of the Nb-promoted catalysts during WGS. Overall, the Nb promoter does stabilize higher surface area catalysts.

Table 6.4. BET surface areas of Fe, 8NbFe and supported 3Cu/8NbFe catalysts (m²/g) after dehydration: 10% O₂/Ar at 400 °C for 1 hr and WGS reaction: 10% CO/Ar (10 mL/min), He (30 mL/min), and water vapor (H₂O/CO ~ 1)

Environmental Conditions	Fe (m²/g)	8NbFe (m²/g)	3Cu/8NbFe (m²/g)
Calcined catalyst	30	135	105
330 °C 1hr WGS	13	40	42
500 °C 2hr WGS	6	18	18
500 °C 5hr WGS	5	15	15

6.2.3.5. CO-TPR

The redox properties of the activated Fe, 8CrFe, 3Cu/8CrFe, and 3Cu/8NbFe catalysts were studied by CO-TPR. The normalized CO₂ MS signals with respect to the bed temperature are shown in Figure 6.11. Although there are tiny peaks at lower temperatures (114 °C and 166 °C), supported 3Cu/8NbFe catalyst gives similar temperature of the main peak as 8CrFe catalyst. The lattice oxygen removal temperature is also similar to CrFe catalyst.

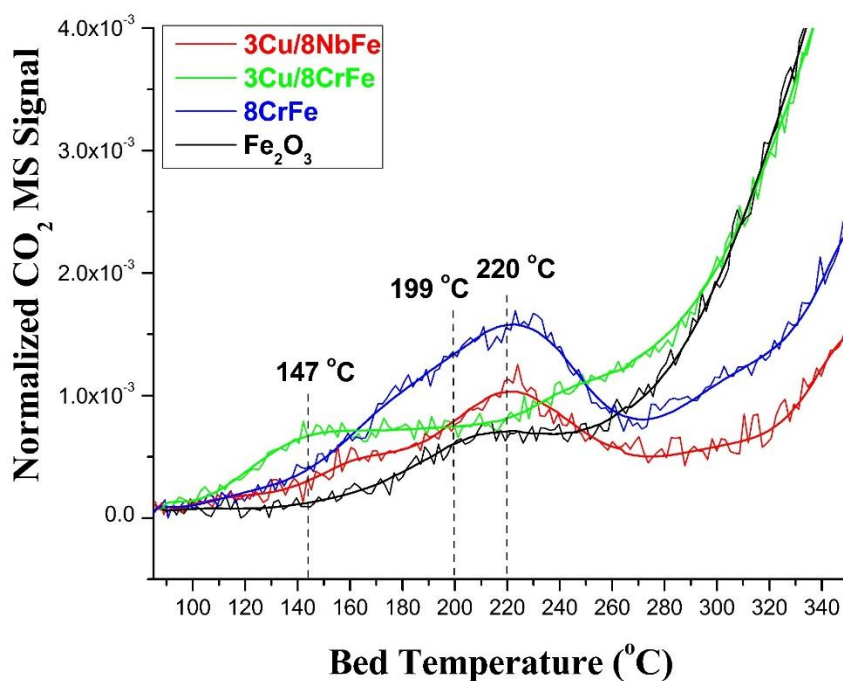


Figure 6.11. CO-TPR spectra of activated Fe, 8CrFe, 3Cu/8CrFe, and 3Cu/8NbFe catalysts activated by WGS reaction conditions at 350 °C

6.2.3.6. Catalytic Activity during Steady-State HT-WGS Reaction

The steady-state catalytic activities of the unpromoted and Nb-promoted catalysts are listed in Table 6.5. Although the Nb-promoted catalysts possess higher surface areas, they exhibit much lower catalytic activity. Even promotion

with Cu has only a minimal effect on the HT-WGS activity of the Nb-promoted catalysts.

Table 6.5. Steady-state HT-WGS (10% CO/Ar (10 mL/min), He (30 mL/min), and water vapor (H₂O/CO ~ 1)) catalytic activities after 1 hr of reaction for Fe, 8NbFe and supported 3Cu/8NbFe catalysts based on CO conversion ($\times 10^{-6}$ mol/s.g)

Temperature (°C)	Fe ($\times 10^{-6}$ mol/s.g)	8NbFe ($\times 10^{-6}$ mol/s.g _t)	3Cu/8NbFe ($\times 10^{-6}$ mol/s.g)
330	1.9	0.3	0.4
350	3.1	0.4	0.4
370	4.8	0.5	0.5

6.2.3.7. Schematic Model

The schematic model for the calcined and activated supported 3Cu/8NbFe catalyst is presented in Figure 6.12 and takes into consideration all the above findings. The models incorporate the (1) bulk Fe_{2-x}Nb_xO₃ and Fe_{3-x}Nb_xO₄ solid solutions that appear to be rather limited, (2) surface enrichment of Nb for the fresh and activated catalysts, (3) dissolution of Cu²⁺ in the surface region of the calcined catalyst, and (4) sintering of the metallic Cu nanoparticles during activation. It may also be possible that a portion of the metallic Cu NPs reside on the Nb₂O₅ NPs, but it is not possible to confirm this from the data at hand. It is also possible that the metallic Cu NPs are decorated with some surface FeO_x and NbO_x, but it is not possible to establish this because of the weak HS-LEIS signal from the metallic Cu NPs.



Figure 6.12. Schematic of the supported 3Cu/8NbFe catalyst (a) calcined and (b) during HT-WGS

6.2.4. Ce-promoted Iron Oxide Catalysts

The co-precipitated 8CeFe catalyst was synthesized by the co-precipitation of cerium nitrate ($\text{Ce}(\text{NO}_3)_3 \cdot 6\text{H}_2\text{O}$, Alfa Aesar 99.99%) and iron (III) nitrate nonahydrate ($\text{Fe}(\text{NO}_3)_3 \cdot 9\text{H}_2\text{O}$, Sigma-Aldrich, 99.99% trace metal basis) precursors. The supported 3Cu/8CeFe catalyst was prepared by incipient wetness impregnation of aqueous copper (II) nitrate hemi(pentahydrate) ($\text{Cu}(\text{NO}_3)_2 \cdot 2.5\text{H}_2\text{O}$, Sigma-Aldrich 99.99% trace metal basis) Cu onto the co-precipitated 8CeFe support followed by drying and calcination at 80 °C for 12 hours and 400 °C for 4 hours, respectively.

6.2.4.1. XRD

The diffractograms of calcined Fe_2O_3 , 8CeFe and supported 3Cu/8CeFe catalysts are presented as full scans and main Fe_2O_3 (110) peaks in Figures 6.13a and 6.13b, respectively. The bulk phase of the calcined Ce-promoted catalysts is the crystalline $\alpha\text{-Fe}_2\text{O}_3$ (hematite) bulk phase¹³⁹. The X-ray diffraction patterns of the calcined 8CeFe and supported 3Cu/8CeFe catalyst do not indicate any observable distinct nanoparticles of crystalline CeO_2 ¹⁵³, CuO_x or Cu-Ce-Fe compounds for the catalysts. The slight shift of the XRD Fe_2O_3 (110) peak for both the 8CeFe and supported 3Cu/8CeFe catalysts indicates that a solid solution has formed between Ce oxide and Fe_2O_3 , and is consistent with the larger ionic

radii of Ce^{4+} (87 pm)¹⁴³/ Ce^{3+} (101 pm)¹⁴³ than the ionic radius of Fe^{3+} (64.5 pm)¹⁴³. The addition of Cu to the Ce-promoted catalyst has no effect on the XRD Fe_2O_3 (110) peak position and is a consequence of either the small Cu concentration in the catalyst and/or the possible absence of a Cu-iron oxide solid solution.

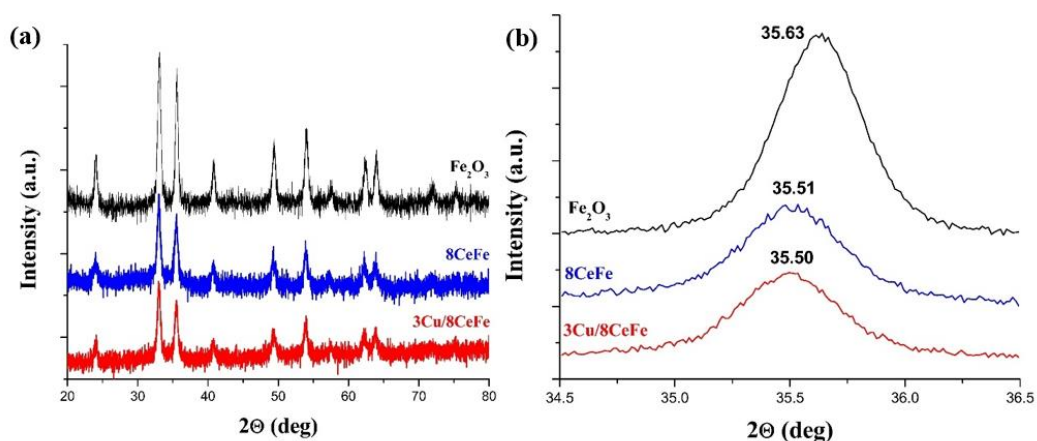


Figure 6.13. XRD diffractograms of Fe_2O_3 , 8CeFe and supported 3Cu/8CeFe catalysts calcined at 400 °C and taken under ambient conditions as a function of 2θ (a) full scan and (b) Fe_2O_3 (110) peak

6.2.4.2. *In situ* Raman Spectroscopy

The *in situ* Raman spectra of the 8CeFe and supported 3Cu/8CeFe catalysts are presented in Figure 6.14 as a function of environmental conditions. The Raman spectra of the calcined 8CeFe and supported 3Cu/8CeFe catalysts exhibit the characteristic Raman bands of the $\alpha\text{-Fe}_2\text{O}_3$ bulk phase¹²¹. The Raman band in the 620-700 cm^{-1} range indicates the formation of a $\text{Fe}_{2-x}\text{Ce}_x\text{O}_3$ solid solution for the calcined catalysts. Under the RWGS reaction conditions, the bulk iron oxide phase of the 8CeFe and supported 3Cu/8CeFe transforms to the magnetite bulk phase¹⁴¹. In the presence of Cu, a Raman band at $\sim 460 \text{ cm}^{-1}$ is also present that indicates CeO_2 ¹⁵⁴ nanoparticles are also formed during the RWGS reaction conditions.

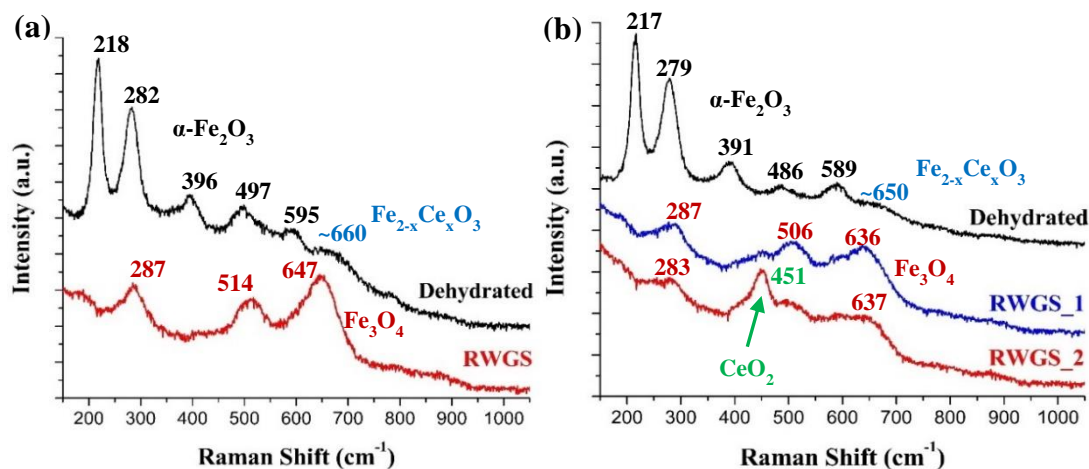


Figure 6.14. The *in situ* Raman spectra of (a) 8CeFe and (b) 3Cu/8CeFe catalysts under dehydration in 10% O₂/Ar and RWGS reaction conditions (30 mL/min 5% CO₂/Ar and 15 mL/min 10% H₂/Ar) at 400 °C. RWGS_1 and RWGS_2 signify spectral collection from different points.

6.2.4.3. High Sensitivity Low-Energy Ion Scattering (HS-LEIS)

Spectroscopy

The BET surface area normalized HS-LEIS analyses of calcined dehydrated and activated supported 3Cu/8CeFe catalyst are shown in Figures 6.15. For the dehydrated oxidized supported 3Cu/8CeFe catalyst (Figure 6.15a), the Ce promoter has the same concentration for both the outermost surface layer and the surface region (below the surface) revealing that Ce is not surface enriched and may be dissolved in the bulk Fe₂O₃ phase as a solid solution. The intensity of the HS-LEIS Cu signal is slightly higher towards the surface and mildly decreases with sputtering depth suggesting that Cu may be concentrated in the surface region. The HS-LEIS Fe signal intensity increases with initial sputter depth because of preferential sputtering of O^{147,148} and also possibly the enrichment of Cu in the surface region.

After activation of the supported 3Cu/8CeFe catalyst in the RWGS reaction environment at 400°C (Figure 6.15b), the intensity of the HS-LEIS Cu signal decreases slightly compared to the calcined catalyst. The comparable

intensity HS-LEIS Cu signals for the calcined and activated catalysts suggests, as well as the much stronger Cu signal for the activated Cu/8CeFe than the corresponding activated Zr- and Nb-promoted catalysts, indicates that Cu is not as sintered for the activated supported Cu/8CeFe catalyst in comparison to the other activated promoted catalysts. This interesting observation suggests that the cerium oxide promoter is maintaining Cu as a dispersed phase during HT-WGS. One possibility for this trend would be that Cu^{2+} cations are dispersed on the surface of the CeO_2 NPs. The decrease of the intensity of the HS-LEIS Cu signal with sputtering depth indicates that Cu is enriched towards the outer surface. The intensity of the HS-LEIS Ce signal, however, has significantly increased after the RWGS reaction treatment. This change in Ce concentration is related to both modest decrease of the catalyst surface area, ~36% (see surface areas in Table 6.8 below) and surface enrichment by formation of CeO_2 nanoparticles detected with Raman (see Figure 6.14). The intensity of the HS-LEIS Ce signal modestly decreases with sputtering that may be related to the slow depletion of the CeO_2 nanoparticles by the sputtering process and possibly the presence of a Ce-Fe-O solid solution. The intensity of the HS-LEIS Fe signal increases with sputtering depth because of Ce and Cu on the surface and the preferential sputtering of $\text{O}^{147,148}$.

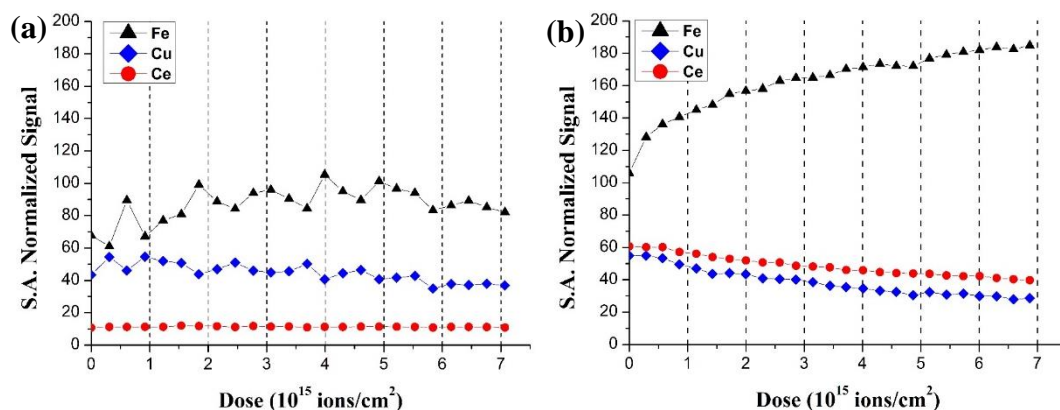


Figure 6.15. The BET surface area normalized HS-LEIS Fe, Ce, and Cu Atomic density of both (a) dehydrated, calcined and (b) activated supported 3Cu/8CeFe catalyst with the 5keV Ne⁺ dose. The vertical dashed lines indicate doses of $n(1 \times 10^{15} \text{ ions/cm}^2)$, with $n=1,2,3$, etc., that correspond to removal of a monolayer-equivalents from the catalyst¹⁴⁹

6.2.4.4. Flow BET Surface Area

The BET surface areas of the 8CeFe and supported 3Cu/8CeFe are given in Table 6.6. For the 8CeFe catalyst, the addition of the Ce promoter increases the surface area of the mixed oxide by ~2x after calcination and ~3-4x after WGS at 500°C. The addition of Cu to 8CeFe decreases the surface area of the mixed oxide by ~20%, but not the surface areas of the activated catalysts that are essentially the same.

Table 6.6. BET surface areas of Fe, 8CeFe and supported 3Cu/8CeFe catalysts (m^2/g) after dehydration: 10% O_2/Ar at 400 °C for 1 hr and WGS reaction: 10% CO/Ar (10 mL/min), He (30 mL/min), and water vapor ($\text{H}_2\text{O}/\text{CO} \sim 1$)

Environmental Conditions	Fe (m^2/g)	8CeFe (m^2/g)	3Cu/8CeFe (m^2/g)
Calcined catalyst	30	63	50
330 °C 1hr WGS	13	32	32
500 °C 2hr WGS	6	22	20
500 °C 5hr WGS	5	20	18

6.2.4.5. CO-TPR

The redox properties of the activated Fe, 8CrFe, 3Cu/8CrFe, and 3Cu/8CeFe catalysts were studied by CO-TPR. The normalized CO_2 MS signals with respect to the bed temperature are shown in Figure 6.16. Promoted 8Cu/3CeFe catalyst decreases the main peak temperature to 184 °C and it is higher than the peak temperature of 8CrFe catalyst.

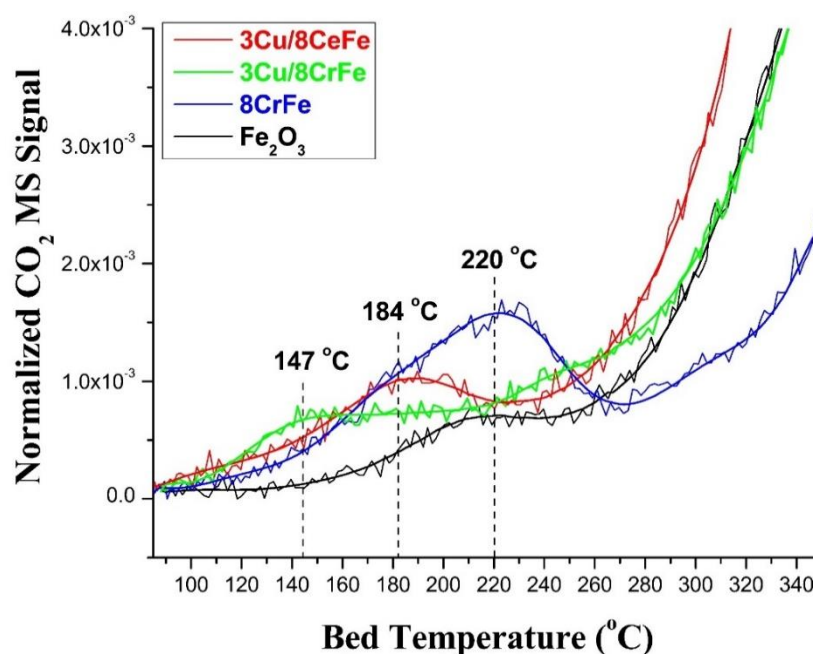


Figure 6.16. CO-TPR spectra of activated Fe, 8CrFe, 3Cu/8CrFe, and 3Cu/8CeFe catalysts activated by WGS reaction conditions at 350 °C

6.2.4.6. Catalytic Activity during Steady-State HT-WGS Reaction

The catalytic activity of the 8CeFe and supported 3Cu/8CeFe catalysts for the WGS reaction are given in Table 6.7. Their comparable surface areas indicates that any observable changes would not be related to changes in catalyst surface area. The addition of Ce, however, does not increase the WGS activity of 8CeFe catalyst compared to the unpromoted Fe catalyst. At best, the 8CeFe catalyst only approaches the activity of the unpromoted Fe catalyst. This indicates that Ce does not increase the redox activity of iron oxide³⁸. The supported 3Cu/8CeFe catalyst, however, was ~3-4x more active than the 8CeFe catalyst reflecting the promotional effect of Cu and Cu-Ce interactions.

Table 6.7. Steady-state HT-WGS (10% CO/Ar (10 mL/min), He (30 mL/min), and water vapor (H₂O/CO ~ 1)) catalytic activities after 1 hr of reaction for Fe, 8CeFe and supported 3Cu/8CeFe catalysts based on CO conversion (x10⁻⁶ mol/s.g)

Temperature (°C)	Fe (x10 ⁻⁶ mol/s.g)	8CeFe (x10 ⁻⁶ mol/s.g)	3Cu/8CeFe (x10 ⁻⁶ mol/s.g)
330	1.9	1.1	4.0
350	3.1	1.7	5.6
370	4.8	2.5	7.7

6.2.4.8. Schematic Model

The schematic model of the calcined and activated supported 3Cu/8CeFe catalyst is presented in Figure 6.17 and takes into consideration all the above findings. The models incorporate the (1) bulk Fe_{2-x}Ce_xO₃ and Fe_{3-x}Ce_xO₄ solid solutions, (2) surface enrichment of Ce for the activated catalyst, (3) dissolution of Cu²⁺ in the surface region of the calcined catalyst, and (4) sintering of the metallic Cu nanoparticles during activation, (5) formation of CeO₂ NPs on the activated catalyst.



Figure 6.17. Schematic of the 3Cu/8CeFe catalyst (a) calcined and (b) during HT-WGSR

6.2.5. Al-promoted Iron Oxide Catalysts

The 3Cu8AlFe catalyst was synthesized by the co-precipitation of aluminum nitrate nonahydrate ($\text{AlN}_3\text{O}_9 \cdot 9\text{H}_2\text{O}$, Sigma-Aldrich, 99.99% trace metal basis), iron (III) nitrate nonahydrate ($\text{FeN}_3\text{O}_9 \cdot 9\text{H}_2\text{O}$, Sigma-Aldrich, 99.99% trace metal basis) and copper (II) nitrate hemi(pentahydrate) ($\text{CuN}_2\text{O}_6 \cdot 2.5\text{H}_2\text{O}$, Sigma-Aldrich, 99.99% trace metal basis) precursors and followed by drying and calcination at 80 °C for 12 hours and 400 °C for 4 hours, respectively.

6.2.5.1. XRD

The diffractograms of calcined Fe_2O_3 and supported 3Cu8AlFe catalysts are presented as full scans and main Fe_2O_3 (110) peaks in Figures 6.18a and 6.18b, respectively. The bulk phase of the calcined Al-promoted catalysts is the crystalline $\alpha\text{-Fe}_2\text{O}_3$ (hematite) bulk phase¹³⁹. The X-ray diffraction pattern of 3Cu8AlFe catalyst do not show any separate Al_2O_3 ¹⁵⁵, CuO_x or any compounds between Cu-Al-Fe. The shift of the XRD Fe_2O_3 (110) peak for supported 3Cu8AlFe catalyst indicates that a solid solution has formed between Al oxide and Fe_2O_3 , and is consistent with the smaller ionic radii of Al^{3+} (53.5 pm)¹⁴³ than the ionic radius of Fe^{3+} (64.5 pm)¹⁴³.

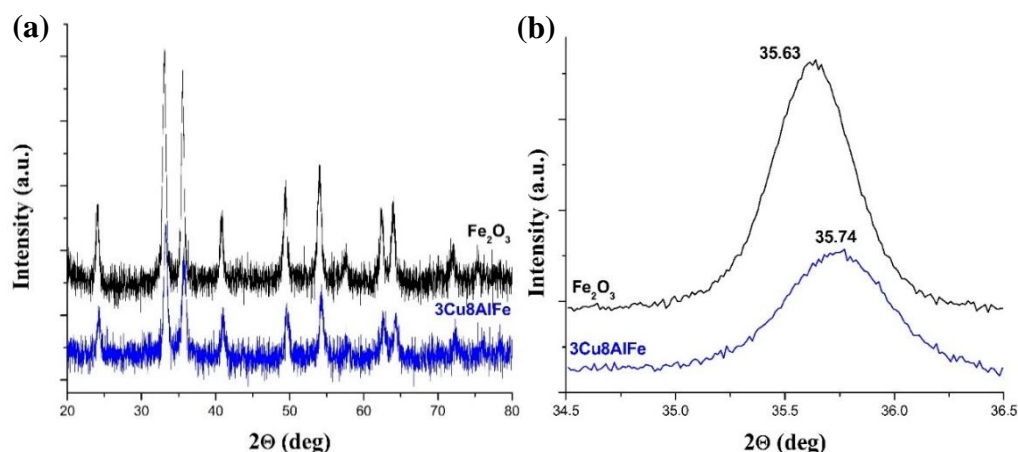


Figure 6.18. XRD diffractograms of Fe_2O_3 and supported 3Cu8AlFe catalysts calcined at 400 °C and taken under ambient conditions as a function of 2Θ (a) full scan and (b) Fe_2O_3 (110) peak

6.2.5.2. *In situ* Raman Spectroscopy

The *in situ* Raman spectra of the supported 3Cu8AlFe catalysts are presented in Figure 6.19 as a function of environmental conditions. The Raman spectra of the calcined supported 3Cu8AlFe catalysts exhibit the characteristic Raman bands of the $\alpha\text{-Fe}_2\text{O}_3$ bulk phase¹²¹. The Raman band in the 620-700 cm^{-1} range indicates the formation of a $\text{Fe}_{2-x}\text{Al}_x\text{O}_3$ solid solution for the calcined catalysts. Under the RWGS reaction conditions, the bulk iron oxide phase of the 3Cu8AlFe transforms to the magnetite bulk phase¹⁴¹.

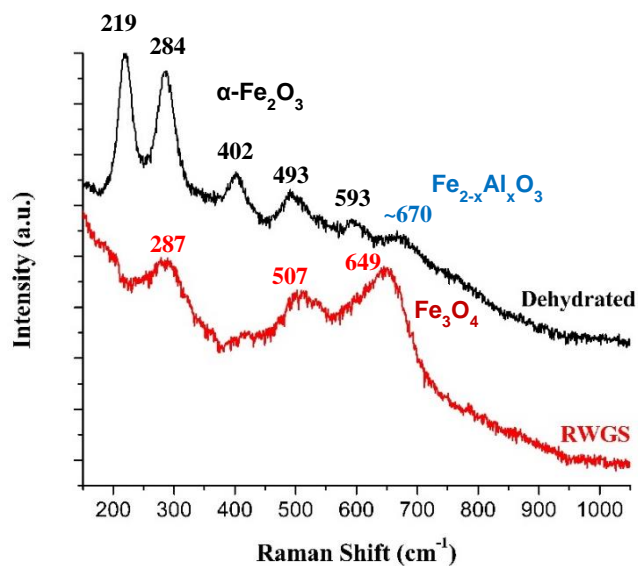


Figure 6.19. The *in situ* Raman spectra of 3Cu8AlFe catalysts under dehydration in 10% O₂/Ar and RWGS reaction conditions (30 mL/min 5%CO₂/Ar and 15 mL/min 10%H₂/Ar) at 400 °C

6.2.5.3. High Sensitivity Low-Energy Ion Scattering (HS-LEIS) Spectroscopy

For analysis of higher atomic weight elements (Fe, Cu, Zr, Nb, and Ce) ²⁰Ne⁺ HS-LEIS was employed. The ⁴He⁺ HS-LEIS was used to collect data for lighter elements (O, and Al). The BET surface area normalized HS-LEIS analyses of calcined dehydrated and activated supported 3Cu8AlFe catalyst are shown in Figure 6.20. The very weak HS-LEIS intensity of the Al signal is multiplied by 20 to better compare it with the other elements. For the dehydrated oxidized supported 3Cu8AlFe catalyst (Figure 6.20a), the concentration of the Al promoter is the same for both the outermost surface layer and the surface region (below the surface) revealing that Al is not surface enriched and is dissolved in the bulk lattice of the Fe₂O₃ phase as a solid solution. The intensity of the HS-LEIS Cu signal is also constant through the surface region and slightly increases in the first nm of depth profiling reflecting the absence of surface

segregation. The HS-LEIS Fe signal intensity increases with initial sputter depth because of preferential sputtering of O^{147,148}.

After activation of the supported 3Cu8AlFe catalyst in the RWGS reaction environment at 400°C (Figure 6.20b), the intensity of the HS-LEIS Al signal has significantly increased and because of the decrease in the catalyst surface area, ~49% (see surface areas in Table 6.11 below). The comparable intensity of the HS-LEIS Al signal with depth profiling indicates the absence of surface segregation of Al, and comparable similar concentrations on the outermost surface and below the surface. The mild increase of HS-LEIS intensity of the Cu signal with depth profiling suggest that the metallic Cu nanoparticles may be decorated with FeO_x. The intensity of the HS-LEIS Fe signal increases with sputtering depth because of preferential sputtering of O^{147,148}.

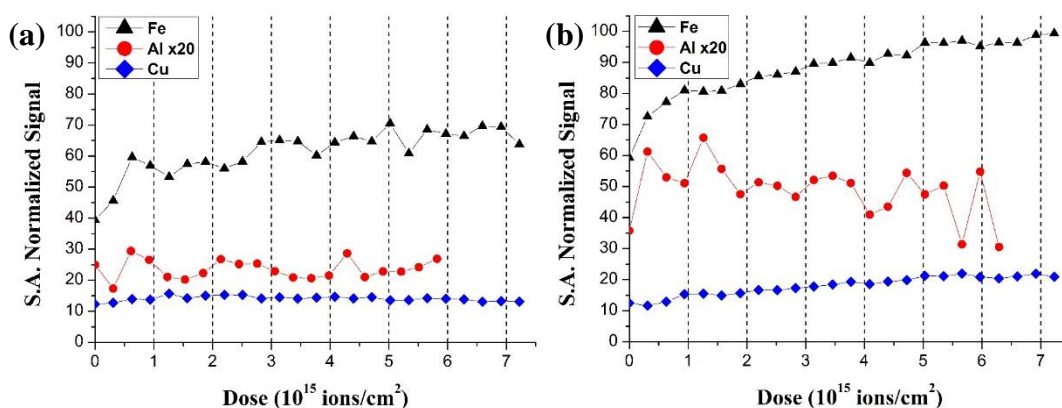


Figure 6.20. The BET surface area normalized HS-LEIS Fe, Al, and Cu Atomic density of both (a) dehydrated, calcined and (b) activated supported 3Cu8AlFe catalyst with the 3keV He⁺ and 5keV Ne⁺ dose. The vertical dashed lines indicate doses of $n(1 \times 10^{15} \text{ ions/cm}^2)$, with $n=1,2,3$, etc., that correspond to removal of a monolayer-equivalents from the catalyst¹⁴⁹

6.2.5.4. Flow BET Surface Area

The BET surface areas of the supported 3Cu8AlFe is given in Table 6.8. The addition of the Al promoter increases the surface area of the mixed oxide by

~3x after calcination and ~3.4x and ~4.5x after WGS at 330°C and 500 °C, respectively.

Table 6.8. BET surface areas of Fe and supported 3Cu8AlFe catalysts (m²/g) after dehydration: 10% O₂/Ar at 400 °C for 1 hr and WGS reaction: 10% CO/Ar (10 mL/min), He (30 mL/min), and water vapor (H₂O/CO ~ 1)

Environmental Conditions	Fe (m²/g)	3Cu8AlFe (m²/g)
Calcined catalyst	30	86
330 °C 1hr WGS	13	44
500 °C 2hr WGS	6	25
500 °C 5hr WGS	5	23

6.2.5.5. CO-TPR

The redox properties of the activated Fe, 8CrFe, 3Cu/8CrFe, and 3Cu8AlFe catalysts were studied by CO-TPR. The normalized CO₂ MS signals with respect to the bed temperature are shown in Figure 6.21. Promoted 8Cu3AlFe catalyst gives similar even lower low peak temperature as 134 °C and main peak is the 1st peak indicating that the interaction of Cu-Al-Fe system, especially copper interaction with the oxides, facilitates surface reduction.

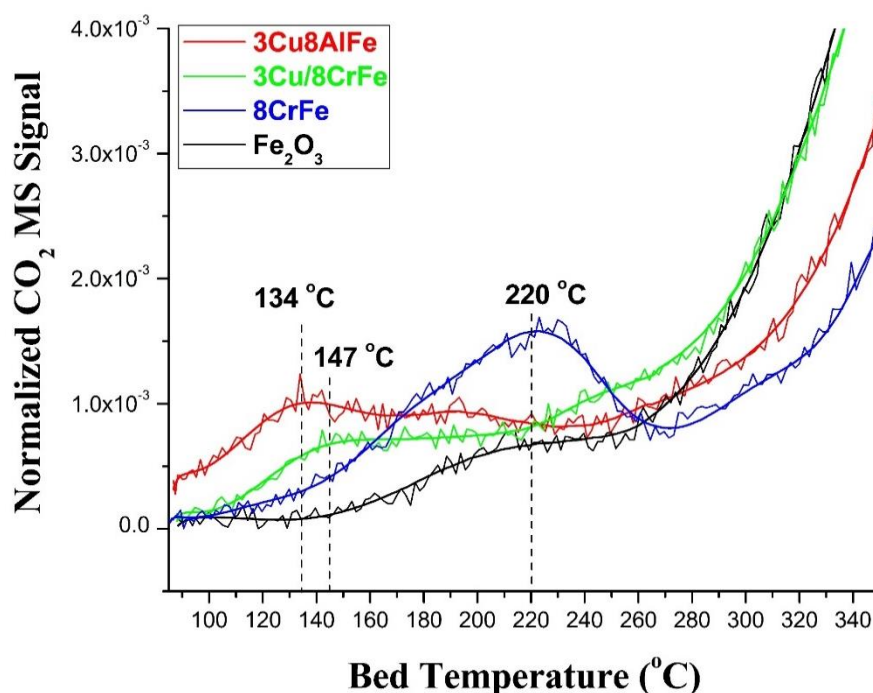


Figure 6.21. CO-TPR spectra of activated Fe, 8CrFe, 3Cu/8CrFe, and 3Cu8AlFe catalysts activated by WGS reaction conditions at 350 °C

6.2.5.6. Catalytic Activity during Steady-State HT-WGS Reaction

The catalytic activity of the supported 3Cu8AlFe catalysts for the WGS reaction are given in Table 6.9. Cu-Al promoters enhance the catalytic activity. The supported 3Cu8AlFe catalyst was ~2x more active than the iron oxide catalyst reflecting the promotional effect of Cu and Cu-Al-Fe interactions.

Table 6.9. Steady-state HT-WGS (10% CO/Ar (10 mL/min), He (30 mL/min), and water vapor (H₂O/CO ~ 1)) catalytic activities after 1 hr of reaction for Fe and supported 3Cu8AlFe catalysts based on CO conversion (x10⁻⁶ mol/s.g)

Temperature (°C)	Fe (x10 ⁻⁶ mol/s.g)	3Cu8AlFe (x10 ⁻⁶ mol/s.g)
330	1.9	4.4
350	3.1	6.3
370	4.8	8.8

6.2.5.7. Schematic Model

The schematic model of the calcined and activated supported 3Cu/8CeFe catalyst is presented in Figure 6.22 and takes into consideration all the above findings. The models incorporate the (1) bulk $\text{Fe}_{2-x}\text{Al}_x\text{O}_3$ and $\text{Fe}_{3-x}\text{Al}_x\text{O}_4$ solid solutions, (2) dissolution of Cu^{2+} in the surface region of the calcined catalyst, and (3) sintering of the metallic Cu nanoparticles during activation, (5) decoration of Cu NPs by FeO_x particles on the activated catalyst.

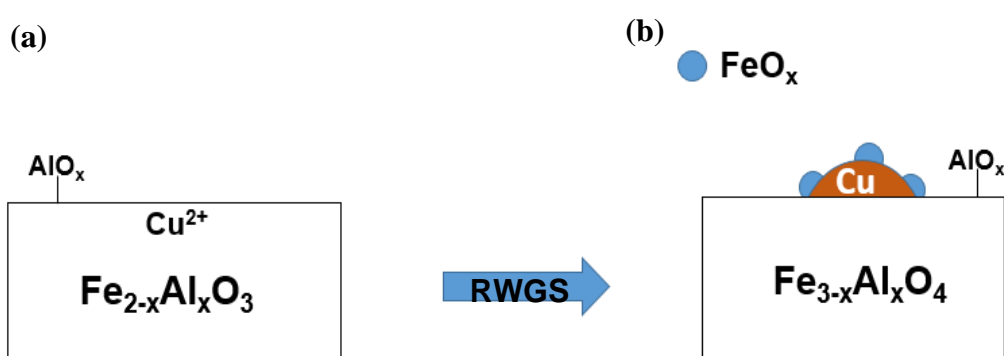


Figure 6.22. Schematic of the 3Cu8AlFe catalyst (a) calcined and (b) during HT-WGSR

6.3. Discussion

6.3.1. Bulk Structure

a. Calcined catalysts. Both the promoted and unpromoted calcined catalysts always possess the bulk hematite (Fe_2O_3) phase. In the presence of promoters during the co-precipitation synthesis, the promoters may also become incorporated into the bulk hematite phase by forming solid solutions of $\text{Fe}_{2-x}\text{M}_x\text{O}_3$. The commercially used Cr promoter forms a $\text{Fe}_{2-x}\text{Cr}_x\text{O}_3$ solid solution with Cr^{3+} in octahedral sites²⁴. The Zr, Ce and Al promoters also form $\text{Fe}_{2-x}\text{Zr}_x\text{O}_3$,

Fe_{2-x}Ce_xO₃ and Fe_{2-x}Al_xO₃ solid solutions as reflected by the shifts in the XRD Fe₂O₃ (110) peak and the Raman band at 620-700 cm⁻¹. The XRD shifts follow the trends with their ionic radii: Al³⁺ (35.74, 0.535 Å) > Fe₂O₃ (35.63°, 64.5 pm) > Zr⁴⁺ (35.51°, 72 pm) = Ce³⁺ (35.51°, 101 pm Å). The addition of the Nb promoter does not result in a shift in the XRD Fe₂O₃ (110) peak, but there is a weak Raman band at 620-700 cm⁻¹ suggesting that there is minimal formation of a Fe_{2-x}Nb_xO₃ solid solution. Although the addition of the Cu promoter does not give rise to a shift in the XRD Fe₂O₃ (110) peak because of its low concentration or presence as CuO nanoparticles, the HS-LEIS analysis reveals that Cu is present below the Fe₂O₃ surface as a Fe_{2-x}Cu_xO₃ solid solution. The schematic models of the calcined promoted catalysts are depicted above in Figures 6.7a, 6.12a, 6.17a and 6.22a.

b. Activated catalysts. During the WGS and RWGS reaction environments at 400 °C, the bulk hematite (Fe₂O₃) phase transforms to the bulk magnetite (Fe₃O₄) phase. In the presence of promoters during HT-WGS, the promoters may also become incorporated into the bulk magnetite phase by forming solid solutions of Fe_{3-x}M_xO₄. The commercially used Cr promoter forms a Fe_{3-x}Cr_xO₄ solid solution with Cr³⁺ in octahedral sites²⁴. In the absence of *in situ* XRD diffractograms during the HT-WGS reaction, the formation of bulk magnetite (Fe_{3-x}M_xO₄ with M=Zr, Nb, Ce and Al) solid solutions could not be confirmed by XRD. The persistence of the HS-LEIS signals for the promoters with extensive sputtering, ~6 monolayer equivalent, strongly suggests that the promoters were at least partially dissolved in the magnetite lattice. The constant HS-LEIS signal for Al promoter indicates dissolving in the magnetite lattice. The *in situ* Raman spectra measurements during HT-WGS revealed that Nb₂O₅ and CeO₂ nanoparticles formed during HT-WGS that could reflect the lower solubility of these promoters in the slightly reduced magnetite phase with generally much lower surface areas. Nanoparticles of ZrO₂ may also be present, but previous studies have shown that ZrO₂ nanoparticles are difficult to detect with Raman spectroscopy. No Al₂O₃ nanoparticles were observed. The

significant decrease in the HS-LEIS Cu signal after activation in HT-WGS reflects the reduction and sintering of the initially dispersed Cu^{+2} to metallic Cu^0 nanoparticles. The formation of metallic Cu^0 nanoparticles during HT-WGS was previously confirmed with *in situ* XPS and EXAFS measurements³⁸. The schematic models of the activated promoted catalysts are depicted above in Figures 6.7b, 6.12b, 6.17b and 6.22b.

6.3.2. Surface Structure

a. Calcined catalysts. The relatively constant intensity of the HS-LEIS signals for the promoters Zr, Ce and Al with sputtering depth of the dehydrated calcined catalysts reveals that the promoters were not surface enriched and were equally concentrated throughout the surface region, ~6 monolayer-equivalent, of the hematite phase. For the conventional Cu/CrFe HT-WGS catalyst, the calcined catalyst is surface enriched with dioxo $(\text{O}=\text{O})_2\text{Cr}^{6+}\text{O}_4$ species that are readily detectable with Raman spectroscopy because of the Cr=O bond that give rise to a strong Raman band³⁸. The absence of Zr=O and Ce=O oxo bonds for these promoters with low oxidation states, unfortunately, precludes their detection with Raman spectroscopy. Although Nb=O oxo bonds can be present for niobium oxides ($\sim 900\text{-}980\text{ cm}^{-1}$ ¹⁵¹) their Raman bands tend to be very weak and would be overshadowed by the stronger Raman bands of hematite. For the calcined supported 3Cu/8ZrFe catalyst, the Cu promoter is present as Cu^{2+} and concentrated in the 2-3nm region below the surface of hematite, which is reflected by the initial increase and subsequent decrease of the intensity of the HS-LEIS Cu signal with sputtering depth. For the Nb-, Ce- and Al-promoted catalyst, however, the Cu^{2+} may be more concentrated into the bulk since the maximum in the HS-LEIS intensity of the Cu signal is not as pronounced with sputter etching.

b. Activated catalysts. The conventional Cu-Cr-Fe HT-WGS catalyst contains the Cr^{3+} in the bulk $\text{Fe}_{3-x}\text{Cr}_x\text{O}_4$ bulk lattice with a lower concentration

at the outermost surface than the bulk region. The Zr, Nb and Ce promoters, however, are slightly surface enriched for the activated catalysts and the intensity of their HS-LEIS signals slightly decrease with sputter etching. This depth profile trend suggests that the Zr, Nb and Ce promoters are more concentrated at the surface than the magnetite bulk lattice. Furthermore, Raman spectroscopy revealed that even Nb₂O₅ and CeO₂ nanoparticles are present on the magnetite support. The same may also hold for ZrO₂ nanoparticles, but cannot be confirmed because of the absence of Raman detectable bands for ZrO₂ nanoparticles. On the other hand, Al promoter is not surface enriched and located on both outermost layer and in the bulk lattice. Upon activation for the Zr- and Nb-promoted catalysts, the HS-LEIS intensity of the Cu signal significantly decreased and then slightly further decreases with sputter etching due to formation of sintered metallic Cu⁰ nanoparticles. For the Ce-promoted catalyst, however, the HS-LEIS intensity of the Cu signal did not decrease upon activation suggesting that sintering of metallic Cu⁰ may have not taken place. It is possible that CeO₂ stabilizes surface Cu²⁺ species since this would maintain similar surface concentration of Cu in the activated catalyst that would be similar to that for the calcined catalyst.

6.3.3. Catalyst Thermostability

For the conventional Cu-Cr-Fe HT-WGS catalyst, Cr enhances the catalyst thermostability by nearly doubling the surface area. In the present study, the Zr, Nb, Ce and Al promoters also enhanced the surface area of calcined and activated copper promoted 8MFe catalysts.

6.3.4 Catalytic Activity – Structure Relationship

The activated Zr-, Nb-, Ce- and Al-promoted Fe_{3-x}M_xO₃ magnetite catalysts possessed comparable or slightly higher surface areas than the

unpromoted catalyst, but did not exhibit higher HT-WGS activity than unpromoted Fe_3O_4 and $\text{Fe}_{3-x}\text{Cr}_x\text{O}_4$ catalysts. Even with the addition of the Cu promoter, the Zr- and Nb-promoted catalysts were not more active than unpromoted Fe_3O_4 and $\text{Fe}_{3-x}\text{Cr}_x\text{O}_4$ catalysts. The Cu-promoted $\text{Fe}_{3-x}\text{Ce}_x\text{O}_4$ catalyst, however, possessed a high activity for the HT-WGS reaction. For the conventional $\text{Fe}_{3-x}\text{Cr}_x\text{O}_4$ catalyst, promotion of Cu is induced by the formation of surface FeO_x islands on the metallic Cu nanoparticles³⁸. The low activity of the Zr- and Nb-promoted Cu/ Fe_3O_4 catalysts may be related to the retardation of the migration of FeO_x to the surface of the metallic Cu nanoparticles. The Ce-promoted Cu/8CeFe catalyst, however maintained the Cu highly dispersed, either by being present on the metallic Cu surface or as dispersed Cu on the CeO_2 nanoparticles. Such a strong metal-support interaction may account for the enhanced performance of the Ce-promoted Cu/8CeFe catalyst for HT-WGS. Although Al-promoter provides FeO_x nanoparticles decoration on the metallic copper, it does not provide better activity.

6.4. Conclusions

A series of iron oxide-based catalysts for HT-WGS were prepared by a two-step co-precipitation-impregnation method. The Zr, Nb, Ce and Al promoters were initially co-precipitated with iron oxide to form mixed oxides that were subsequently impregnated with copper. Differing promotion mechanisms were found for the activated promoted catalysts. The Zr promoter was equally distributed on the catalyst outermost surface and the surface region (~6 monolayers-equivalent) and did not interfere with the promotion of the metallic Cu nanoparticles by surface FeO_x . The Nb promoter was concentrated on the catalyst outermost surface and also prevented the migration of surface FeO_x to the metallic Cu nanoparticles. The Ce promoter was concentrated on the catalyst outermost surface and enhanced migration of FeO_x to CeO_2 and metallic Cu nanoparticles. Al promoter is not surface enriched, increases BET but does

not enhance redox properties. The interplay between the promoters (Zr, Nb, Ce, Al), copper and iron oxide affected the catalytic performance for the WGS reaction; however, none of these promoters enhanced catalytic performance for the WGS reaction even with copper.

CHAPTER 7

CONCLUSIONS AND RECOMMENDATIONS

7.1. Conclusions

The Water-gas shift catalytic reaction is an important intermediate step for hydrogen enrichment. The HT-WGS reaction was initially commercially practiced with the unsupported Cr-Fe mixed oxide catalyst in industry. A Cu promoter was subsequently added to increase the catalytic activity. The fundamental understanding of these Fe oxide-based catalysts can be advanced by combining theoretical and *in situ/operando* spectroscopy experimental studies. The new insights should guide the rational design of Cr-free Fe oxide-based HT-WGS catalysts.

In the computational part of this study, the bulk and (111) surface of Fe_3O_4 with FeO_4 and FeO_6 terminations were successfully optimized by spin-polarized DFT calculations using VASP. The DFT calculations indicate that surface FeO_6 is catalytic active site and Cr atoms prefer locating below the FeO_6 sites, in agreement with the LEIS surface analysis of Cr-Fe oxide catalyst activated under the WGS reaction conditions. The oxygen atom located at the topmost layer is energetically favorable for oxygen vacancy formation and the presence of Cr in the structure increases the energy for oxygen vacancy formation, which is in line with kinetic measurements. Water adsorption on both $\text{Fe}_{\text{oct}2}$ and Cr- $\text{Fe}_{\text{oct}2}$ surfaces is dissociative with the adsorption energy values of -159 and -154 kJ/mol, respectively, indicating that there is only a minor effect of Cr on molecular adsorption of water. The adsorption energy for CO on both surfaces are nearly same (the activation barrier for CO_2 formation on the $\text{Fe}_{\text{oct}2}$ site is 48 kJ/mol). The new active sites formed at the copper-iron oxide interface of the supported Cu_4 cluster on the $\text{Fe}_{\text{oct}2}$ surface enhance the CO adsorption with higher adsorption energies. Spin polarized DFT calculations conclude that Cr

does not have an effect as a chemical promoter and that only Cu acts as a chemical promoter because of the formation of the new interfacial active sites.

In the experimental part of this study, Zr-, Ce-, Al- and Nb-promoted Fe oxide-based, Cr-free, catalysts were successfully synthesized by the co-precipitation method and subsequently impregnated with Cu. The prepared catalysts were investigated with XRD, *in situ* Raman spectroscopy, HS-LEIS, and flow BET bulk and surface characterization techniques. Differing promotion mechanisms were found for the activated promoted catalysts. The Zr promoter was equally distributed on the catalyst outermost surface and the surface region (~6 monolayers-equivalent) and did not interfere with the promotion of the metallic Cu nanoparticles by surface FeO_x. The Nb promoter was concentrated on the catalyst outermost surface and also prevented the migration of the promoting surface FeO_x to the metallic Cu nanoparticles. The Ce promoter was concentrated on the catalyst outermost surface and enhanced migration of FeO_x to metallic Cu and CeO₂ nanoparticles, especially the latter. The Al promoter incorporates into the structure for activated catalyst, increases surface area; however it does not enhance redox properties. The interplay between the promoters (Zr, Nb, Al and Ce), metallic copper nanoparticles and iron oxide affected the catalytic performance for the WGS reaction. None of these promoters, however, enhanced the catalytic performance for the WGS reaction in comparison to the promoter-free supported copper/iron oxide catalyst.

7.2. Recommendations

From the theoretical perspective:

Adsorption of the reactants and the redox mechanism of the HT-WGS catalyst models should be elaborated on by the climbing image nudged elastic band calculations (CI-NEB) to determine the transition states and the activation barriers of each reaction step especially the rate-determining-step.

The promotion of metallic copper may be investigated with larger copper clusters over the surface, which would possess greater metallic property. This may provide a good comparison between the metallic copper and the copper-iron oxide interference.

From the experiment perspective:

The activated surfaces of catalysts under the WGS reaction conditions should be investigated by additional *in situ/operando* characterization technique. Fully understanding of the catalyst system of the proposed promoters for Cr-free iron oxide-based catalysts would be possible by the combination of several additional analyses. *In situ/operando* XANES and NAP-XPS are two valuable characterization techniques for examining the nature of the catalytic active sites and the redox characteristics of the catalyst bulk and surface components during HT-WGS reaction.

In order to evaluate the activity of a catalyst, one can determine the turnover frequency (TOF), which indicates the production of the desired product on an active site per unit time. The $C^{16}O_2/C^{18}O_2$ isotopic switch experiments can be performed to determine the number of catalytic active sites (Ns: active surface O^*) and the specific reaction rates (turnover frequency = reaction rate/Ns). Evaluation of the activity of the catalysts would be meaningful by comparing the TOF values since TOF is independent of catalyst surface area and reflects the intrinsic activity of the active sites. By this way, the promotion mechanism of the proposed elements would be better understood.

The designed new catalyst for HT-WGS reaction by stabilizing BET with Al promoter and increasing redox by post-impregnation of redox Ce promoter.

The importance of further decreasing the CO content in syngas and producing additional H_2 will maintain the research interest in the water-gas shift reaction system for years to come. The rational design of the Cr-free iron oxide-based catalysts for HT-WGS reaction is critical for the environmental and health concerns and this study may contribute to this goal.

REFERENCES

1. Smith RJB, Loganathan M, Shantha MS. A Review of the water gas shift reaction kinetics. *Int J Chem React Eng*. 2010;8(1):1-32. doi:10.2202/1542-6580.2238.
2. Gradisher L, Dutcher B, Fan M. Catalytic hydrogen production from fossil fuels via the water gas shift reaction. *Appl Energy*. 2015;139:335-349. doi:10.1016/j.apenergy.2014.10.080.
3. Levalley TL, Richard AR, Fan M. The progress in water gas shift and steam reforming hydrogen production technologies - A review. *Int J Hydrogen Energy*. 2014;39(30):16983-17000. doi:10.1016/j.ijhydene.2014.08.041.
4. Ladebeck JR, Wagner JP. Catalyst development for water-gas shift. *Handb Fuel Cells – Fundam Technol Appl*. 2003;3:190-201. doi:10.1002/9780470974001.f302017.
5. Ratnasamy C, Wagner JP. Water gas shift catalysis. *Catal Rev Sci Eng*. 2009;51(3):325-440. doi:10.1080/01614940903048661.
6. Mendes D, Mendes A, Madeira LM, Iulianelli A, Sousa JM, Basile A. The water-gas shift reaction: from conventional catalytic systems to Pd-based membrane reactors - a review. *Asia-Pacific J Chem Eng*. 2010;5:111-137. doi:10.1002/apj.364.
7. Rhodes C, Hutchings GJ, Ward AM. Water-gas shift reaction: finding the mechanistic boundary. *Catal Today*. 1995;23(1):43-58. doi:10.1016/0920-5861(94)00135-O.
8. Lee DW, Lee MS, Lee JY, et al. The review of Cr-free Fe-based catalysts for high-temperature water-gas shift reactions. *Catal Today*. 2013;210:2-9. doi:10.1016/j.cattod.2012.12.012.
9. De Araújo GC, do Carmo Rangel M. An environmental friendly dopant for the high-temperature shift catalysts. *Catal Today*. 2000;62(2-3):201-207. doi:10.1016/S0920-5861(00)00421-1.
10. Babita K, Sridhar S, Raghavan KV. Membrane reactors for fuel cell quality hydrogen through WGS - Review of their status, challenges and opportunities. *Int J Hydrogen Energy*. 2011;36(11):6671-6688. doi:10.1016/j.ijhydene.2011.02.107.
11. Reddy GK, Smirniotis PG. *Water Gas Shift Reaction Research Developments and Applications*. Elsevier B.V.; 2015.
12. Zhu M, Wachs IE. Iron-based catalysts for the high-temperature water-

- gas shift (HT-WGS) reaction: a review. *ACS Catal.* 2016;6(2):722-732. doi:10.1021/acscatal.5b02594.
13. Fishtik I, Datta R. A UBI–QEP microkinetic model for the water–gas shift reaction on Cu(111). *Surf Sci.* 2002;512:229-254. doi:10.1016/S0039-6028(02)01689-8.
 14. Armstrong EF, Hilditch TP. A study of catalytic actions at solid surfaces. IV. The interaction of carbon monoxide and steam as conditioned by iron oxide and by copper. *Proc R Soc A Math Phys Eng Sci.* 1920;97:265-273.
 15. Meshkani F, Rezaei M. Hydrogen production by high temperature water gas shift reaction over highly active and stable chromium free Fe-Al-Ni catalysts. *Int J Hydrogen Energy.* 2015;40(34):10867-10875. doi:10.1016/j.ijhydene.2015.06.170.
 16. Natesakhawat S, Wang X, Zhang L, Ozkan US. Development of chromium-free iron-based catalysts for high-temperature water-gas shift reaction. *J Mol Catal A Chem.* 2006;260(1-2):82-94. doi:10.1016/j.molcata.2006.07.013.
 17. Lee JY, Lee D-W, Lee K-Y, Wang Y. Cr-free Fe-based metal oxide catalysts for high temperature water gas shift reaction of fuel processor using LPG. *Catal Today.* 2009;146(1-2):260-264. doi:10.1016/j.cattod.2009.01.041.
 18. Wang H, Wang G, Wang X, Bai J. Hydrogen production by redox of cation-modified iron oxide. *J Phys Chem C.* 2008;112(14):5679-5688. doi:10.1021/jp711587m.
 19. Tabakova T, Manzoli M, Paneva D, Boccuzzi F, Idakiev V, Mitov I. CO-free hydrogen production over Au/CeO₂-Fe₂O₃ catalysts: Part 2. Impact of the support composition on the performance in the water-gas shift reaction. *Appl Catal B Environ.* 2011;101(3-4):266-274. doi:10.1016/j.apcatb.2010.11.021.
 20. Zhang F, Zheng Q, Wei K, et al. Improved performance of Au/Fe₂O₃ catalysts promoted with ZrO₂ and Nb₂O₅ in the WGS reaction under hydrogen-rich conditions. *Catal Letters.* 2006;108(3-4):131-136. doi:10.1007/s10562-006-0047-5.
 21. Pereira ALC, Berrocal GJP, Marchetti SG, Alborno A, de Souza AO, do Carmo Rangel M. A comparison between the precipitation and impregnation methods for water gas shift catalysts. *J Mol Catal A Chem.* 2008;281(1-2):66-72. doi:10.1016/j.molcata.2007.07.042.
 22. Lin X, Zhang Y, Yin L, Chen C, Zhan Y, Li D. Characterization and catalytic performance of copper-based WGS catalysts derived from copper ferrite. *Int J Hydrogen Energy.* 2014;39(12):6424-6432. doi:10.1016/j.ijhydene.2014.02.018.

23. Lin X, Li R, Zhang Y, et al. The role of surface copper species in Cu-Fe composite oxide catalysts for the water gas shift reaction. *Int J Hydrogen Energy*. 2015;40(4):1735-1741. doi:10.1016/j.ijhydene.2014.11.105.
24. Scariot M, Francisco MSP, Jordão MH, Zanchet D, Logli MA, Vicentini VP. An investigation of the activation process of high temperature shift catalyst. *Catal Today*. 2008;133-135(1-4):174-180. doi:10.1016/j.cattod.2007.12.090.
25. Edwards MA, Whittle DM, Rhodes C, et al. Microstructural studies of the copper promoted iron oxide/chromia water-gas shift catalyst. *Phys Chem Chem Phys*. 2002;4(15):3902-3908. doi:10.1039/b202347b.
26. Patlolla A, Carino EV, Ehrlich SN, Stavitski E, Frenkel AI. Application of operando XAS, XRD, and Raman spectroscopy for phase speciation in water gas shift reaction catalysts. *ACS Catal*. 2012;2(11):2216-2223. doi:10.1021/cs300414c.
27. Diagne C, Vos PJ, Kiennemann A, Perrez MJ, Portela MF. Water-gas shift reaction over chromia-promoted magnetite. Use of temperature-programmed desorption and chemical trapping in the study of the reaction mechanism. *React Kinet Catal Lett*. 1990;42:25-31. doi:10.1007/BF02137613.
28. Tinkle M, Dumesic JA. Isotopic exchange measurements of the rates of adsorption/desorption and interconversion of CO and CO₂ over chromia-promoted magnetite: Implications for water-gas shift. *J Catal*. 1987;103(1):65-78. doi:10.1016/0021-9517(87)90093-5.
29. Rhodes C, Hutchings GJ. Studies of the role of the copper promoter in the iron oxide/chromia high temperature water gas shift catalyst. *Phys Chem Chem Phys*. 2003;5(2003):2719-2723. doi:10.1039/b303236c.
30. Kappen P, Grunwaldt JD, Hammershoi BS, Troger L, Clausen BS. The state of Cu promoter atoms in high-temperature shift catalysts - An in situ fluorescence XAFS study. *J Catal*. 2001;198(1):56-65. doi:10.1006/jcat.2000.3071.
31. Puig-Molina A, Cano FM, Janssens TVW. The Cu promoter in an iron-chromium-oxide based water-gas shift catalyst under industrial conditions studied by in-situ XAFS. *J Phys Chem C*. 2010;114(36):15410-15416. doi:10.1021/jp1035103.
32. Magalhaes F, Pereira MC, Botrel SEC, et al. Cr-containing magnetites Fe_{3-x}Cr_xO₄: The role of Cr³⁺ and Fe²⁺ on the stability and reactivity towards H₂O₂ reactions. *Appl Catal A Gen*. 2007;332(1):115-123. doi:10.1016/j.apcata.2007.08.002.
33. Estrella M, Barrio L, Zhou G, et al. In situ characterization of CuFe₂O₄ and Cu/Fe₃O₄ water - gas shift catalysts. *J Phys, Chem, C*.

- 2009;113:14411-14417. doi:10.1021/jp903818q.
34. Rodriguez JA, Hanson JC, Stacchiola D, Senanayake SD. In situ/operando studies for the production of hydrogen through the water-gas shift on metal oxide catalysts. *Phys Chem Chem Phys*. 2013;15:12004-12025. doi:10.1039/c3cp50416f.
 35. Wachs IE, Keturakis CJ. Monolayer systems. In: Schlögl R, ed. *Comprehensive Inorganic Chemistry II*. Waltham, MA: Elsevier; 2013:131-151.
 36. Keturakis CJ, Zhu M, Gibson EK, et al. Dynamics of CrO₃-Fe₂O₃ Catalysts during the high-temperature water-gas shift reaction: molecular structures and reactivity. *ACS Catal*. 2016;6(7):4786-4798. doi:10.1021/acscatal.6b01281.
 37. Zhu M, Wachs IE. Resolving the reaction mechanism for H₂ formation from high-temperature water-gas shift by chromium-iron oxide catalysts. *ACS Catal*. 2016;6(5):2827-2830. doi:10.1021/acscatal.6b00659.
 38. Zhu M, Rocha TCR, Lunkenbein T, Knop-Gericke A, Schlögl R, Wachs IE. Promotion mechanisms of iron oxide-based high temperature water-gas shift catalysts by chromium and copper. *ACS Catal*. 2016;6(7):4455-4464. doi:10.1021/acscatal.6b00698.
 39. Zhu M, Wachs IE. Determining number of active sites and TOF for the high-temperature water gas shift reaction by iron oxide-based catalysts. *ACS Catal*. 2016;6(3):1764-1767. doi:10.1021/acscatal.5b02961.
 40. De Araujo GC, do Carmo Rangel M. An environmental friendly catalyst for the high temperature shift reaction. *Stud Surf Sci Catal*. 2000;130:1601-1606. doi:10.1016/S0167-2991(00)80429-2.
 41. Meshkani F, Rezaei M. High temperature water gas shift reaction over promoted iron based catalysts prepared by pyrolysis method. *Int J Hydrogen Energy*. 2014;39(29):16318-16328. doi:10.1016/j.ijhydene.2014.07.176.
 42. Bouarab R, Bennici S, Mirodatos C, Auroux A. Hydrogen production from the water-gas shift reaction on iron oxide catalysts. *J Catal*. 2014;2014:1-6. doi:10.1155/2014/612575.
 43. Martos C, Dufour J, Ruiz A. Synthesis of Fe₃O₄-based catalysts for the high-temperature water gas shift reaction. *Int J Hydrogen Energy*. 2009;34(10):4475-4481. doi:10.1016/j.ijhydene.2008.08.042.
 44. Gawade P, Mirkelamoglu B, Tan B, Ozkan US. Cr-free Fe-based water-gas shift catalysts prepared through propylene oxide-assisted sol-gel technique. *J Mol Catal A Chem*. 2010;321(1-2):61-70. doi:10.1016/j.molcata.2010.02.002.
 45. Zhang L, Wang X, Millet JMM, Matter PH, Ozkan US. Investigation of

highly active Fe-Al-Cu catalysts for water-gas shift reaction. *Appl Catal A Gen.* 2008;351(1):1-8. doi:10.1016/j.apcata.2008.08.019.

46. Ye Y, Wang L, Zhang S, Zhu Y, Shan J, Tao FF. The role of copper in catalytic performance of a Fe-Cu-Al-O catalyst for water gas shift reaction. *Chem Commun (Camb).* 2013;49(39):4385-4387. doi:10.1039/c2cc37416a.
47. Bao Z, Ding W, Li Q. Effect of Fe/Cu ratio on the activity of Fe-Al-Cu catalysts for water gas shift reaction under hydrogen-rich atmosphere. *Int J Hydrogen Energy.* 2012;37(1):951-955. doi:10.1016/j.ijhydene.2011.03.095.
48. Bliem R, Pavelec J, Gamba O, et al. Adsorption and incorporation of transition metals at the magnetite Fe₃O₄ (001) surface. *Phys Rev B.* 2015;92(7):75440. doi:10.1103/PhysRevB.92.075440.
49. Gangwar A, Alla SK, Srivastava M, et al. Structural and magnetic characterization of Zr-substituted magnetite (Zr_xFe_{3-x}O₄, 0 ≤ x ≤ 1). *J Magn Mater.* 2016;401:559-566. doi:10.1016/j.jmmm.2015.10.087.
50. Hakeem AA, Rajendran J, Kapteijn F, Makkee M. Effect of rhodium on the water-gas shift performance of Fe₂O₃/ZrO₂ and CeO₂/ZrO₂: Influence of rhodium precursor. *Catal Today.* 2015;242(Part A):168-177. doi:10.1016/j.cattod.2014.05.015.
51. Hakeem AA, Rajendran J, Kapteijn F, Makkee M. Promotion or additive activity? the role of gold on zirconia supported iron oxide in high temperature water-gas shift. *J Mol Catal A Chem.* 2016;420:115-123. doi:10.1016/j.molcata.2016.04.017.
52. Hakeem AA, S. Vásquez R, Rajendran J, et al. The role of rhodium in the mechanism of the water-gas shift over zirconia supported iron oxide. *J Catal.* 2014;313:34-45. doi:10.1016/j.jcat.2014.02.010.
53. Hakeem AA, Li M, Berger RJ, Kapteijn F, Makkee M. Kinetics of the high temperature water-gas shift over Fe₂O₃/ZrO₂, Rh/ZrO₂ and Rh/Fe₂O₃/ZrO₂. *Chem Eng J.* 2015;263:427-434. doi:10.1016/j.cej.2014.10.104.
54. Ladebeck J, Kochloefl K. Cr-free iron-catalysts for water-gas shift reaction. *Stud Surf Sci Catal.* 1995;91:1079-1083. doi:10.1016/S0167-2991(06)81851-3.
55. Yamaguchi D, Tang L, Burke N, Trimm D, Chiang K, Nguyen K. Redox performance of modified iron oxides for hydrogen production. *Nov Gas Convers Symp 9, Lyon, Fr 30 May - 4 June.* 2011:CDROM.
56. Trovarelli A. *Catalytic Science Series: Catalysis by Ceria and Related Materials.* Imperial Collage Press; 2002.

57. Pradhan S, Reddy AS, Devi RN, Chilukuri S. Copper-based catalysts for water gas shift reaction: Influence of support on their catalytic activity. *Catal Today*. 2009;141(1-2):72-76. doi:10.1016/j.cattod.2008.06.026.
58. Ou X-J, Cheng J-Y, Wang H-M, Xiao Y. Effects of metal oxides on stability and activity of iron-based chromia-free catalysts for water-gas shift reaction. *J Nat Gas Chem*. 1999;8(3):231-237.
59. Reddy GK, Boolchand P, Smirniotis PG. Unexpected behavior of copper in modified ferrites during high temperature WGS reaction-aspects of $\text{Fe}^{3+} \leftrightarrow \text{Fe}^{2+}$ redox chemistry from Mössbauer and XPS studies. *J Phys Chem C*. 2012;116(20):11019-11031. doi:10.1021/jp301090d.
60. Reddy GK, Smirniotis PG. Effect of copper as a dopant on the water gas shift activity of Fe/Ce and Fe/Cr modified ferrites. *Catal Letters*. 2011;141(1):27-32. doi:10.1007/s10562-010-0465-2.
61. Schmieg SJ, Belton DN. Effect of hydrothermal aging on oxygen storage/release and activity in a commercial automotive catalyst. *Appl Catal B, Environ*. 1995;6(2):127-144. doi:10.1016/0926-3373(95)00011-9.
62. Zerva C, Philippopoulos CJ. Ceria catalysts for water gas shift reaction: Influence of preparation method on their activity. *Appl Catal B Environ*. 2006;67(1-2):105-112. doi:10.1016/j.apcatb.2006.04.013.
63. Reddy GK, Gunasekara K, Boolchand P, Smirniotis PG. Cr- and Ce-doped ferrite catalysts for the high temperature water-gas shift reaction: TPR and Mössbauer spectroscopic study. *J Phys Chem C*. 2011;115(4):920-930. doi:10.1021/jp102959p.
64. Silva AC, Oliveira DQL, Oliveira LCA, et al. Nb-containing hematites $\text{Fe}_{2-x}\text{Nb}_x\text{O}_3$: The role of Nb^{5+} on the reactivity in presence of the H_2O_2 or ultraviolet light. *Appl Catal A Gen*. 2009;357(1):79-84. doi:10.1016/j.apcata.2009.01.014.
65. Silva AC, Cepera RM, Pereira MC, Lima DQ, Fabris JD, Oliveira LCA. Heterogeneous catalyst based on peroxo-niobium complexes immobilized over iron oxide for organic oxidation in water. *Appl Catal B Environ*. 2011;107(3-4):237-244. doi:10.1016/j.apcatb.2011.07.017.
66. Rahim Pouran S, Abdul Aziz AR, Wan Daud WMA, Embong Z. Niobium substituted magnetite as a strong heterogeneous Fenton catalyst for wastewater treatment. *Appl Surf Sci*. 2015;351:175-187. doi:10.1016/j.apsusc.2015.05.131.
67. Joseph Y, Kuhrs C, Ranke W, Ritter M, Weiss W. Adsorption of water on $\text{FeO}(111)$ and $\text{Fe}_3\text{O}_4(111)$: identification of active sites for dissociation. *Chem Phys Lett*. 1999;31:195-202. doi:10.1016/S0009-2614(99)01159-8.

68. Joseph Y, Ranke W, Weiss W. Water on FeO(111) and Fe₃O₄(111): Adsorption behavior on different surface terminations. *J Phys Chem B*. 2000;104(111):3224-3236. doi:10.1021/jp9932012.
69. Shaikhutdinov S, Ritter M, Wang X, Over H, Weiss W. Defect structures on epitaxial Fe₃O₄ (111) films. *Phys Rev B*. 1999;60(15):62-69. doi:10.1103/PhysRevB.60.11062.
70. Paul M, Sing M, Claessen R, Schrupp D, Brabers VAM. Thermodynamic stability and atomic and electronic structure of reduced Fe₃O₄ (111) single-crystal surfaces. *Phys Rev B*. 2007;76(7):75412. doi:10.1103/PhysRevB.76.075412.
71. Cutting RS, Muryn CA, Vaughan DJ, Thornton G. Substrate-termination and H₂O-coverage dependent dissociation of H₂O on Fe₃O₄(111). *Surf Sci*. 2008;602(6):1155-1165. doi:10.1016/j.susc.2008.01.012.
72. Van Natter RM, Coleman JS, Lund CRF. DFT models for active sites on high temperature water-gas shift catalysts. *J Mol Catal A Chem*. 2008;292(1-2):76-82. doi:10.1016/j.molcata.2008.07.015.
73. Bohlbro H. The kinetics of the water gas conversion at atmospheric pressure. *Acta Chem Scand*. 1961;15:502-520. doi:10.3891/acta.chem.scand.15-0502.
74. Bohlbro H. The kinetics of the water gas conversion. II. Investigations at elevated pressures. *Acta Chem Scand*. 1962;16:431-438. doi:10.3891/acta.chem.scand.16-0431.
75. Van Natter RM, Coleman JS, Lund CRF. A DFT study of the effect of copper promotion upon iron oxide surface species. *J Mol Catal A Chem*. 2009;311(1-2):17-22. doi:10.1016/j.molcata.2009.07.013.
76. Yu X, Huo C-F, Li Y-W, Wang J, Jiao H. Fe₃O₄ surface electronic structures and stability from GGA+U. *Surf Sci*. 2012;606(9-10):872-879. doi:10.1016/j.susc.2012.02.003.
77. Santos-Carballal D, Roldan A, Grau-Crespo R, de Leeuw NH. A DFT study of the structures, stabilities and redox behaviour of the major surfaces of magnetite Fe₃O₄. *Phys Chem Chem Phys*. 2014;16(39):21082-21097. doi:10.1039/c4cp00529e.
78. Grillo ME, Finnis MW, Ranke W. Surface structure and water adsorption on Fe₃O₄(111): Spin-density functional theory and on-site Coulomb interactions. *Phys Rev B*. 2008;77(7):75407. doi:10.1103/PhysRevB.77.075407.
79. Yang T, Wen X-D, Ren J, Li Y-W, Wang J-G, Huo C-F. Surface structures of Fe₃O₄ (111), (110), and (001): A density functional theory study. *J Fuel Chem Technol*. 2010;38(1):121-128. doi:10.1016/S1872-5813(10)60024-2.

80. Kiejna A, Ossowski T, Pabisiak T. Surface properties of the clean and Au/Pd covered Fe₃O₄(111): DFT and DFT+U study. *Phys Rev B*. 2012;85(12):125414. doi:10.1103/PhysRevB.85.125414.
81. Yang T, Wen X-D, Cao D-B, Li Y-W, Wang J-G, Huo C-F. Structures and energetics of H₂O adsorption on the Fe₃O₄(111) surface. *J Fuel Chem Technol*. 2009;37(4):506-512. doi:10.1016/S1872-5813(10)60006-0.
82. Zhou C, Zhang Q, Chen L, et al. Density functional theory study of water dissociative chemisorption on the Fe₃O₄(111) surface. *J Phys Chem C*. 2010;114(49):21405-21410. doi:10.1021/jp105040v.
83. Li X, Paier J. Adsorption of water on the Fe₃O₄ (111) surface: structures, stabilities, and vibrational properties studied by density functional theory. *J Phys Chem C*. 2016;120(111):1056-1065. doi:10.1021/acs.jpcc.5b10560.
84. Huang D-M, Cao D-B, Li Y-W, Jiao H. Density function theory study of CO adsorption on Fe₃O₄(111) surface. *J Phys Chem B*. 2006;110(28):13920-13925. doi:10.1021/jp0568273.
85. Rim KT, Eom D, Chan S, Flytzani-Stephanopoulos M. Scanning tunneling microscopy and theoretical study of water adsorption on Fe₃O₄: implications for catalysis. *J Am Chem Soc*. 2012;134:18979-18985. doi:10.1021/ja305294x.
86. Huang L, Han B, Zhang Q, Fan M, Cheng H. Mechanistic study on water gas shift reaction on the Fe₃O₄(111) reconstructed surface. *J Phys Chem C*. 2015;119(52):28934-28945. doi:10.1021/acs.jpcc.5b09192.
87. Dementyev P, Dostert K-H, Ivars-Barceló F, et al. Water interaction with iron oxides. *Angew Chemie Int Ed*. 2015;54:13942-13946. doi:10.1002/anie.201506439.
88. Fu Z, Wang J, Zhang N, An Y, Yang Z. Effect of Cu doping on the catalytic activity of Fe₃O₄ in water-gas shift reactions. *Int J Hydrogen Energy*. 2015;40(5):2193-2198. doi:10.1016/j.ijhydene.2014.12.063.
89. Guvelioglu GH, Ma P, He X, Forrey RC, Cheng H. Evolution of small copper clusters and dissociative chemisorption of hydrogen. *Phys Rev Lett*. 2005;94(2):3-6. doi:10.1103/PhysRevLett.94.026103.
90. Chen L, Zhang Q, Zhang Y, et al. A first principles study of water dissociation on small copper clusters. *Phys Chem Chem Phys*. 2010;12(33):9845-9851. doi:10.1039/c001006e.
91. Xue P, Fu Z, Yang Z. The density functional theory studies on the promoting effect of the Cu-modified Fe₃O₄ catalysts. *Phys Lett A*. 2015;379(6):607-612. doi:10.1016/j.physleta.2014.12.014.
92. Topsøe H. Developments in operando studies and in situ

- characterization of heterogeneous catalysts. *J Catal.* 2003;216(1-2):155-164. doi:10.1016/S0021-9517(02)00133-1.
93. Guerrero-Pérez MO, Bañares MA. From conventional in situ to operando studies in Raman spectroscopy. *Catal Today.* 2006;113(1-2):48-57. doi:10.1016/j.cattod.2005.11.009.
 94. Jones CW, Tao F, Garland MV. Introduction to special issue on operando and in situ studies of catalysis. *ACS Catal.* 2012;2(11):2444-2445. doi:10.1021/cs3006692.
 95. Bañares MA, Wachs IE. Molecular structures of supported metal oxide catalysts under different environments. *J Raman Spectrosc.* 2002;33(5):359-380. doi:10.1002/jrs.866.
 96. Rodriguez AA, Hanson JC, Chupas PJ. *In-Situ Characterization of Heterogeneous Catalysts.* New Jersey, USA: John Wiley & Sons, Inc.; 2013.
 97. Niemantsverdriet JW. *Spectroscopy in Catalysis: An Introduction.* Weinheim: Wiley-VCH; 2007.
 98. Mestl G. In situ Raman spectroscopy - A valuable tool to understand operating catalysts. *J Mol Catal A Chem.* 2000;158(1):45-65. doi:10.1016/S1381-1169(00)00042-X.
 99. Knözinger H. In situ Raman spectroscopy. A powerful tool for studies in selective catalytic oxidation. *Catal Today.* 1996;32:71-80. doi:10.1016/S0920-5861(96)00074-0.
 100. Wachs IE. In situ Raman spectroscopy studies of catalysts. *Top Catal.* 1999;8:57-63. doi:10.1023/A:1019100925300.
 101. Das RS, Agrawal YK. Raman spectroscopy: Recent advancements, techniques and applications. *Vib Spectrosc.* 2011;57(2):163-176. doi:10.1016/j.vibspec.2011.08.003.
 102. Brongersma HH, Draxler M, de Ridder M, Bauer P. Surface composition analysis by low-energy ion scattering. *Surf Sci Rep.* 2007;62(3):63-109. doi:10.1016/j.surfrep.2006.12.002.
 103. Goebel D, Bruckner B, Roth D, Ahamer C, Bauer P. Low-energy ion scattering: A quantitative method? *Nucl Instruments Methods Phys Res B.* 2015;354:3-8. doi:10.1016/j.nimb.2014.11.030.
 104. Jehng JM, Wachs IE. Niobium Oxalate - New Precursor for Preparation of Supported Niobium Oxide Catalysts. *ACS Symp Ser.* 1990;437:232-242. doi:10.1021/bk-1990-0437.ch021.
 105. Jehng JM, Wachs IE. Niobium Oxide Solution Chemistry. *J Raman Spectrosc.* 1991;22:83-89. doi:10.1002/jrs.1250220207.
 106. Hafner J. Ab-initio Simulations of Materials Using VASP: Density-

- Functional Theory and Beyond. *J Comput Chem*. 2008;29:2044-2078. doi:10.1002/jcc.21057.
107. Hehre WJ. *A Guide to Molecular Mechanics and Quantum Chemical Calculations*. Wavefunction, Inc.; 2003.
 108. Koch W, Holthausen MC. *A Chemist's Guide to Density Functional Theory*. 2nd ed. Wiley-VCH; 2001. <http://doi.wiley.com/10.1002/3527600043>.
 109. Kohn W. Nobel Lecture: Electronic structure of matter—wave functions and density functionals. *Rev Mod Phys*. 1999;71(5):1253-1266. doi:10.1103/RevModPhys.71.1253.
 110. Hohenberg P, Kohn W. Inhomogeneous electron gas. *Phys Rev B*. 1964;136:B864-B871. doi:10.1103/PhysRev.136.B864.
 111. Harrison NM. An Introduction to Density Functional Theory. *Technology*. 1995;2(1):1-26. doi:10.1016/S1380-7323(05)80031-7.
 112. Kohn W, Sham LJ. Self-consistent equations including exchange and correlation effects. *Phys Rev*. 1965;140(4A):A1133-A1138. doi:10.1103/PhysRev.140.A1133.
 113. Bengone O, Alouani M, Blochl P, Hugel J. Implementation of the projector augmented-wave LDA+U method: Application to the electronic structure of NiO. *Phys Rev B*. 2000;62:16392-16401. doi:10.1103/PhysRevB.62.16392.
 114. Dudarev SL, Savrasov SY, Humphreys CJ, Sutton a. P. Electron-energy-loss spectra and the structural stability of nickel oxide: An LSDA+U study. *Phys Rev B*. 1998;57(3):1505-1509. doi:10.1103/PhysRevB.57.1505.
 115. Kresse G, Furthmüller J. Efficiency of ab-initio total energy calculations for metals and semiconductors using a plane-wave basis set. *Comput Mater Sci*. 1996;6(1):15-50. doi:10.1016/0927-0256(96)00008-0.
 116. Kresse G, Furthmüller J. Efficient iterative schemes for ab initio total-energy calculations using a plane-wave basis set. *Phys Rev B*. 1996;54(16):11169-11186. doi:10.1103/PhysRevB.54.11169.
 117. Sun G, Kürti J, Rajczy P, Kertesz M, Hafner J, Kresse G. Performance of the Vienna ab initio simulation package (VASP) in chemical applications. *J Mol Struct THEOCHEM*. 2003;624:37-45. doi:10.1016/S0166-1280(02)00733-9.
 118. Kresse G, Marsman M, Furthmüller J. Vasp the guide. <http://cms.mpi.univie.ac.at/VASP/>. Published 2013. Accessed January 5, 2014.
 119. Jónsson H, Mills G, Jacobsen KW. Nudged elastic band method for finding minimum energy paths of transitions. *Class Quantum Dyn*

Condens Phase Simulations. 1998:385-404.
doi:10.1142/9789812839664_0016.

120. Tasker PW. The stability of ionic crystal surfaces. *J Phys C Solid State Phys*. 1979;12(22):4977-4984. doi:10.1088/0022-3719/12/22/036.
121. Cornell RM, Schwertmann U. *The Iron Oxides: Structure, Properties, Reactions, Occurrences and Uses*. Wiley-VCH; 2003.
122. Fleet ME. The structure of magnetite. *Acta Crystallogr*. 1981;B37:917-920. doi:10.1107/S0567740881004597.
123. Callister Jr. WD. *Materials Science and Engineering: An Introduction*. 7th ed. John Wiley & Sons; 2007.
124. Okudera H, Kihara K, Matsumoto T. Temperature dependence of structure parameters in natural magnetite: single crystal X-ray studies from 126 to 773 K. *Acta Crystallogr Sect B Struct Sci*. 1996;52(3):450-457. doi:10.1107/S0108768196000845.
125. Levy D, Giustetto R, Hoser A. Structure of magnetite (Fe₃O₄) above the Curie temperature: a cation ordering study. *Phys Chem Miner*. 2012;39(2):169-176. doi:10.1007/s00269-011-0472-x.
126. Iizumi M, Koetzle TF, Shirane G, Chikazumi S, Matsui M, Todo S. Structure of magnetite (Fe₃O₄) below the Verwey transition temperature. *Acta Crystallogr*. 1982;B38(8):2121-2133. doi:10.1107/S0567740882008176.
127. Dronskowski R. The little maghemite story: A classic functional material. *Adv Funct Mater*. 2001;11(1):27-29. doi:10.1002/1616-3028(200102)11:1<27::AID-ADFM27>3.0.CO;2-X.
128. Grau-Crespo R, Al-Baitai AY, Saadoune I, De Leeuw NH. Vacancy ordering and electronic structure of γ -Fe₂O₃ (maghemite): a theoretical investigation. *J Phys Condens Matter*. 2010;22(25):255401. doi:10.1088/0953-8984/22/25/255401.
129. Aragón R. Magnetization and exchange in nonstoichiometric magnetite. *Phys Rev B*. 1992;46(9):5328-5333. doi:10.1103/PhysRevB.46.5328.
130. Gaudry E, Kiratisin A, Sainctavit P, et al. Structural and electronic relaxations around substitutional Cr³⁺ and Fe³⁺ ions in corundum. *Phys Rev B*. 2003;67(9):94108. doi:10.1103/PhysRevB.67.094108.
131. Benny S, Grau-Crespo R, de Leeuw NH. A theoretical investigation of α -Fe₂O₃-Cr₂O₃ solid solutions. *Phys Chem Chem Phys*. 2009;11(5):808-815. doi:10.1039/B815907F.
132. Tang W, Sanville E, Henkelman G. A grid-based Bader analysis algorithm without lattice bias. *J Phys Condens Matter*. 2009;21(8):84204. doi:10.1088/0953-8984/21/8/084204.

133. NIST. Computational Chemistry Comparison and Benchmark DataBase. <http://cccbdb.nist.gov/>. Accessed May 25, 2015.
134. Noh J, Osman OI, Aziz SG, Winget P, Brédas J-L. Magnetite Fe₃O₄ (111) surfaces: impact of defects on structure, stability, and electronic properties. *Chem Mater*. 2015;27(17):5856-5867. doi:10.1021/acs.chemmater.5b02885.
135. Robbins M, Wertheim GK, Sherwood RC, Buchanan DNE. Magnetic properties and site distributions in the system FeCr₂O₄-Fe₃O₄ (Fe²⁺Cr_{2-x}Fe_x³⁺O₄). *J Phys Chem Solids*. 1971;32:717-729. doi:https://doi.org/10.1016/S0022-3697(71)80412-2.
136. Ok HN, Pan LS, Evans BJ. 57Fe Mössbauer study of chromium-doped magnetite, Fe_{3-x}Cr_xO₄ (0<x<0.5) above the Verwey transition. *Phys Rev B*. 1978;17:85-90. doi:https://doi.org/10.1103/PhysRevB.17.85.
137. Haynes WM. *CRC Handbook of Chemistry and Physics*. 93rd edn. (Haynes WM, ed.). London: Taylor & Francis; 2012.
138. Lemire C, Meyer R, Henrich VE, Shaikhutnov S, Freund HJ. The surface structure of Fe₃O₄(111) films as studied by CO adsorption. *Surf Sci*. 2004;572(1):103-114. doi:10.1016/j.susc.2004.08.033.
139. Morris MC, McMurdie HF, Evans EH, et al. *Standard X-Ray Diffraction Powder Patterns*. Washington, D.C.: National Bureau of Standards: for sale by the Supt. of Docs., U.S. Govt. Print.; 1981. <http://digicoll.manoa.hawaii.edu/techreports/PDF/NBS25-18.pdf>.
140. Tian H, Wachs IE, Briand LE. Comparison of UV and visible Raman spectroscopy of bulk metal molybdate and metal vanadate catalysts. *J Phys Chem B*. 2005;109(49):23491-23499. doi:10.1021/jp053879j.
141. Shebanova ON, Lazor P. Raman spectroscopic study of magnetite (FeFe₂O₄): A new assignment for the vibrational spectrum. *J Solid State Chem*. 2003;174(2):424-430. doi:10.1016/S0022-4596(03)00294-9.
142. Hanesch M. Raman spectroscopy of iron oxides and (oxy)hydroxides at low laser power and possible applications in environmental magnetic studies. *Geophys J Int*. 2009;177(3):941-948. doi:10.1111/j.1365-246X.2009.04122.x.
143. Shannon RD. Revised effective ionic radii and systematic studies of interatomic distances in halides and chalcogenides central research and development department, experimental station, E. L Du Pont de Nemours The effective ionic radii of Shannon & Prewitt [*Acta. Acta Cryst*. 1976;A 32:751-767. doi:10.1107/S0567739476001551.
144. Perez-Alonso FJ, Granados ML, Ojeda M, et al. Relevance in the Fischer-Tropsch synthesis of the formation of Fe-O-Ce interactions on iron-cerium mixed oxide systems. *J Mater Chem B*. 2006;110:23870-

23880. doi:10.1021/jp064575f.

145. Ishigame M, Sakurai T. Temperature dependence of the Raman spectra of ZrO₂. *J Am Ceram Soc.* 1977;60:367-369. doi:10.1111/j.1151-2916.1977.tb15561.x.
146. Naumenko AP, Berezovska NI, Biliy MM, Shevchenko OV. Vibrational analysis and Raman spectra of tetragonal Zirconia. *Phys Chem Solid State.* 2008;9:121-125.
147. de Ridder M, van de Ven PC, van Welzenis RG, et al. Growth of iron oxide on yttria-stabilized zirconia by atomic layer deposition. *J Mater Chem B.* 2002;106:13146-13153. doi:10.1021/jp0211640.
148. Anantharaman MR, Reijne S, Jacobs JP, Brongersma HH, Smits RHH, Seshan K. Preferential exposure of certain crystallographic planes on the surface of spinel ferrites: a study by LEIS on polycrystalline spinel ferrite surfaces. *J Mater Sci.* 1999;34:4279-4283. doi:10.1023/A:1004615222119.
149. Phivilay SP, Puretzky AA, Domen K, Wachs IE. Nature of catalytic active sites present on the surface of advanced bulk tantalum mixed oxide photocatalysts. *ACS Catal.* 2013;3(12):2920-2929. doi:10.1021/cs400662m.
150. Liu J, Xue D, Li K. Single-crystalline nanoporous Nb₂O₅ nanotubes. *Nanoscale Res Lett.* 2011;6:1-8. doi:10.1186/1556-276X-6-138.
151. Jehng J-M, Wachs IE. Structural chemistry and raman spectra of niobium oxides. *Chem Mater.* 1991;3(1):100-107. doi:10.1021/cm00013a025.
152. Harmsen JMA, Jansen WPA, Hoebink JHBJ, Schouten JC, Brongersma HH. Coke deposition on automotive three-way catalysts studied with LEIS. 2001;74(3):133-137.
153. Sudarsanam P, Mallesham B, Durgasri ND, Reddy BM. Physicochemical characterization and catalytic CO oxidation performance of nanocrystalline Ce-Fe mixed oxides. *RSC Adv.* 2014;4(22):11322. doi:10.1039/C3RA45778H.
154. Lee Y, He G, Akey AJ, Si R, Flytzani-stephanopoulos M, Herman IP. Raman Analysis of Mode Softening in Nanoparticle CeO₂. *J Am Chem Soc.* 2011;133(33):12952-12955.
155. Cava S, Tebcherani SM, Souza IA, et al. Structural characterization of phase transition of Al₂O₃ nanopowders obtained by polymeric precursor method. *Mater Chem Phys.* 2007;103(2-3):394-399. doi:10.1016/j.matchemphys.2007.02.046.

APPENDIX A

Supporting Info for Section 6.2.1

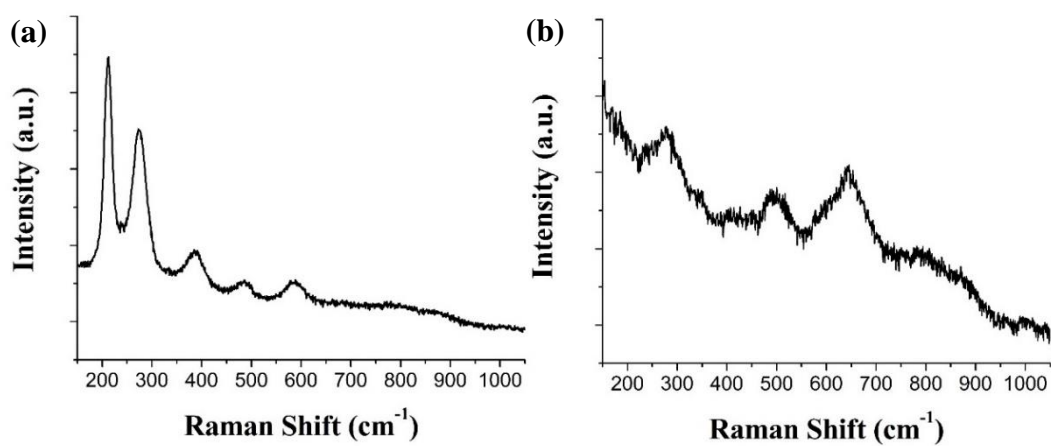


Figure A.1. *In situ* Raman (442nm) spectra of calcined unpromoted iron oxide catalyst at 400 °C: (a) reoxidized in 10% O₂/Ar and (b) RWGS reaction conditions (2nd time, (30 mL/min 5% CO₂/Ar and 15 mL/min 10% H₂/Ar))

CURRICULUM VITAE

PERSONAL INFORMATION

Surname, Name: Yalçın, Özgen
Nationality: Turkish (TC)
Date and Place of Birth: 1st of December 1985, Karaman
Marital Status: Single
Phone: +90 535 239 5352
E-mail: ozgenyalcin@gmail.com

EDUCATION

Degree	Institution	Year of Graduation
MS	METU Chemical Engineering	2011
BS	METU Chemical Engineering	2009
High School	Dr. Binnaz Ege – Dr. Rıdvan Ege Anatolian High School, Ankara	2004

WORK EXPERIENCE

Year	Place	Enrollment
2015-2017	Lehigh University, USA	Research Assistant
2011-2015	METU Dept. of Chemical Engineering	Teaching Assistant
2008 August	KARTONSAN A.Ş., Kocaeli	Intern
2007 August	ATAŞ Anadolu Tasfiyehanesi A.Ş., Mersin	Intern

FOREIGN LANGUAGES

Advanced English, Beginner Spanish

PUBLICATIONS

Peer-reviewed journal articles

1. O. Yalcin, I. Onal “DFT Investigation of High Temperature Water Gas Shift Reaction on Chromium-Iron Mixed Oxide Catalyst” *International Journal of Hydrogen Energy* 2014;39(34):19563-19569

Presented at Conferences

1. O. Yalcin, I. Onal, I.E. Wachs, “Water Gas Shift Reaction over Iron Oxide Catalysts – A DFT Study” - **Poster Presentation**, *2017 Annual Symposium The Catalysis Society of Metropolitan New York*, 22 March 2017, Research and Development Center of the ExxonMobil Research and Engineering Company (EMRE) at Clinton, NJ/USA
2. O. Yalcin, I. Onal, I.E. Wachs, “Water-Gas Shift Reaction on Iron Oxide Catalysts – A DFT Study” - **Oral Presentation**, *2016 AIChE Annual Meeting*, 13-18 November 2016, San Francisco, CA/USA
3. O. Yalcin, I. Onal, I.E. Wachs, “Theoretical and Experimental Investigation of Water Gas Shift (WGS) Reaction Over Iron Oxide Catalysts” - **Oral Presentation**, *252nd ACS National Meeting in Philadelphia*, 21-25 August 2016, Philadelphia, PA/USA
4. O. Yalcin, I. Onal, I.E. Wachs, “Adsorption of Water and Carbon Monoxide as the Reactants of Water Gas Shift Reaction on Chromium-Iron Oxide Catalyst – A DFT Study” - **Poster Presentation**, *2016 Annual Symposium The Catalysis Society of Metropolitan New York*, 23 March 2016, New Brunswick, NJ/USA
5. O. Yalcin, I. Onal, I.E. Wachs, “High Temperature Water Gas Shift Reaction on Chromium-Iron Oxide Catalyst – A DFT Study” - **Poster Presentation**, *Catalysis Club of Philadelphia*, 19 November 2015, Wilmington, DE/USA
6. O. Yalcin, I. Onal, “DFT Investigation of High Temperature Water Gas Shift Reaction on Chromium-Iron Oxide Catalyst” - **Poster Presentation**, *30th European Conference on Surface Science*, 31 August – 5 September 2014, Antalya/Turkey
7. O. Yalcin, I. Onal, “DFT Investigation of High Temperature Water Gas Shift Reaction on Chromium-Iron Mixed Oxide Catalyst” – **Oral Presentation**, *20th World Hydrogen Energy Conference*, 15-20 June 2014, Gwangju Metropolitan City/S. Korea

AWARDS and SCHOLARSHIPS

- 1.** 2214/B International Joint PhD Fellowship Programme 2015 – 2017
TUBITAK (The Scientific and Technological Research Council of Turkey)
- 2.** National Scholarship Programme for PhD Students 2011 – 2015
TUBITAK (The Scientific and Technological Research Council of Turkey)
- 3.** National Scholarship Programme for MSc Students 2010 – 2011
TUBITAK (The Scientific and Technological Research Council of Turkey)
- 4.** 2011-2012 Academic Year METU Graduate Courses Performance Award,
METU Graduate School of Natural and Applied Sciences
- 5.** 2008-2009 Spring Semester Senior Year First in rank

HOBBIES

Yoga, Photography, Cooking